Aachener Verfahrenstechnik Series
AVT.CVT – Chemical Process Engineering
Volume 66 (2026)

Yannick Sebastian Mürtz

Novel Catalyst Systems and Process Optimization of Electrochemical Cells for Ammonia Synthesis

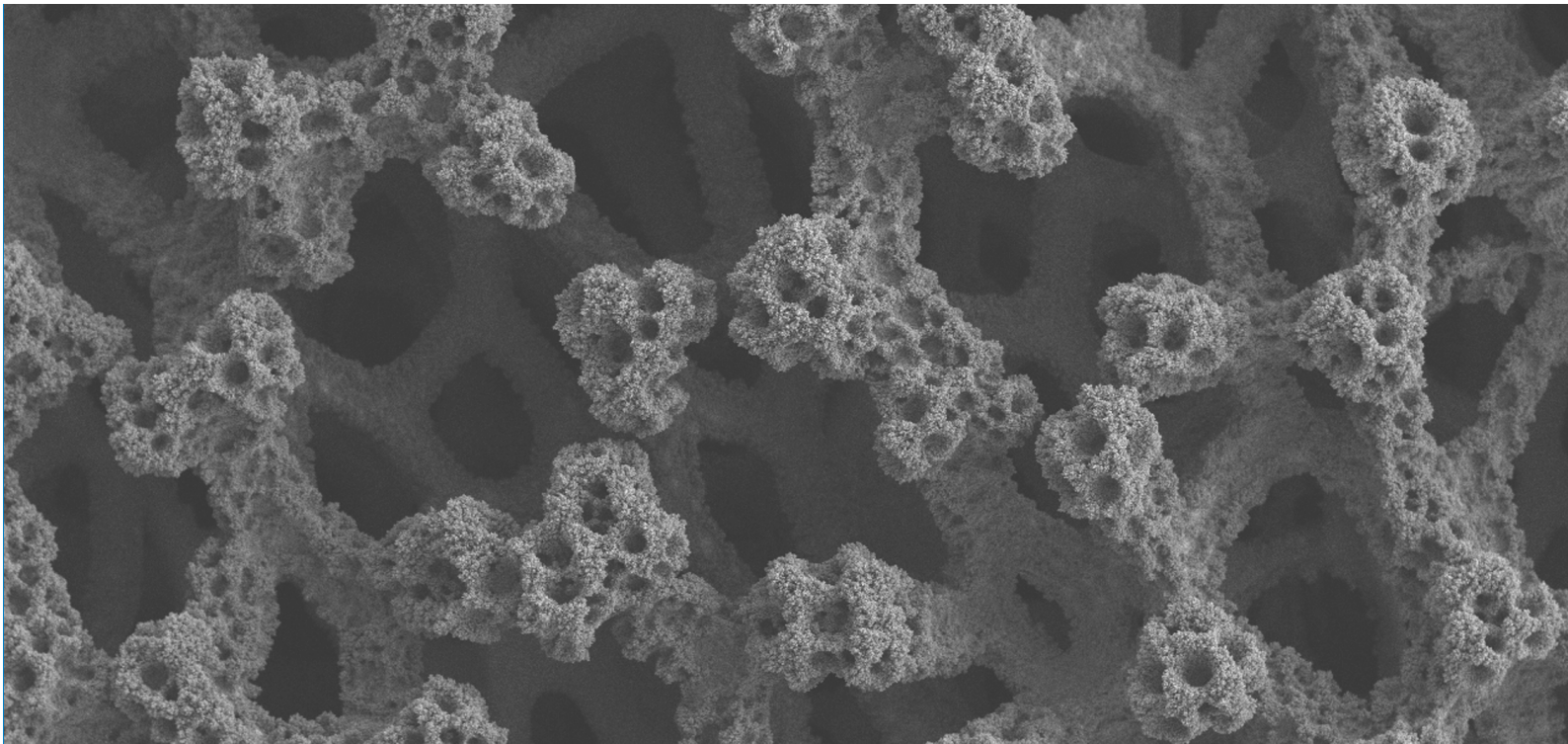

Novel Catalyst Systems and Process Optimization of Electrochemical Cells for Ammonia Synthesis

Neuartige Katalysatorsysteme und Prozessoptimierung elektrochemischer Zellen für die Ammoniaksynthese

Von der Fakultät für Maschinenwesen der
Rheinisch-Westfälischen Technischen Hochschule Aachen
zur Erlangung des akademischen Grades eines Doktors
der Ingenieurwissenschaften genehmigte Dissertation

vorgelegt von

Yannick Sebastian Mürtz, geb. Tschauder

Berichter/in:
Univ.-Prof. Dr.-Ing. Matthias Wessling
Univ.-Prof. Dr. rer. nat. Ulrich Simon

Tag der mündlichen Prüfung: 17.06.2026

Diese Dissertation ist auf den Internetseiten der Universitätsbibliothek online verfügbar.

Impressum

Titel: Novel Catalyst Systems and Process Optimization of Electrochemical Cells for Ammonia Synthesis
Neuartige Katalysatorsysteme und Prozessoptimierung elektrochemischer Zellen für die Ammoniaksynthese

Autor: Yannick Sebastian Mürtz

Reihe: Aachener Verfahrenstechnik Series
AVT.CVT - Chemical Process Engineering
Volume: 66 (2026)

Herausgeber: Aachener Verfahrenstechnik
Forckenbeckstraße 51
52074 Aachen
Tel.: +49 (0)241 8095470
Fax.: +49 (0)241 8092252
E-Mail: secretary.cvt@avt.rwth-aachen.de
http://www.avt.rwth-aachen.de/AVT

Volltext verfügbar: 10.18154/RWTH-2026-06192

Nutzungsbedingungen: Die Universitätsbibliothek der RWTH Aachen University räumt das unentgeltliche, räumlich unbeschränkte und zeitlich auf die Dauer des Schutzrechtes beschränkte einfache Recht ein, das Werk im Rahmen der in der Policy des Dokumentenservers „RWTH Publications“ beschriebenen Nutzungsbedingungen zu vervielfältigen.

Universitätsbibliothek
RWTH Aachen University
Templergraben 61
52062 Aachen
http://www.ub.rwth-aachen.de

Acknowledgement

Auf dieser Arbeit steht zwar nur mein Name, doch hinter dieser Dissertation stehen unzählige Menschen, die mich in den letzten fünf Jahren begleitet haben. Ohne ihre Unterstützung wäre diese Arbeit nicht entstanden.
An erster Stelle möchte ich meinen Doktorvätern Matthias Wessling und Ulrich Simon danken. Matthias danke ich besonders für den Freiraum, eigene Ideen verfolgen zu können. Uli gilt mein Dank für den fachlichen Austausch und insbesondere für das Eröffnen neuer Blickwinkel. Ein ganz besonderer Dank gilt Robert Keller, der gerade in der Anfangszeit meiner Promotion stets versucht hat, meine Interessen zu vertreten, und mich darüber hinaus durchgehend unterstützt hat. Ebenso danke ich allen Kolleginnen und Kollegen am IAC und der CVT, die mir über die Jahre zu Freunden geworden sind, für die gemeinsame Zeit. Auf der Seite der Chemie gilt mein besonderer Dank Ahed Abouserie, Gianluca Dalfollo und Niklas Lothmann, die mich bei meinen Arbeiten unterstützt haben. In der CVT möchte ich mich vor allem bei meinen Büromitbewohnenden Alexander Limper, Lennart Willms, Waralee Dilokekunakul, Tobias Harhues und Maria Padligur dafür bedanken, für die kleinen täglichen Ablenkungen. Inbesondere möchte ich Julian Neumann und Lukas Portheine danken, die mir so manche Zeit versüßt haben. Mein Dank gilt dabei besonders dem Ammoniak-Team, Wenzel Plischka und Yannik Kohlhaas, sowie dem eChem-Team, für die außerordentlichen fachlichen Diskussionen. Ein ganz besonders herzlicher Dank gilt Ann-Kathrin Mertens für die unkomplizierte Aufnahme in die CVT-Familie, die die gesamte Promotionszeit zu etwas ganz Besonderem gemacht hat.
Ebenso bin ich den vielen helfenden Händen meiner Studierenden, die ich betreuen durfte, sowie dem ZAL-Team und insbesondere Justin Gottfried für ihren tatkräftigen Einsatz dankbar, ohne Euch wäre diese Arbeit nicht möglich gewesen.
Lea und Florian Wiesner danke ich für die vielen wunderbaren Gespräche, die mir geholfen haben, Dinge besser zu verstehen, und die mich immer wieder aufgebaut haben. Kerstin Wienkamp, Carla Esch und Wibke Zäng-

ler danke ich für die guten Gespräche, sowohl auf professioneller aber besonders auch auf persönlicher Ebene.
Ihr alle habt meine Promotionszeit bereichert und mitgeholfen, um Wissenschaft zu betreiben, aber auch um eine großartige Zeit zu erleben. Darüber hinaus möchte ich meinen Freunden danken und insbesondere Nils Bues. Du hast mich mit dem ChemCar entzündet, mich an die CVT gebracht und mir meine handwerklichen Fertigkeiten gelehrt, die mir stets hilfreich sind.
Meiner Schwester Lea und meinen Eltern gilt mein riesiger Dank. Ihr unterstützt mich in allen Lebenslagen, baut mich immer wieder auf, ermutigt mich, auch Wege außerhalb der ausgetretenen Pfade zu suchen, und stärkt mich bei allen Entschlüssen und schwierigen Entscheidungen. Ihr seid meine größten Fans.
Mein größter Dank gilt meiner besten Freundin, die mittlerweile zur Ehefrau gewordenen ist, Sonja. Unser gemeinsames Chemiestudium hat uns zusammengeschweißt und unsere Teamfähigkeit geformt. Du begleitest mich durch alle Höhen und Tiefen dieser Promotion, hältst mir in stressigen Zeiten mit dem nötigen Plan den Rücken frei und erinnerst mich immer wieder daran, was im Leben wirklich zählt. Ohne deine Liebe, deine Geduld, deine Ausdauer meine überschwänglichen Emotionen auszuhalten und deinen unerschütterlichen Glauben an mich wäre ich nicht an dieser Stelle und diese Arbeit nie entstanden.

Das Glück ist ein Wie, kein Was; ein Talent, kein Objekt.

Hermann Hesse

Artificial Intelligence (AI) Statement

This thesis has been partially rewritten using an artificial intelligence (AI) model to improve readability. All ideas, considerations, and content are original and created by the author. Therefore, AI systems are not concerned with intellectual property. The AI usage rules stipulated by the Faculty of Mechanical Engineering of RWTH Aachen University on July 29, 2025, have been fully satisfied.

Contents

Acknowledgement iii

Artificial Intelligence (AI) Statement vi

Abstract xi

Zusammenfassung xiii

1. Introduction 1

2. Fundamentals 9

2.1. Electrochemical Fundamentals 9

2.1.1. Electrochemical Reactions 9

2.1.2. Electrochemical Reactors 10

2.1.3. Membranes in Electrochemistry 12

2.1.4. Electrochemical Thermodynamics 14

2.1.5. Electrochemical Kinetics and Interfacial Phenomena 15

2.1.6. Electrochemical Performance Indicators 18

2.1.7. Mass Transport in Liquid Electrolytes 20

2.1.8. Hydrodynamics in Flow Cells and Porous Electrodes 21

2.2. Ammonia Production Processes 24

2.2.1. Grey Haber–Bosch process 25

2.2.2. Green Haber–Bosch process 26

2.2.3. Electrochemical Nitrogen Reduction 27

2.2.4. Nitrate recovery from wastewater streams 28

3. MOF-derived Carbon for Electrochemical Nitrogen Reduction 31

3.1. Introduction 32

3.2. Experimental 37
3.2.1. Materials 37
3.2.2. MOF Synthesis 37
3.2.3. Ammonia Quantification 38
3.2.4. LSV Measurements 38
3.2.5. Gas Scrubbing Setup 39
3.2.6. Gas Diffusion Electrode Preparation 39
3.2.7. Constant Potential Electrolysis 39
3.3. Results and Discussion 41
3.3.1. Structural Characterization of MIL-100 and Basolite F300 . 41
3.3.2. Structural Evolution During Pyrolysis 43
3.3.3. Morphological Characterization 47
3.3.4. Support Characterization 49
3.3.5. Electrochemical Characterization 50
3.4. Conclusion 54

4. Electrochemical Nitrate Reduction in a Batch Cell 57
4.1. Introduction 58
4.2. Experimental 60
4.2.1. Materials 60
4.2.2. Electrochemical Cell 60
4.2.3. Experimental Setup 61
4.2.4. Electrode Materials 63
4.2.5. Gas Analysis 63
4.2.6. Ion Chromatography 64
4.2.7. Performance Parameters 64
4.3. Results and Discussion 66
4.3.1. Membrane Influence 66
4.3.2. Electrode Material Screening 69
4.3.3. Influence of Nitrate Concentration 71
4.3.4. Effect of Hydrodynamics and Spacer Geometry 73
4.4. Conclusion 75

5. Electrochemical Nitrate Reduction in a Continuous Feed-and-Bleed Reactor 77
5.1. Introduction 78

5.2. Materials and Methods 83
5.2.1. Experimental Setup 83
5.2.2. Electrochemical Cell 83
5.2.3. Experimental Procedure 86
5.2.4. Transient Phase 86
5.2.5. Analysis 87
5.3. Results and Discussion 89
5.4. Conclusion 99

6. Catalyst-coated Membranes for Zero-Gap Nitrate Reduction 103
6.1. Introduction 104
6.2. Materials and Methods 107
6.2.1. Membrane Electrode Assembly and Cell Configuration . . . 107
6.2.2. Preparation of Copper-Based Catalyst-Coated Membranes 108
6.2.3. Electrochemical Operation and Analytics 110
6.3. Results and Discussion 112
6.3.1. Effect of Nitrate Concentration 113
6.3.2. Influence of Catholyte Circulation Flow 116
6.3.3. Pulsed Electrolysis and Local Microenvironment 118
6.3.4. Influence of Ionomer Binder 121
6.3.5. Operation without Supporting Electrolyte 124
6.4. Conclusion 127

7. Conclusion and Perspectives 131

A. Figures 137

Bibliography 139

List of Abbreviations 159

Abstract

The defossilization of energy production and the chemical industry requires new sustainable energy sources and new processes for the sustainable production of these and key basic chemicals using renewable energy. Ammonia plays a key role in this as both a chemical raw material and a potential energy source. While electrochemical nitrogen reduction is being intensively investigated as a direct alternative to the Haber-Bosch process, its technical implementation has so far been limited by low conversion rates, low selectivity, and methodological uncertainties. In contrast, the electrochemical reduction of nitrate represents a more robust and technically realistic route, but one that still needs to be implemented, particularly in the context of wastewater streams and the circular economy, as electrochemical processes have so far mostly been investigated on a laboratory scale and under idealized conditions. The starting point of the work is electrochemical nitrogen reduction, which was carried out using specially manufactured nitrogen-free catalysts and under meticulously controlled conditions to avoid contamination effects and false-positive results. Furthermore, nitrate reduction is established as a more promising synthesis route. Building on this, batch-based electrolysis systems are used to investigate the influence of electrolyte composition, pH value, and membrane type on selectivity and yield. A key contribution of this work is the transfer of nitrate reduction to continuously operated electrochemical flow cells and the associated avoidance of dynamic influences. The introduction of a feed-and-bleed operating mode enables stable steady-state operation at a constant nitrate concentration. The systematic variation of the hydrodynamic conditions allows a targeted increase in the ammonia formation current and the derivation of general relationships between mass transport and reaction performance. Through optimization, Faraday efficiencies for ammonia of almost 95 % are achieved at current densities of 600 $mA\,cm^{-2}$. In addition, process intensification is investigated in a zero-gap cell architecture with catalyst-coated membranes. This allows operation at high current densities without the addition of conductive electrolytes and leads to significantly increased ammonia concentrations. The work shows that electrochemical nitrate reduction can be developed into a technically relevant process through suitable reactor and process design and provides general concepts for electrochemical processes under industrially relevant conditions beyond the specific application.

Zusammenfassung

Die Defossilisierung der Energieerzeugung und der chemischen Industrie erfordert neue nachhaltige Energieträger, sowie neue Verfahren zur nachhaltigen Herstellung dieser und weiterer zentraler Grundchemikalien unter Nutzung erneuerbarer Energie. Ammoniak spielt dabei sowohl eine Schlüsselrolle als chemischer Rohstoff als auch als potenzieller Energieträger. Während die elektrochemische Stickstoffreduktion als direkte Alternative zum Haber-Bosch-Verfahren intensiv untersucht wird, ist ihre technische Umsetzung bislang durch geringe Umsätze, niedrige Selektivitäten und methodische Unsicherheiten begrenzt. Die elektrochemische Reduktion von Nitrat stellt demgegenüber eine robustere und technisch realistischere Route dar, die aber insbesondere im Kontext von Abwasserströmen und der Kreislaufwirtschaft noch implementiert werden muss, da elektrochemische Verfahren bisher meist im Labormaßstab und unter idealisierten Bedingungen untersucht worden sind.

Den Ausgangspunkt der Arbeit bildet die elektrochemische Stickstoffreduktion, die mit eigens dafür hergestellten stickstofffreien Katalysatoren und unter penibel kontrollierten Bedingungen durchgeführt wurde, um Kontaminationseffekte und falsch-positive Ergebnisse zu vermeiden. Weiterführend wird die Nitratreduktion als erfolgversprechendere Syntheseroute etabliert. Aufbauend darauf werden Batch-basierte Elektrolysesysteme genutzt, um den Einfluss von Elektrolytzusammensetzung, pH-Wert und Membrantyp auf Selektivität und Ausbeute zu untersuchen.

Ein zentraler Beitrag der Arbeit ist die Übertragung der Nitratreduktion in kontinuierlich betriebene elektrochemische Flusszellen und die damit verbundene Vermeidung von dynamischen Einflüssen. Durch die Einführung eines Feed-and-Bleed Betriebsmodus wird ein stabiler stationärer Betrieb bei konstanter Nitratkonzentration ermöglicht. Die systematische Variation der hydrodynamischen Bedingungen erlaubt eine gezielte Steigerung des Ammoniakbildungsstroms und die Ableitung allgemeiner Zusammenhänge zwischen Stofftransport und Reaktionsleistung. Durch die Optimierung werden Faraday Effizienzen zu Ammoniak von fast 95 % bei Stromdichten von 600 $mA\,cm^{-2}$ erreicht.

Darüber hinaus wird die Prozessintensivierung in einer Zero-Gap Zellarchitektur mit katalysatorbeschichteten Membranen untersucht. Diese erlaubt den Betrieb bei hohen Stromdichten ohne Zusatz von Leitelektrolyten und führt zu deutlich erhöhten Ammoniakkonzentrationen. Die Arbeit zeigt, dass die elektrochemische Nitratreduktion durch geeignete Reaktor- und Prozessführung zu einem technisch relevanten Verfahren entwickelt werden kann und liefert über den spezifischen Anwendungsfall hinaus allgemeine Konzepte für elektrochemische Prozesse unter industriell relevanten Bedingungen.

1. Introduction

Anthropogenic climate change and the associated need to drastically reduce greenhouse gas emissions pose a fundamental challenge to the present paradigm of energy- and resource-intensive chemical production [IPCC2023]. At the same time, a growing world population and rising living standards continue to drive the demand for food, fuels, and materials. Modern agriculture in particular relies on large quantities of synthetic nitrogen fertilizers, predominantly ammonia (NH_3), to sustain high crop yields. Global ammonia production reached approximately 150 Mt in 2024 with about 80 % of this volume being used as fertilizer and the remainder serving as a feedstock for pharmaceuticals, polymers, explosives, and various bulk and fine chemicals [Eris2008; Stat]. Today, roughly 94 % of global NH_3 is synthesized via the Haber-Bosch (HB) process [Smit2020]. In its conventional "grey" form, HB is tightly coupled to hydrogen production by steam methane reforming, resulting in a highly energy- and carbon-intensive value chain. Ammonia synthesis accounts for about 1.4 % of global primary energy consumption and roughly 1.2 % of anthropogenic CO_2 emissions [Appl2011; Smit2020; IEA2021], corresponding to specific emissions on the order of 1.6 to 2.9 kg_{CO_2}/kg_{NH_3} in modern large-scale plants [Smit2020]. The theoretical minimum energy requirement of HB is about 22.2 GJ/t_{NH_3}, whereas state-of-the-art plants typically operate at 27.4 GJ/t_{NH_3}, with only $\approx$18.6 GJ/t_{NH_3} stored in the chemical bonds of NH_3 [Smit2020]. Decarbonizing ammonia production is therefore a key objective for a sustainable chemical industry and for limiting global warm-

ing [IEA2021; IREN2022].

Looking ahead, the role of ammonia is expected to extend beyond its traditional use as a fertilizer. Owing to its high hydrogen content, favorable volumetric energy density, and existing global infrastructure, NH_3 is increasingly considered as a carbon-free energy vector and hydrogen carrier for large-scale power generation and maritime transport [MacF2020; IREN2022]. This prospective ammonia economy implies further growth in NH_3 demand and reinforces the urgency of developing low-carbon or carbon-free production routes that can be integrated into a sustainable energy and materials system [MacF2020; IEA2021].

At the same time, the current anthropogenic nitrogen cycle is essentially linear. Molecular nitrogen (N_2) from the atmosphere is fixed to reactive nitrogen, predominantly as NH_3, via HB. After application as fertilizer, a substantial fraction of this reactive nitrogen is lost to the environment as nitrate (NO_3^-), nitrite (NO_2^-), and other nitrogen species. In particular, nitrate contamination of ground- and surface waters, originating mainly from agricultural runoff and industrial effluents, poses serious ecological and human health risks [Guti2018]. Conventional nitrate removal technologies (e.g. biological denitrification or physico-chemical treatment via ion exchange and membrane processes) typically treat nitrate as waste and often generate concentrated brine streams that require energy-intensive and costly disposal [Guid2022; Barr2023; Huan2024a]. Such end-of-pipe strategies do not recover the nitrogen value and thus remain at odds with the concept of a circular nitrogen economy [MacF2020].

Electrochemical technologies offer an attractive route to couple the decarbonization of ammonia production with a transition from linear to circular nitrogen management. One widely discussed approach is the electrochemical nitrogen reduction reaction (eNRR), which aims to produce NH_3 directly from N_2 and water under ambient conditions [Skúl2011; MacF2020], thereby bypassing fossil-based hydrogen generation and high-pressure thermochemical reactors. However, the cleavage of the N≡N triple bond (bond enthalpy $\approx$941 kJ mol^{-1}) is kinetically demanding, and the hydrogen evolution reaction (HER) typically dominates under ca-

thodic conditions [MacF2020]. Moreover, recent studies have highlighted severe challenges in reliably quantifying low eNRR rates due to contamination and background ammonia, leading to ongoing debate about the true activity of many reported catalysts [He2022].

In contrast, the electrochemical nitrate reduction reaction (eNO_3RR) is thermodynamically more favorable and circumvents the low solubility and slow activation of N_2. Nitrate is already present in the aqueous phase and at elevated oxidation state, such that its reduction to NH_3 can, in principle, combine water treatment with distributed ammonia synthesis.

Hence, the overarching objective of this dissertation is to develop a catalyst and engineering-based process-optimization of electrochemical pathways for sustainable ammonia production from reactive nitrogen species, with a particular focus on nitrate-containing waste and side streams. The central hypothesis is that combining electrochemical nitrate reduction with suitable pre-concentration and reactor concepts can enable decentralized, low-carbon NH_3 synthesis while simultaneously mitigating nitrogen pollution and closing material loops in a circular nitrogen economy [MacF2020; Guo2024].

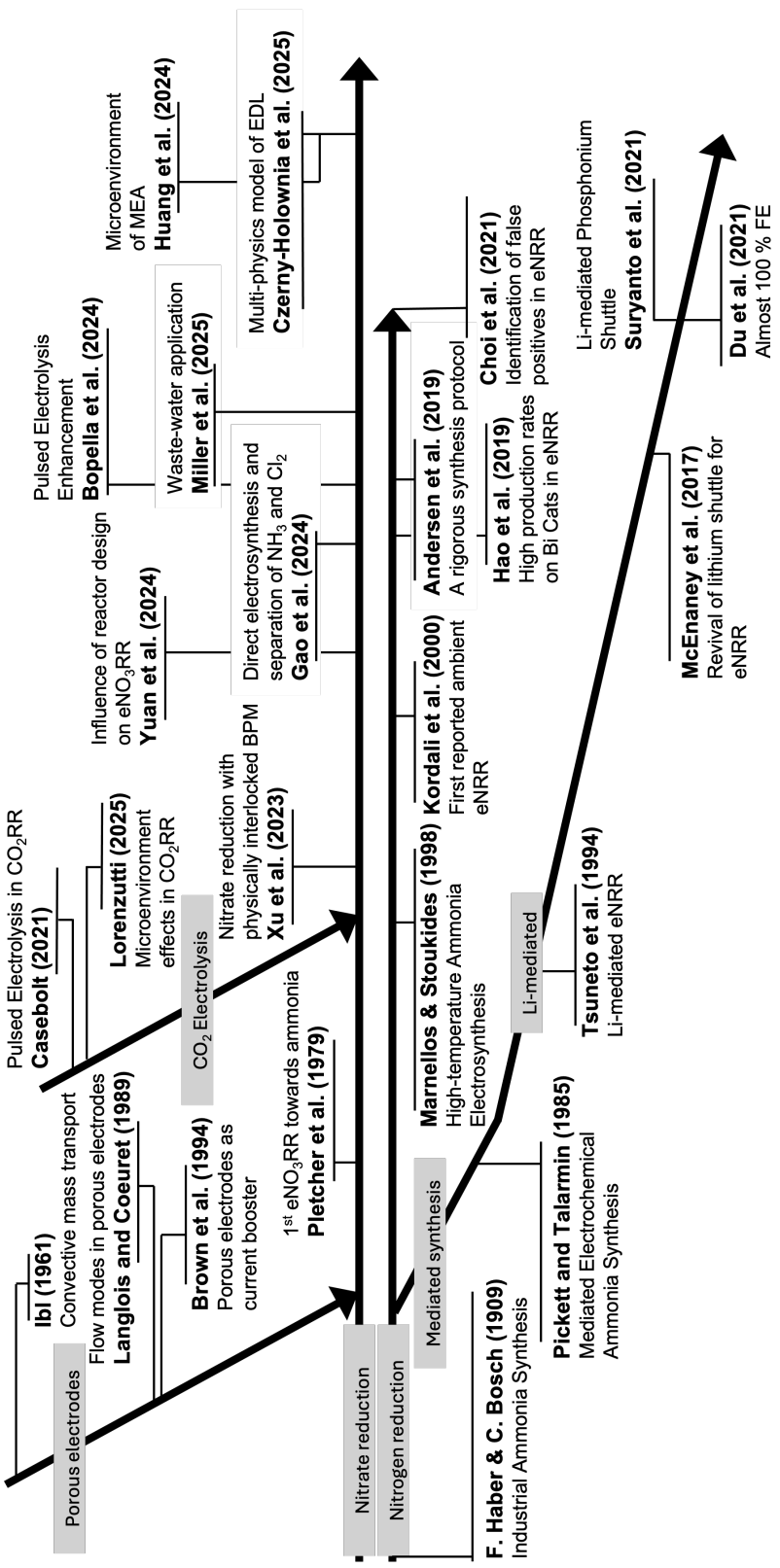

Figure 1.1.: Overview of the field of electrochemical reduction of nitrate (top) [Ibl1961; Lang1989a; Plet1979; Brow1994; Case2021; Xu2023; Gao2024; Yuan2024; Bopp2024; Huan2024b; Mill2024; Lore2025; Czer2025] and nitrogen (bottom) [Pick1985; Pick1985; Marn1998; Tsun1994; Kord2000; McEn2017; Hao2019; Ande2019; Choi2020; Sury2021; Du2022].

About this thesis

This thesis investigates electrochemical pathways for the sustainable conversion of reactive nitrogen species into ammonia (NH_3), with a particular focus on integrating the electrochemical nitrate reduction reaction (eNO_3RR) into process concepts for nitrate-containing wastewaters. The work spans fundamental electrochemical principles, electrocatalyst development, and reactor engineering, thereby connecting molecular-scale mechanisms with cell-level design and operation. The overarching objective is to identify operating regimes and reactor architectures that combine high Faradaic efficiency toward NH_3, efficient use of electrical energy, and compatibility with realistic nitrate feed streams. To address this aim, each core chapter is framed by a single research question.

Chapter 3: Can MOF-derived, nitrogen-free catalysts show intrinsic eNRR activity under rigorous contamination-controlled experiments?

This chapter investigates Metal-Organic-Framework (MOF)-derived carbon materials as model electrocatalysts for the eNRR. A nitrogen-free iron-based MOF precursor is synthesized, thermally converted into conductive carbon, and systematically characterized with respect to morphology, phase composition, and residual nitrogen content. The electrochemical response of the resulting electrodes is evaluated using a rigorous N_2/Ar protocol and strict contamination control. The analysis reveals that, within the detection limits of the employed methodology, no intrinsic N_2-to-NH_3 activity can be attributed to the catalyst, and that previously reported high Faradaic efficiencies are likely dominated by experimental artifacts. This chapter thus motivates the shift of focus from eNRR to eNO_3RR as a more viable electrochemical route to NH_3.

Chapter 4: Which reactor conditions maximize NH_3 FE in batch eNO_3RR?

In this chapter, electrochemical nitrate reduction to NH_3 is demonstrated and analyzed in a two-compartment batch cell. The influence of ion-exchange membrane type, porous metal foam cathodes, nitrate concentration, and hydrodynamic conditions on Faradaic efficiency, product distribution, and cell voltage is systematically quantified. The experiments show that bipolar membranes in inside-out mode, copper foam electrodes, sufficiently high nitrate concentrations, and moderated hydrodynamics are key design elements for achieving high selectivity toward NH_3.

Chapter 5: How can eNO_3RR be operated at steady-state and what influences the reaction?

This chapter extends the batch-cell studies from Chapter 4 to a temperature-controlled, continuous feed-and-bleed reactor equipped with dendrite-modified copper foam cathodes. In this configuration, nitrate conversion, electrolyte composition and pH, current density, and recirculation flow rate are varied to obtain steady-state performance under conditions representative of industrial operation. The analysis elucidates how proton availability, product accumulation, and membrane degradation jointly determine cell voltage and Faradaic efficiency toward NH_3. By decoupling hydrodynamics from overall conversion, the chapter establishes quantitative links between recirculation flow, effective diffusion-layer thickness, and mass-transport limitation and introduces a dimensionless transport framework that connects Reynolds and Sherwood numbers to eNO_3RR performance.

Chapter 6: Can copper-based catalyst-coated membranes enable intensified zero-gap eNO_3RR or supporting-electrolyte-free conditions?

In this chapter, the focus shifts to planar zero-gap cells employing copper-based catalyst-coated membranes (CCMs) on cation-exchange membranes. The working hypothesis is that the CCM architecture can enhance

local proton availability and enable compact reactor layouts for eNO_3RR from concentrated nitrate solutions and treated wastewaters. The chapter investigates the effects of nitrate concentration, catholyte recirculation flow, pulsed versus continuous operation, ionomer binder chemistry, and the presence or absence of supporting electrolyte on Faradaic efficiency and ammonia production rate.

Chapter 7: Conclusion and Perspectives

Finally, this chapter summarizes the insights gained throughout the thesis and discusses their implications for the design of electrochemical processes for sustainable NH_3 production from reactive nitrogen or from nitrate-containing wastewater streams as decentralized nitrogen sources and on the role of electrochemical NH_3 synthesis in a low-carbon chemical industry.

Previous Publications in Student Theses

The content and results of this thesis are the result of research work conducted under the affiliation and position of the author as a research fellow and Ph.D. candidate at RWTH Aachen University. The position is associated with the Chair of Chemical Process Engineering. The work comprises data based on the following student theses:

- Patric Keister, Bachelor Thesis, RWTH Aachen University, 14.10.2022, ”Synthesis and Annealing of the Metal-Organic-Framework Fe-MIL-100 for the Development of an Iron-Based & Nitrogen-Free N_2-Reducing Electrocatalyst”
- Florian Musialek, Research Internship, RWTH Aachen University, 11.05.2023, ”Influence of the Pyrolysis Temperature on Nanoparticle Size of Fe/C and their eNRR Activity.”
- Franz Röllgen, Master Thesis, RWTH Aachen University, 07.10.2024, ”Optimization of Process Parameters for the Electrochemical Nitrate

Reduction towards Ammonia”

- Ferdinand Heinke, Bachelor Thesis, RWTH Aachen University, 04.04.2025, ”Process optimization of electrochemical ammonia synthesis through the reduction of nitrate.”
- Adrian Linnemann, Master Thesis, RWTH Aachen University, 13.11.2025, ”Process optimization of electrochemical NH_3 synthesis”

2. Fundamentals

2.1. Electrochemical Fundamentals

Electrochemistry is the study of heterogeneous reactions involving the reciprocal conversion of chemical and electrical energy through electron transfer at the interface between electrode and electrolyte. This enables the interconversion of chemical and electrical energy. Typically, electrochemical systems are classified based on the direction of energy conversion. In galvanic cells, the free enthalpy of spontaneous chemical reactions is converted into electrical energy, known from batteries. In electrolytic cells, electrical energy is used to drive non-spontaneous chemical reactions, known as electrolysis [Bard2001; Schm2003; Plet2009]. The processes investigated in this thesis are operated exclusively in the electrolytic mode and use electrical energy to drive the conversion.

2.1.1. Electrochemical Reactions

Electrochemical processes are mediated by the transfer of charge, comprising both electron and ion transport. Electrons are conveyed through an external electronic conductor, while ions migrate through an ionically conductive electrolyte to maintain charge balance. In electrolytic operation, the required driving force is imposed as an externally applied potential acting on the electrons, whereas the ionic flux in the electrolyte closes the electrical circuit (Figure 2.1).

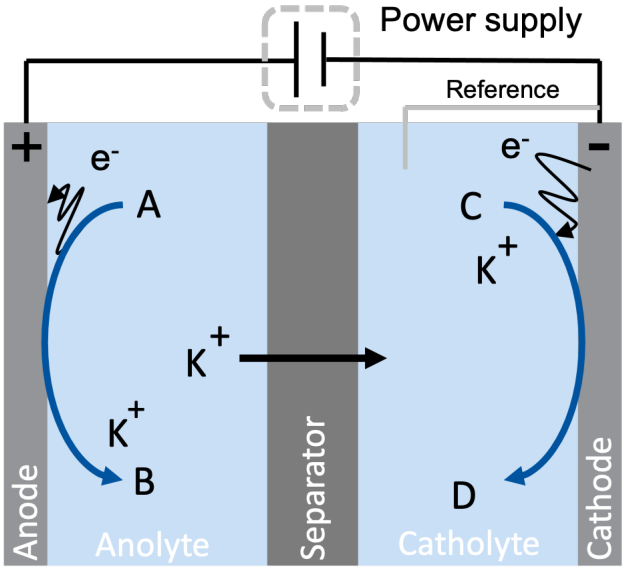

Figure 2.1.: Schematic depiction of an electrochemical cell.

In contrast to conventional redox reactions in homogeneous solution, this explicit partitioning of electronic and ionic pathways leads to a spatial separation of oxidation and reduction into distinct half-reactions at different electrodes. However, both half-reactions remain strictly coupled via the stoichiometric amount of charge transferred. The overall electrochemical reaction can thus be decomposed into its anodic and cathodic half-reactions of oxidation and reduction, respectively, which proceed simultaneously at the respective electrodes.

2.1.2. Electrochemical Reactors

In its simplest configuration, an electrolytic cell consists of two electronically conductive electrodes that are immersed in, and electrically connected through, an ionically conductive electrolyte. If products from anode and cathode should be kept separated, the electrolyte is divided into two compartments, namely anolyte and catholyte, by an ion-permeable separator that permits ionic transport while suppressing bulk mixing of the electrode compartments. Different reactor operation modes can be distinguished based on the manner in which fresh electrolyte is supplied and product is withdrawn. In the context of electrolysis, three idealized modes

are particularly relevant: batch operation, single-pass flow operation, and feed-and-bleed operation (Figure 2.2).

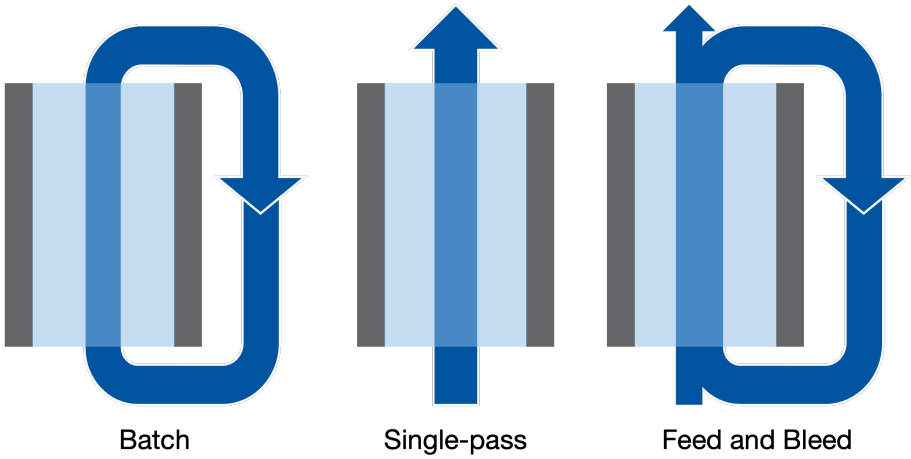

Figure 2.2.: Schematic depiction of different idealized electrochemical reactor flow modes: batch, single-pass flow, and feed-and-bleed (from left to right). Adapted from Bäßler et al. [Baes2025].

In batch operation, the electrolyte is confined in a closed vessel. The electrolyte composition in each compartment changes over time as electroactive species are consumed and products are formed, while the total liquid volume remains approximately constant.

In single-pass operation, fresh electrolyte is continuously fed to the cell and leaves the cell as product stream without recirculation. The inflow composition is constant, and the outflow composition reflects the conversion achieved during a single passage through the electrochemical reactor.

Feed-and-bleed operation represents an intermediate case between batch and single-pass operation. The electrolyte is circulated between an external reservoir and the electrochemical cell. Fresh feed is continuously supplied to the reservoir, while an equal volumetric flow rate is withdrawn as product stream, such that the liquid level in the reservoir remains constant. Inside the reservoir, ideal mixing is typically assumed, so that the concentration is spatially uniform and evolves in time according to a continuous stirred-tank reactor balance that accounts for both electrochemical reaction and convective exchange with the environment.

2.1.3. Membranes in Electrochemistry

Ion-exchange membranes are frequently employed as separators in electrochemical reactors when a physical separation of anolyte and catholyte is required. They suppress convective mixing while allowing ionic transport, thereby enabling different electrolyte compositions and reactants at anode and cathode and preventing undesired product re-oxidation or reduction. This substantially increases the design freedom in electrochemical process engineering, for example in paired electrolysis. Ion-exchange membranes are generally classified as cation exchange membranes (CEMs), anion exchange membranes (AEMs), and bipolar membranes (BPMs) [Schm2003; Drio2016].

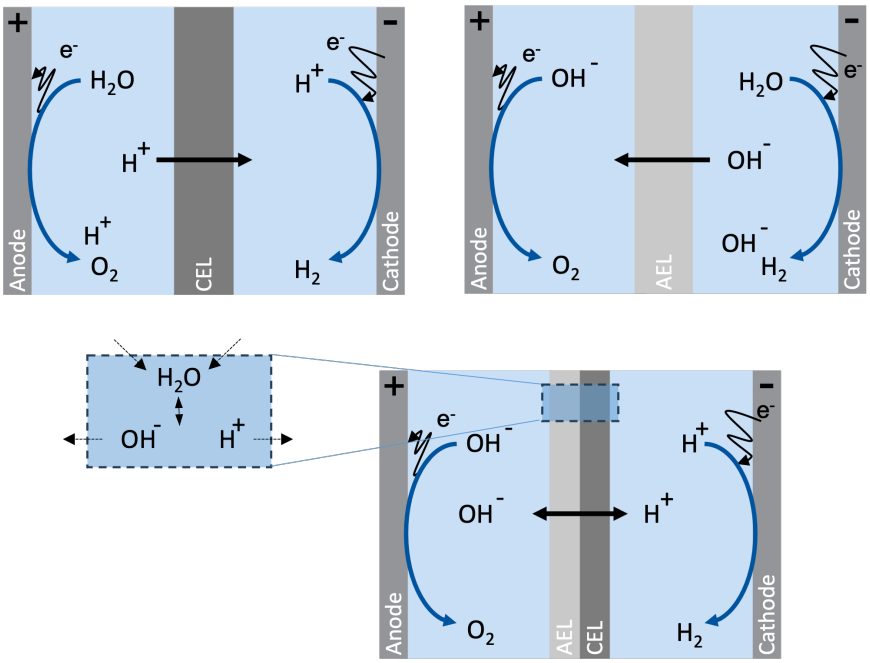

Figure 2.3.: Schematic depiction of ion migration when a CEM, AEM, or BPM is used as separator.

CEMs selectively transport cations and block anions. Under polarization this enforces charge compensation by cation migration, typically protons or background electrolyte cations such as K^+ or Na^+. In aqueous systems with supporting electrolyte concentrations of 0.05 to 0.1 M, the concentration of these co-ions often exceeds that of H^+ or OH^- by several orders

of magnitude, so the co-ions carry most of the current despite their lower mobility [Schm2003].

AEMs, in contrast, preferentially conduct anions (e.g. OH^-). In both cases, ion migration is not restricted to the ions from the autoprotolysis of water but also to the charge carriers involved in the target half-reactions, and includes ions from the supporting electrolyte. This can lead to significant pH drifts in both compartments and to reactant or product crossover, as most reactions in electrochemistry rely on protons or hydroxide ions as charge carrier. Hence, reaction selectivity, electrode stability, and downstream processing are strongly affected [Venn2019; Salv2021; Xu2023].

BPMs consist of a laminated CEM-AEM pair and can include a catalyst layer at the junction that promotes water dissociation. Under reverse bias, water diffuses to the junction, splits into H^+ and OH^-, and the resulting ions migrate into the acidic and alkaline compartments, respectively. Ideally, this allows decoupling of pH in anolyte and catholyte while suppressing co-ion crossover. Under forward bias, H^+ and OH^- from the adjacent electrolytes recombine at the junction to form water. In real BPMs, however, co-ions can still penetrate the individual layers, particularly at elevated current densities, and ionic accumulation inside the membrane stack may contribute to degradation [Blom2020; Pärn2021; Pärn2023]. Moreover, BPMs generally exhibit higher area-specific resistance than monolayer ion-exchange membranes due to their larger thickness and the additional overpotential associated with water dissociation and diffusion to the junction. This limits their operation window in high-current electrolysis, where local water depletion and intense water-splitting fluxes can cause accelerated aging above current densities of a few hundred $mA\,cm^{-2}$ [Krol1998; Blom2021].

Overall, the choice of IEM type and operating mode governs ion fluxes, pH evolution, reactant and product crossover, and cell voltage, and is therefore a central degree of freedom in the design of integrated electrochemical processes.

2.1.4. Electrochemical Thermodynamics

Electrode reactions in aqueous electrolytes can be described in terms of their thermodynamic driving force and the corresponding electron transfer. For a general reaction,

$$\sum_i \nu_i \mathrm{A}_i \rightleftharpoons \sum_j \nu_j \mathrm{B}_j \tag{2.1}$$

the equilibrium (reversible) electrode potential E_{eq} is given by the Nernst equation: The composition of the reacting system at a given state is described by the reaction quotient Q constructed from the activities of products and reactants.

$$Q = \frac{\prod_j a_{B_j}^{\nu_j}}{\prod_i a_{A_i}^{\nu_i}} \tag{2.2}$$

For sufficiently dilute aqueous solutions, activities can often be approximated by concentrations, $a_K \approx c_K/c^0$, with $c^0 = 1\ \mathrm{mol\,L^{-1}}$.

The driving force of a chemical reaction is the change in Gibbs free energy $\Delta_\mathrm{r}G$. For a general reaction, it is related to the standard reaction Gibbs energy $\Delta_\mathrm{r}G^0$ and the reaction quotient Q by:

$$\Delta_\mathrm{r}G = \Delta_\mathrm{r}G^0 + RT \ln Q \tag{2.3}$$

In electrochemical processes operated at constant temperature and pressure, the free-energy change of the overall cell reaction can, in the ideal case, be entirely converted into electrical work. The maximum non-pV work is then:

$$\Delta_\mathrm{r}G = -zFE \tag{2.4}$$

where E is the cell potential and F the Faraday constant. Under standard conditions, the same relation defines the standard cell potential E^0. Com-

bining these expressions yields the Nernst equation in its general form:

$$E = E^0 - \frac{RT}{zF} \ln Q \tag{2.5}$$

For a generic redox couple, the reduction half-reaction can be written as

$$\mathrm{Ox} + z\,\mathrm{e}^- \rightleftharpoons \mathrm{Red} \tag{2.6}$$

where Ox and Red denote the oxidized and reduced forms of the species, respectively, and z is the number of transferred electrons. The corresponding oxidation reaction is obtained by reversing the arrow. The activity of electrons in the metallic electrode is effectively constant, so the reaction quotient reduces to $Q = a_{\mathrm{Red}}/a_{\mathrm{Ox}}$. The half-cell potential then reads:

$$E = E^0 - \frac{RT}{zF} \ln \frac{a_{\mathrm{Red}}}{a_{\mathrm{Ox}}} \tag{2.7}$$

At $T = 298.15$ K, this can be expressed in logarithms as:

$$E = E^0 + \frac{0.059\ \mathrm{V}}{z} \log_{10} \frac{a_{\mathrm{Ox}}}{a_{\mathrm{Red}}} \tag{2.8}$$

This is the original form of the Nernst equation for a single half-cell, linking the redox state of the couple directly to the electrode potential.

2.1.5. Electrochemical Kinetics and Interfacial Phenomena

A thermodynamic description of electrochemical equilibria and overpotential establishes the maximum driving force available for a given transformation but does not specify the rate at which charge and matter are transferred across the interface, as this is governed by the microscopic charge-transfer kinetics at the electrode-electrolyte interface. At this interface, electron transfer between the electronically conductive solid and solvated redox species proceeds via a sequence of proton-coupled electron-transfer steps, in which the transfer of an electron is often coupled to the transfer of a proton or other ion [Bard2001]. For a given elementary step,

the interfacial reaction rate can be expressed in terms of the current density j, which in compact form is described by the Butler-Volmer equation:

$$j = j_0 \left[\exp\left(\frac{\alpha_\mathrm{a} F \eta}{RT}\right) - \exp\left(-\frac{\alpha_\mathrm{c} F \eta}{RT}\right) \right], \tag{2.9}$$

where j_0 is the exchange current density, η the overpotential relative to the equilibrium potential of the considered half-reaction, F the Faraday constant, and $\alpha_\mathrm{a}, \alpha_\mathrm{c}$ the anodic and cathodic transfer coefficients, respectively [Bard2001]. The exchange current density j_0 quantifies the intrinsic charge-transfer activity of the interface under equilibrium conditions. It depends sensitively on the electronic structure of the electrode, the adsorption strength and coverage of reaction intermediates, as well as on the composition, temperature, and pH of the electrolyte. High j_0 values indicate facile charge transfer and small kinetic overpotentials at a given current density, whereas low j_0 values imply sluggish kinetics and large activation losses.

In the limit of large anodic or cathodic polarization, one of the exponential terms in Equation (2.9) dominates and the current-overpotential relation reduces locally to a Tafel-type expression. For cathodic control, this yields approximately

$$\eta \approx \frac{RT}{\alpha_\mathrm{c} F} \ln\left(\frac{|j|}{j_0}\right),$$

such that the Tafel slope $b_\mathrm{c} = (2.303\, RT)/(\alpha_\mathrm{c} F)$ provides direct access to the apparent transfer coefficient and thus to the symmetry of the activation barrier [Bard2001]. In practical polarization curves, the observed slope is often a convolution of intrinsic charge-transfer kinetics with ohmic losses and mass-transport limitations.

The local reaction environment at the interface is further shaped by the structure of the electric double layer (EDL) (Figure 2.4). Upon polarizing an electrode in an electrolyte, electronic charge accumulated in the metal is compensated by an excess of counter-ions in the adjacent solution phase,

giving rise to a compact layer of specifically adsorbed ions and solvent molecules (inner Helmholtz plane) and a more diffuse region of mobile ions extending over several Debye lengths into the bulk electrolyte [Plet2009]. The resulting steep potential drop across the compact layer and the adjacent diffuse layer modifies the effective driving force experienced by charged reactants and intermediates, affects their activity coefficients, and governs the local proton activity through H^+/OH^- partitioning between bulk and interface. Consequently, the rate and selectivity of interfacial reactions depend not only on the intrinsic catalytic properties of the surface but also on the composition and structure of the EDL, which can be tuned via supporting electrolyte, pH, and potential window. In operating electrochemical

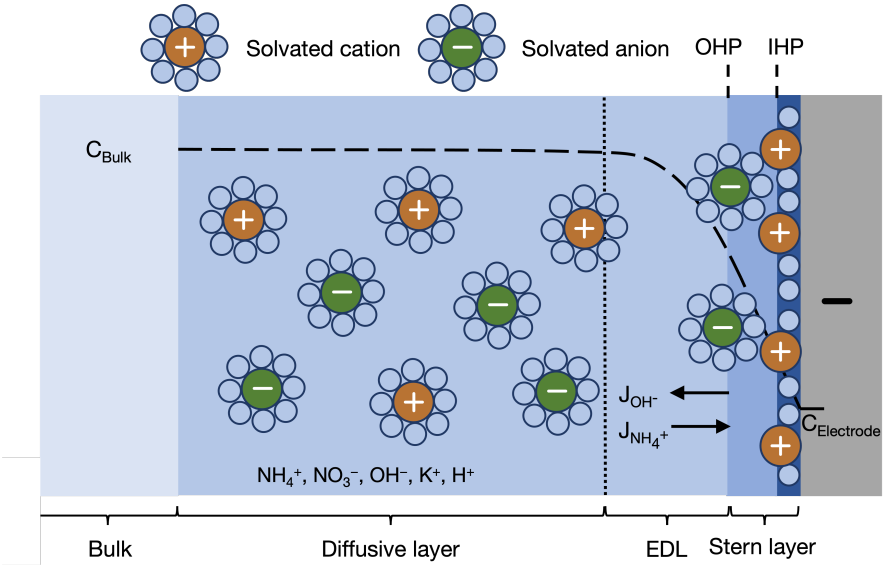

Figure 2.4.: Schematic depiction of the electrolyte interphase.

reactors, the measurable current density is therefore determined by an interplay between charge-transfer kinetics, the structure and dynamics of the EDL, and the supply and removal of reactants and products by mass transport.

2.1.6. Electrochemical Performance Indicators

The charge passed through an electrode during electrolysis is given by

$$Q = \int_0^{t_{\text{end}}} I(t)\,\mathrm{d}t, \tag{2.10}$$

with $i(t)$ the time-dependent current. Faraday's law of electrolysis relates this charge to the amount of substance formed or consumed at the electrode:

$$Q_k = n_k z_k F \tag{2.11}$$

where n_k is the amount of species k, z_k the number of electrons transferred in its formation (or consumption), and Q_k the fraction of the total charge used for this process [Bard2001; Schm2003]. In realistic systems, only part of the total charge contributes to the formation of the desired product because of competing side reactions such as the hydrogen evolution reaction (HER). The faradaic efficiency (FE) for a product k is defined as the ratio of the charge used for its formation to the total charge passed:

$$\mathrm{FE}_k = \frac{Q_k}{Q_{\text{tot}}} = \frac{n_k z_k F}{\int_0^{t_{\text{end}}} i(t)\,\mathrm{d}t}, \tag{2.12}$$

Following the ideally mixed model as described by Bäßler [Baes2025], a well-mixed electrolyte volume V with volumetric feed $\dot{V}_{\text{feed}}$, the current density j and inlet concentration c_{in} of a product species with concentration $c(t)$ is considered. The macroscopic mole balance is then given by:

$$V\frac{\mathrm{d}c(t)}{\mathrm{d}t} = \dot{V}_{\text{feed}}\big(c_{\text{in}} - c(t)\big) + \frac{jA\mathrm{FE}}{zF} \tag{2.13}$$

In batch mode, the feed flow rate vanishes, $\dot{V}_{\text{feed}} = 0$, such that Equation (2.13) reduces to:

$$V\frac{\mathrm{d}c(t)}{\mathrm{d}t} = \frac{jA}{zF}\,\mathrm{FE}(t) \tag{2.14a}$$

$$\mathrm{FE}(t) = \frac{zFV}{jA}\,\frac{\mathrm{d}c(t)}{\mathrm{d}t}, \tag{2.14b}$$

In practice, the time derivative is approximated by a finite difference between two sampling times t_{n-1} and t_n.

For feed-and-bleed operation, neither the feed flow nor the temporal change in concentration can be neglected. Rearranging Equation (2.13) and separating variables yields

$$\int_{c_{n-1}}^{c_n} \frac{\mathrm{d}c}{\frac{\dot{V}_{\text{feed}}}{V}\left(c_{\text{in}} - c\right) + \frac{jA}{zFV}\,\mathrm{FE}_n} = \int_{t_{n-1}}^{t_n} \mathrm{d}t = \Delta t_n \tag{2.15a}$$

$$-\frac{V}{\dot{V}_{\text{feed}}}\,\ln\left[\dot{V}_{\text{feed}}\left(c_{\text{in}} - c\right) + \frac{jA}{zF}\,\mathrm{FE}_n\right]_{c_{n-1}}^{c_n} = \Delta t_n, \tag{2.15b}$$

where $\Delta t_n = t_n - t_{n-1}$ and FE_n is assumed constant within the sampling interval $[t_{n-1}, t_n]$. Solving Equation (2.15b) for FE_n leads to the explicit expression for the FE in feed-and-bleed mode:

$$\mathrm{FE}_n = \frac{zF\dot{V}_{\text{feed}}}{jA}\left[\left(c_{n-1} - c_{\text{in}}\right) + \frac{c_n - c_{n-1}}{1 - \exp\left(-\frac{\dot{V}_{\text{feed}}}{V}\,\Delta t_n\right)}\right]. \tag{2.16}$$

For the typical case relevant in this work, the product is absent in the feed, i.e. $c_{\text{in}} = 0$. Equation (2.16) then simplifies to the discrete FE expression for feed-and-bleed operation neglecting this term [Baes2025].

The ammonia production rate was expressed as area-normalized molar

rate

$$\nu_{\mathrm{NH_3}} = \frac{\dot{n}_{\mathrm{NH_3}}}{A_{\mathrm{Cathode}}} \quad \left[\mathrm{mmol\,h^{-1}\,cm^{-2}}\right]. \tag{2.17}$$

2.1.7. Mass Transport in Liquid Electrolytes

Transport of ionic and molecular species in the electrolyte occurs through diffusion, migration, and convection. The molar flux J_i of species i can be described by the Nernst-Planck equation together with the Nernst-Einstein relation:

$$J_i = -\underbrace{D_i \nabla c_i}_{Diffusion} - \underbrace{z_i u_i F c_i \nabla \Phi}_{Migration} + \underbrace{c_i \mathbf{v}}_{Convection} \tag{2.18}$$

where D_i is the diffusion coefficient, c_i the concentration, u_i the ionic mobility, z_i the charge, Φ the electric potential, and **v** the fluid velocity vector. For mass transport in electrochemical systems, instead of the three dimensional flux, it is often more convenient to consider the one-dimensional flux normal to the electrode surface:

$$J_i = -D_i \frac{\partial c_i}{\partial x} - z_i u_i F c_i \frac{\partial \Phi}{\partial x} + c_i v(x), \tag{2.19}$$

At sufficiently high current densities, the reactant concentration at the electrode surface approaches zero, leading to a diffusion-limited regime characterized by the limiting current density:

$$j_{\mathrm{lim}} = zF D_i \frac{c_{i,\infty}}{\delta} \tag{2.20}$$

where δ is the hydrodynamic boundary-layer thickness. In electrochemical reaction engineering, the limiting current density is conveniently expressed using the mass-transfer coefficient k_m:

$$k_m = \frac{D_i}{\delta_{\mathrm{N}}} \tag{2.21}$$

while δ_N is the Nernst diffusion layer thickness, as defined as:

$$\delta_N = \sqrt{\pi D t} \tag{2.22}$$

This leads to an alternative expression for the limiting current density used in process engineering:

$$j_{lim} = zFk_m c_{i,\infty} \tag{2.23}$$

This regime can be identified by a plateau in the current-voltage curve, indicating that further increases in overpotential do not lead to higher current due to mass-transport constraints [Schm2003].

2.1.8. Hydrodynamics in Flow Cells and Porous Electrodes

The hydrodynamic operating regime in electrochemical flow cells and porous electrodes strongly influences species transport, reaction-zone thickness, and the residence time of intermediates. Flow behavior is commonly characterized by the Reynolds number

$$\mathrm{Re} = \frac{\rho u L}{\mu}, \tag{2.24}$$

where ρ is the fluid density, u a characteristic velocity, L a characteristic length scale (e.g. channel height or hydraulic diameter), and μ the dynamic viscosity. At low Re, the flow is typically laminar and mass transfer is dominated by diffusion and well-defined boundary layers, while higher Re can lead to transition and turbulence depending on the geometry [Schm2003]. For example, in aqueous systems the flow in a straight channel is laminar for Re < 2000 and turbulent for Re > 2300; for a plane slit, turbulence is observed for Re $\geq$ 2200-3600 [Schm2003].

Under diffusion-limited conditions, the reactant concentration at the electroactive surface approaches zero and the current density becomes controlled by mass transfer as defined in Equation (2.23). The correspond-

ing mass-transfer coefficient follows as

$$k_m = \frac{i_{\text{lim}}}{nFc_{i,\infty}}. \tag{2.25}$$

If the experimentally observed i_{lim} scales linearly with $c_{i,\infty}$ over a suitable concentration range, the process can be classified as diffusion-controlled, indicating that kinetic limitations are negligible under those conditions [Brow1994; Schm2003].

Porous electrodes such as open-cell foams are commonly characterized by their porosity ε and specific surface area A_e (electrochemically active surface area per unit volume of electrode). A useful geometric parameter is the hydraulic diameter d_h, which for such structures can be approximated as

$$d_h = \frac{4\varepsilon}{A_e}. \tag{2.26}$$

This effective length scale is then used to construct dimensionless numbers and correlations for flow and mass transfer in the porous structure [Brow1994; Lang1989a; Lang1989b; Lang1990a; Lang1990b].

In porous media, it is convenient to distinguish between the superficial velocity u_s and the interstitial velocity v_i. The superficial velocity is defined as

$$u_s = \frac{Q}{A_f}, \tag{2.27}$$

where Q is the volumetric flow rate and A_f is the macroscopic flow cross-sectional area. The interstitial velocity accounts for the reduced flow area inside the pores and is related to u_s by

$$v_i = \frac{u_s}{\varepsilon}. \tag{2.28}$$

Based on the hydraulic diameter d_h, one can define Reynolds numbers for

both superficial and interstitial flow:

$$\mathrm{Re}_s = \frac{\rho u_s d_h}{\mu} \tag{2.29a}$$

$$\mathrm{Re}_i = \frac{\rho v_i d_h}{\mu} \tag{2.29b}$$

These dimensionless numbers help classify the flow regime within the porous electrode and describe the mass-transfer [Brow1994].

Mass transfer in flowing electrolytes is often described using the Sherwood number Sh and the Schmidt number Sc,

$$\mathrm{Sh} = \frac{k_m d_h}{D} \tag{2.30a}$$

$$\mathrm{Sc} = \frac{\mu}{\rho D} \tag{2.30b}$$

where D is the diffusion coefficient of the electroactive species. The Sherwood number expresses the ratio of convective to diffusive mass transport, while the Schmidt number compares momentum diffusivity to mass diffusivity. In both channel and porous geometries, empirical or semi-empirical correlations are often fitted with a power law form:

$$\mathrm{Sh} = a\mathrm{Re}^b\mathrm{Sc}^c\Gamma^d, \tag{2.31}$$

where Γ is an additional dimensionless group accounting for geometric factors [Schm2003].

Overall, the combination of flow geometry, porosity, and operating flow rate determines the hydrodynamic regime and, through k_m, the extent of diffusion control in electrochemical flow cells and porous electrodes.

2.2. Ammonia Production Processes

Ammonia (NH_3) is a bulk commodity chemical with a central role in modern industrial society. Global production reached approximately 150 Mt in 2024 [Stat]. Around 80 % of this volume is used in agriculture, predominantly as nitrogen fertilizer, while the remaining 20 % is utilized in the manufacture of pharmaceuticals, dyes, plastics, explosives, and other chemical products [Eris2008]. The demand for NH_3 is projected to increase further, as ammonia is increasingly considered a carbon-free energy carrier for H_2 owing to its high volumetric energy density and established global logistics infrastructure [IREN2022]. Conventional ammonia synthesis is associated with a significant energy and carbon footprint, as it accounts for roughly 1.4 % of global primary energy consumption and about 1.2 % of anthropogenic CO_2 emissions [Appl2011; Smit2020; IEA2021]. The development of low-carbon or carbon-free ammonia production pathways is therefore a key objective in the context of sustainable chemical industry and decarbonization of the fertilizer sector.

Looking ahead, the demand for NH_3 is expected to increase not only due to rising global fertilizer requirements but also because ammonia is being considered as a carbon-free energy vector and hydrogen carrier in large-scale power and shipping applications. This prospective dual role as both a key nitrogen fertilizer and an energy carrier is directly linked to the favorable physicochemical properties of ammonia. At standard conditions, NH_3 is a colorless gas with a pungent odor. It is highly soluble in water, with a solubility of 531 g L^{-1} at 20 °C, forming ammonium ions NH_4^+ via the protolysis equilibrium characterized by an acid dissociation constant of pK_a = 9.25. At ambient pressure, ammonia condenses to a liquid at its normal boiling point of approximately –33 °C; at 20 °C, liquefaction requires pressures above about 9 bar [Hayn2017]. The combination of high water solubility and comparatively mild conditions for liquefaction enables both large-scale storage and transport of liquefied ammonia and its straightforward handling as an aqueous fertilizer solution, while simultaneously underpinning its suitability for distribution as an energy and hydrogen carrier.

Currently, about 94 % of global ammonia production is based on the Haber-Bosch (HB) process [Smit2020]. In the following, the conventional HB route employing fossil-derived hydrogen via steam methane reforming (SMR), its adaptation using electrolytic hydrogen, and direct electrochemical nitrogen reduction reaction (eNRR) are outlined and compared in terms of specific energy demand, CO_2 emissions, and techno-economic implications.

2.2.1. Grey Haber–Bosch process

The industrial HB process, developed by Fritz Haber and Carl Bosch, was commercialized in the early twentieth century. The HB process synthesizes ammonia by reacting dinitrogen from air and hydrogen over a heterogeneous catalyst at elevated temperature and pressure (Equation (2.32)). The catalyst is typically iron-based and promoted with potassium, aluminum, and calcium oxides in order to enhance activity and stability under industrial conditions [Bohn2003; Smit2020]. The process is operated under severe conditions, typically 400 to 500 °C and 10 to 30 MPa, which are required to activate the very stable N≡N triple bond and to achieve economically viable reaction rates at acceptable single-pass conversions.

$$N_2 + 3\,H_2 \xrightarrow[20\,\mathrm{MPa}]{450\,^\circ\mathrm{C}} 2\,NH_3 \tag{2.32}$$

The HB synthesis loop is tightly integrated with hydrogen generation via steam methane reforming (SMR), which currently constitutes the dominant route to hydrogen for ammonia production. In SMR, methane is reacted with steam at high temperatures to form carbon monoxide and hydrogen, followed by the water–gas shift reaction to convert carbon monoxide to CO_2 and additional hydrogen. On average, the combined SMR–HB route emits approximately 2.9 kg of CO_2 per kilogram of NH_3. In large-scale, state-of-the-art plants reach specific emissions as low as 1.6 kg CO_2 per kilogram of NH_3 [Smit2020].

Because SMR is strongly endothermic, the overall primary energy de-

mand of the conventional HB process is substantial. The theoretical minimum energy requirement is about 22.2 GJ t^{-1} of NH_3, whereas the chemical energy stored in one tonne of ammonia corresponds to approximately 18.6 GJ [Smit2020]. Modern large-scale plants achieve specific energy consumptions as low as 27.4 GJ t^{-1} of NH_3, corresponding to an overall energy efficiency on the order of 68 %. The resulting production costs typically range from about $300 to $1 000 per ton of NH_3, depending primarily on the natural gas price and plant scale, with the levelized cost of hydrogen from SMR being approximately $1.28 per kilogram [Smit2020; Wang2021]. The application of carbon capture and storage to mitigate CO_2 emissions would add roughly $120 per ton of captured CO_2, thereby increasing the overall cost of ammonia [Smit2020]. In consequence, the conventional SMR–HB route represents both the current industrial benchmark and a key target for decarbonization via alternative hydrogen sources.

2.2.2. Green Haber–Bosch process

A conceptually straightforward route to decarbonize ammonia production is to replace fossil-based hydrogen from SMR with ”green” hydrogen generated via water electrolysis powered by renewable electricity. Commercial proton exchange membrane and alkaline electrolyzers have demonstrated high FE and overall energy efficiencies exceeding 65 % under industrially relevant operating conditions [El-S2023]. In such a configuration, the HB synthesis loop remains largely unchanged, while upstream hydrogen generation is decoupled from fossil carbon sources and, in principle, rendered nearly carbon-free.

With current electrolyzer technologies, the total primary energy demand for HB ammonia production based on electrolytic hydrogen increases to roughly 38.2 GJ t^{-1} of NH_3, whereas the theoretical minimum energy requirement for this route is lower than for SMR-based HB, at approximately 21.3 GJ t^{-1} of NH_3 [Smit2020; Wang2021]. The specific CO_2 emissions of such an electrolysis–HB process depend sensitively on the carbon intensity of the electricity mix. A break-even point relative to state-of-the-art

SMR-based plants is estimated at an electricity-related emission factor of about 167 g kW^{-1} h. When powered by low-carbon electricity from wind, specific emissions can, in principle, be reduced to approximately 0.12 to 0.53 kg CO_2 per kilogram of NH_3 [Smit2020].

Despite the potential for deep emission reductions, the cost of hydrogen from present-day electrolyzers remains comparatively high, with reported values in the range of \$5 to \$10 kg_{H_2}, largely driven by electricity costs and limited operating hours at high renewable capacity factors [Smit2020; Wang2021]. Price parity with SMR-derived hydrogen would require electricity prices on the order of \$0.01 kW^{-1} h, which is well below typical market prices. Consequently, further improvements in electrolyzer efficiency, capital cost, and dynamic operating flexibility, together with access to low-cost renewable electricity, are essential prerequisites for the large-scale deployment of HB plants based on green hydrogen.

2.2.3. Electrochemical Nitrogen Reduction

Instead of combining N_2 with externally supplied H_2 in the HB loop, an alternative concept is the direct eNRR, in which N_2 is reduced to NH_3 using water as the proton source in a single electrochemical step. In principle, such a process could couple renewable electricity directly to ammonia synthesis and thereby eliminate both the SMR unit and the conventional HB synthesis loop. The minimum energy requirement of this route is theoretically as low as 19.9 GJ t^{-1} of NH_3, i.e. below that of both SMR-based and electrolysis-based HB routes [Smit2020]. In practice, however, current eNRR systems exhibit extremely low FE, low partial current densities for NH_3, and poor overall energy efficiency.

The fundamental challenge arises from the high bond dissociation energy of the N≡N triple bond and the associated sluggish kinetics of N_2 activation on most catalyst surfaces. The elementary steps of N_2 adsorption, bond weakening, and subsequent proton-electron transfer are kinetically demanding and typically proceed with high overpotential. Furthermore, in aqueous electrolytes the thermodynamic potential for N_2 reduction is

close to that of the HER, so that HER generally dominates as a competing side reaction and severely limits the FE toward NH_3. Additional constraints include the low solubility and slow mass transport of N_2 in aqueous electrolytes, which further restrict achievable current densities and aggravate mass-transfer limitations at the electrode surface. As a result, reported eNRR systems frequently operate in a regime where most of the supplied charge is consumed by HER, and the rate of NH_3 formation remains several orders of magnitude below technologically relevant values.

In summary, conventional HB synthesis based on SMR is a mature and energy-intensive technology with a substantial carbon footprint. Replacing fossil hydrogen with electrolytic hydrogen enables a significant reduction in CO_2 emissions but is presently constrained by high electricity and hydrogen costs. Direct electrochemical N_2 reduction offers an appealing theoretical minimum energy demand and a conceptually elegant process route but remains limited by fundamental kinetic and selectivity challenges, as well as unfavorable mass-transport characteristics in conventional electrolytes [Smit2020].

2.2.4. Nitrate recovery from wastewater streams

In addition to nitrogen fixation by the HB process, large quantities of reactive nitrogen are already present in anthropogenic material cycles as oxidized nitrogen species, in particular nitrate NO_3^-, in surface waters, groundwater, and engineered wastewater systems. Nitrate pollution contributes to eutrophication, hypoxic zones in aquatic ecosystems, and deterioration of drinking water quality, and it is therefore subject to stringent regulatory limits in many jurisdictions. At the same time, this dispersed NO_3^- inventory represents a substantial secondary nitrogen resource that is currently largely dissipated by conventional removal technologies. Recovering nitrate from wastewater streams and converting it into ammonia thus aligns with concepts of a circular nitrogen economy, in which legacy nitrogen pollution is remediated while displacing part of the primary HB demand [vLang2021].

Nitrate-containing wastewaters arise from a range of point and non-point sources. A major contribution stems from the agriculture sector, where nitrification of ammonium fertilizers and subsequent leaching lead to nitrate-enriched groundwater and surface waters, as well as agricultural drainage and tile-drain runoff with nitrate concentrations often in the 1 to 10 mg L^{-1}-N range and above. Additional nitrogen loads originate from intensive livestock farming and manure handling. In municipal wastewater treatment plants, biological nitrification converts ammonium to nitrate in secondary effluents; depending on process configuration, residual NO_3^- concentrations of several tens of mg L^{-1}-N are common. Industrial sectors such as fertilizer and explosives manufacturing, metal finishing, and food processing can generate process effluents with substantially higher nitrate concentrations, in some cases up to the g L^{-1} range [vLang2021].

Historically, the primary objective for these nitrate-rich streams has been removal rather than recovery. Established technologies include biological denitrification and anaerobic ammonia oxidation, which convert NO_3^- to dinitrogen, as well as physicochemical separation processes such as reverse osmosis, nanofiltration, electrodialysis, and ion exchange using nitrate-selective resins [Abas2022]. In many of these processes, nitrate is transferred from the bulk stream into a secondary brine or regenerant solution. For example, ion exchange followed by regenerant recovery and electrodialysis can concentrate nitrate by more than an order of magnitude, yielding eluates with NO_3^- concentrations on the order of 100 mM to 150 mM from influent streams initially below 10 mM [Simo2025]. Such enrichment not only facilitates compliant disposal but also generates side streams that are attractive as electrochemical feedstocks.

The electrochemical nitrate reduction reaction (eNO_3RR) provides a means to couple nitrate removal from wastewater with the synthesis of ammonia as a value-added product. Compared to N_2, nitrate is already in an oxidized state and exhibits more favorable thermodynamics and kinetics for reduction to NH_3, which lowers the required cell voltage and can enable higher reaction rates under otherwise comparable conditions. In this context, nitrate-laden wastewaters and concentrates can serve as

an alternative nitrogen feedstock, where eNO_3RR simultaneously reduces pollution and recovers usable nitrogen in the form of ammonia. Recent studies have demonstrated that integrating separation and reaction, for example through electrochemical separations that combine electrodialysis with eNO_3RR, can achieve near-complete nitrate removal while producing concentrated ammonia solutions suitable for direct use as liquid fertilizers [Guo2024].

From a reactor engineering perspective, the composition of realistic wastewater feedstocks poses significant challenges for electrochemical conversion. Decentralized wastewaters typically exhibit low nitrate concentrations (< 10 mM), low ionic conductivity, and complex backgrounds of competing ions and organic matter, conditions that are unfavorable for high-rate eNO_3RR [Huan2024a]. Pre-concentration by ion exchange, electrodialysis, or related membrane processes provides a strategy to bridge this gap by generating nitrate-rich, high-conductivity electrolytes that more closely resemble the conditions used in fundamental electrocatalysis studies. An increase of NO_3 concentration from 10 mM in raw wastewater to 150 mM in a concentrated side stream can therefore raise the performance significantly.

These considerations directly motivate the use of zero-gap electrochemical reactors with membrane electrode assemblies (MEAs) for eNO_3RR. In zero-gap configurations, the catalyst-coated electrode is pressed directly against an ion-conducting membrane, minimizing the distance between the reaction zone and the membrane and thereby reducing ionic resistance. Efficient operation of such reactors requires sufficiently high reactant concentrations at the catalyst surface to sustain industrially relevant current densities. Nitrate-enriched side streams generated by ion exchange, electrodialysis, or similar processes are therefore well suited as feeds for zero-gap eNO_3RR cells, enabling compact reactor designs that integrate pollutant removal and ammonia synthesis.

3.

MOF-derived Carbon for Electrochemical Nitrogen Reduction

3.1. Introduction

Ammonia (NH_3) is not only the backbone of global fertilizer production but is also emerging as a promising energy carrier due to its high hydrogen content, carbon-free combustion, and compatibility with existing infrastructure [Boer2019; IREN2022; IEA2025]. The conventional Haber-Bosch (HB) process, while technically mature, remains one of the largest single-point sources of CO_2 emissions worldwide. This is primarily due to its dependency on hydrogen from fossil-based reforming and the energy-intensive nature of its operation (typically 500 °C and 20 to 35 MPa) [MacF2020]. In 2010, ammonia synthesis alone accounted for over 1 % of global energy consumption and more than 450 Mt of CO_2 emissions annually [IREN2022].

Despite efforts to decarbonize ammonia production via renewable-powered electrolysis (“green HB”), such approaches inherit the scale and capital intensity of conventional HB, requiring both electrolyzers and thermochemical reactors. Moreover, HB plants are only economically viable at large scale and near fossil resources such as natural gas, while most regions with abundant renewable energy are geographically disconnected from industrial ammonia production [MacF2020]. To address these challenges, the (electrochemical nitrogen reduction reaction (eNRR)) is being explored as a distributed, modular alternative for NH_3 synthesis. This process converts atmospheric N_2 and water into ammonia under ambient conditions [Skúl2011]:

$$N_2 + 6\,H_2O \longrightarrow 2\,NH_3 + 3\,O_2 \qquad E^\circ \approx 1.17\,\text{V vs. RHE} \tag{3.1}$$

The appeal of eNRR lies in its potential to couple renewable electricity with low-temperature electrolysis, bypassing the need for separate hydrogen generation and high-pressure reactors. However, the realization of efficient eNRR remains a significant scientific challenge due to the high kinetic barrier associated with cleaving the N≡N triple bond (bond enthalpy 941 kJ mol^{-1}) and the competitive hydrogen evolution reaction (HER), which dominates under cathodic conditions [MacF2020].

Catalyst development for eNRR has spanned a wide range of material

classes including transition metals (e.g., Fe, Mo, Ru), metal nitrides and carbides, and metal-free doped carbons. Among these, iron-based materials are particularly attractive owing to their low cost, abundance, and known capacity for N_2 activation as demonstrated in the classical HB process. Nevertheless, most Fe-based eNRR catalysts suffer from limited selectivity and low NH_3 yields, often attributed to HER suppression challenges and insufficient active-site accessibility [Yi2020; Wei2021].

A promising approach to enhance eNRR performance involves the utilization of Metal-Organic-Frameworks (MOFs) as precursors to fabricate tailored electrocatalysts. MOF-derived carbon materials combine exceptionally high surface areas, tunable porosity, and the ability to generate atomically dispersed or nanoscale metal species embedded in conductive carbon matrices. Upon thermal treatment under inert atmosphere (pyrolysis), MOFs decompose into partially graphitized carbon structures while preserving the dispersion and coordination environment of their metal centers [Oar-2017]. By selecting nitrogen-free organic linkers, the resulting carbon matrices are devoid of intrinsic nitrogen species, thereby eliminating false-positive NH_3 signals in post-reaction quantification.

In recent years, MOFs and their derivatives have emerged as a central design platform for eNRR electrocatalysts due to their modular coordination chemistry, high porosity, and structural tunability. The well-defined metal nodes and organic linkers allow atomic-level control over active sites and adsorption environments, which is crucial for activating the inert $N \equiv N$ bond [He2022].

Monometallic MOFs such as NH_2-MIL-88B (Fe), HKUST-1 (Cu), and MIL-100 (Al) have demonstrated eNRR activity under ambient conditions, yet their poor intrinsic conductivity and structural instability severely restrict charge transport and long-term operation [He2022]. For instance, MIL-100 (Al) achieved a production rate of $1.06 \cdot 10^{-9}\,\mathrm{mol\,s^{-1}\,cm^{-2}}$ with a Faradaic efficiency of 22.6 % in alkaline electrolyte. Conductivity improvements through hybridization with conductive scaffolds (e.g., carbon nanotubes or MXenes) have been shown to enhance performance by promoting interfacial charge transfer. Two-dimensional MOFs, such as ultra-thin In-MOF

nanosheets with a thickness of 1.3 nm, further increase active-site exposure and mass transport, resulting in rates up to $2.2 \cdot 10^{-9}$ mol s^{-1} cm^{-2} at −0.2 V vs. reversible hydrogen electrode (RHE) [He2022]. Among transition-metal-based systems, Fe-containing catalysts have consistently shown superior eNRR activity owing to the half-filled $3d$ orbitals of Fe that facilitate N_2 adsorption via back-donation into the antibonding π^* orbitals [Fan2022b]. At elevated temperatures (90 °C), Fe-MOFs achieved rates up to $2.12 \cdot 10^{-9}$ mol s^{-1} cm^{-2} with a Faradaic efficiency of 1.43 %, outperforming their Co- and Cu-based counterparts [He2022]. This intrinsic activity aligns with the mechanistic role of Fe in the Haber-Bosch process, highlighting its potential as an active center for electrochemical nitrogen activation.

Nevertheless, the limited electrical conductivity and instability of pristine MOFs remain key bottlenecks. Pyrolyzing these frameworks under controlled conditions transforms them into conductive, graphitic matrices with atomically dispersed or nanoparticulate Fe species (e.g., Fe_3C, Fe-C, or Fe-O domains) while preserving the original spatial distribution of the metal centers [Oar-2017]. The resulting MOF-derived catalysts are structurally diverse. Depending on the pyrolysis temperature, gas atmosphere, and precursor identity, the active phases can range from atomically dispersed Fe$-N_x$ sites to encapsulated Fe_3C or metallic iron nanoparticles. These phases differ markedly in their accessibility, stability, and catalytic behavior. For instance, thinly encapsulated iron particles may offer long-term structural durability but reduced electrolyte access, whereas exposed Fe domains can provide higher apparent activity at the cost of agglomeration or oxidation [Velá2011; Weze2016].

Particularly promising are MOF-derived single-atom catalysts, which combine atomic dispersion of active centers with conductive carbon matrices formed during pyrolysis. Agour *et al.* [Agou2023] synthesized Fe single-atom catalysts supported on N-doped carbon nanosheets (FeSAC-N-C) using Fe-doped carbon quantum dots as precursors. The resulting catalyst achieved a Faradaic efficiency of 23.7 % and an ammonia yield rate of $5.66 \cdot 10^{-8}$ mol s^{-1} cm^{-2} at −0.1 V vs. RHE in 0.1 M KOH. Density

functional theory (density functional theory (DFT)) calculations confirmed that Fe-N_x coordination sites lower the free-energy barrier for the rate-limiting protonation step, enabling superior N_2 adsorption and activation. Similar Fe-N-C configurations have been observed to outperform nanoparticulate Fe catalysts by suppressing HER and stabilizing reaction intermediates. These findings substantiate the potential of MOF-derived Fe single-atom systems as efficient eNRR catalysts.

Despite these advances, most reported MOFs-derived catalysts contain nitrogen from organic linkers, which may release nitrogen species under reductive potentials, leading to spurious NH_3 formation signals. Andersen *et al.* [Ande2019] and Choi *et al.* [Choi2020] have highlighted the critical need for rigorous control experiments, including Ar-purged electrolytes and $^{15}N_2$-labeling, to exclude such artifacts. Andersen's isotopic protocol demonstrated that many previously claimed aqueous eNRR systems show no measurable NH_3 formation above background levels, with apparent yields below $1 \cdot 10^{-11}\,\mathrm{mmol\,s^{-1}\,cm^{-2}}$. Similarly, Choi *et al.* [Choi2020] emphasized that nitrogen-containing catalysts (e.g., metal nitrides or N-doped carbons) may leach labile nitrogen under reductive potentials, leading to spurious ammonia detection.

In this context, nitrogen-free MOF-derived carbon catalysts present a unique opportunity to unambiguously assess intrinsic eNRR activity. By employing nitrogen-free organic linkers, e.g., trimesic acid in MIL-100 (Fe), one can obtain Fe-containing graphitic carbons devoid of lattice nitrogen. These systems provide isolated Fe centers embedded in conductive carbon matrices, ensuring that any detected NH_3 originates exclusively from electrochemical N_2 reduction. However, in the absence of nitrogen coordinating the metal centers, metal nanoparticles are less stabilized, which can promote sintering or aggregation during pyrolysis and operation and thus affect active-site dispersion, accessibility, and catalytic behavior.

In this chapter, the synthesis of a MOF-derived Fe catalyst MIL-100 (Fe) is investigated and its usage in eNRR shown. The emphasis is placed on the correlation between pyrolysis conditions, phase composition, and electrochemical performance in order to elucidate the active sites respon-

sible for ammonia formation under rigorously controlled, nitrogen-free conditions.

3.2. Experimental

3.2.1. Materials

All reagents were used as received without further purification. Sodium hydroxide (NaOH), sodium salicylate ($C_7H_5NaO_3$), trisodium phosphate dodecahydrate ($Na_3PO_4 \cdot 12\,H_2O$), sodium nitroprusside dihydrate ($Na_2[Fe(CN)_5NO] \cdot 2\,H_2O$), and sodium hypochlorite (NaOCl) were purchased from Sigma-Aldrich (Germany). All aqueous solutions were prepared with deionized water (resistivity > 18.2 $M\Omega\,cm^{-1}$). Nafion™ N117 (5 wt%) (Sigma-Aldrich) and ethanol (EtOH, 99.8%) (Carl Roth) were used for the preparation of catalyst inks. Electrochemical measurements were conducted using a Metrohm Autolab PGSTAT202N potentiostat. For the LSV measurements, a glassy carbon rotating disc electrode (RDE, Metrohm) was employed as working electrode, a platinum sheet (1 cm^2, Metrohm) as counter electrode, and an Ag/AgCl (3 M KCl, Metrohm) double junction electrode as reference. For gas diffusion electrode (GDE) experiments, a platinum sheet from Umicore served as counter electrode. All chemicals were of analytical grade.

3.2.2. MOF Synthesis

MIL-100 (Fe) was synthesized according to a modified solvothermal procedure. In a typical synthesis, 1.67 g trimesic acid (H_3BTC) was partially dissolved in 120 mL of 0.2 M sodium hydroxide solution using ultrasonic agitation for 30 min. Subsequently, 2.26 g $FeCl_2 \cdot 4\,H_2O$, fully dissolved in deionized water, was added dropwise under continuous stirring to the partially dissolved H_3BTC. The mixture was stirred at room temperature for the duration of the reaction. The obtained MIL-100 (Fe) was separated by centrifugation, washed three times with deionized water and once with ethanol, and dried in air overnight. The resulting powder was further dried under vacuum before further use.

3.2.3. Ammonia Quantification

Ammonia quantification was performed by the indophenol blue method. Three stock solutions were prepared. First a solution of 4 M NaOH. Second, the color reagent consisted of 1.6 g sodium salicylate ($C_7H_5NaO_3$), 2 g trisodium phosphate dodecahydrate ($Na_3PO_4 \cdot 12\,H_2O$), and 0.025 g sodium nitroprusside dihydrate ($Na_2[Fe(CN)_5NO] \cdot 2\,H_2O$) dissolved in 50 mL deionized water. Third, the sodium hypochlorite solution was prepared from 0.5 mL 5 % NaOCl diluted with 10 mL deionized water. For each analysis, 1.0 mL of the sample was mixed with 0.25 mL sodium hydroxide solution, 1.0 mL color reagent, and 0.25 mL sodium hypochlorite solution. The mixture was shaken thoroughly, and the absorbance was measured via UV/vis (Genesys™ 150 λ=652 nm) after color development. Calibration was carried out by recording a eight-point calibration curve.

3.2.4. LSV Measurements

Catalyst inks were prepared by dispersing the hand-ground catalyst powder in ethanol containing 5 wt% Nafion™ N117. The suspension contained 10 wt% catalyst with respect to the solvent and was ultrasonicated for 5 min to obtain a homogeneous dispersion. The ink was drop-cast onto a glassy carbon rotating disc electrode tip (Metrohm) and dried in air, resulting in a catalyst loading of 1 mg cm^{-2}. Linear sweep voltammetry (LSV) experiments were conducted in 0.1 M KOH electrolyte. The electrolyte was purged with high-purity nitrogen (N_2 7.0) or argon for at least 30 min prior to each measurement. The gas feed was purified in accordance with Andersen[Ande2019]. The nitrogen feed was guided through sequential gas purification traps containing 0.1 M KOH and 0.1 M $KMnO_4$ solutions to remove trace nitrogen oxides. All LSV measurements were compensated for 80% of the *iR*-drop, which was determined via electrochemical impedance spectroscopy (EIS) at the respective open-circuit potential. EIS was measured in the frequency range from 1 mHz to 1 Hz with an amplitude of 10 mV. The scan rate for LSV measurements was 50 mV s^{-1}. The working electrode potential was measured versus the Ag/AgCl (3 M KCl)

reference electrode and converted to the RHE scale.

3.2.5. Gas Scrubbing Setup

All electrochemical experiments involving nitrogen gas utilized a gas purification system to eliminate traces of nitrogen oxides and ammonia that could bias the eNRR or ammonia quantification. The gas scrubbing train was assembled according to the literature protocol by Andersen [Ande2019]. High-purity nitrogen (7.0) was first passed through a washing bottle containing 0.1 M KOH to remove acidic impurities, followed by a second trap containing 0.1 M $KMnO_4$ in alkaline medium to oxidatively remove nitrogen oxide species. Downstream of the cell, the gas outlet was connected to an acid trap filled with 0.5 M H_2SO_4 to collect volatilized ammonia species generated during electrolysis. This configuration ensured both feed gas purity and accurate quantification of ammonia formation.

3.2.6. Gas Diffusion Electrode Preparation

Catalyst-coated gas diffusion electrodes were prepared via airbrush spraying. For ink preparation, 320 mg of the catalyst powder were dispersed in 80 mL isopropanol and 400 mg (392 µL) Nafion™suspension (20 wt%) using an ultrasonic finger for 2 min. The dispersion was then sprayed onto carbon paper placed on a 120 °C hot plate under vacuum fixation. Spraying was continued until a catalyst loading of 3 mg cm^{-2} was achieved. The electrodes were cooled to room temperature and subsequently dried at 135 °C and 10 mbar for 1 h.

3.2.7. Constant Potential Electrolysis

Constant potential electrolysis experiments were performed in a gas diffusion electrode (GDE) cell using the spray-coated GDE as cathode and a platinum sheet anode (Umicore) with a surface area of 1 cm^2. The cell was separated using a cation exchange membrane (CEM) (Fumasep® F14100). The catholyte consisted of 0.1 M KOH solution. The nitrogen feed (7.0) was

introduced at a volumetric flow rate of 50 mL min^{-1} through the gas purification system described above (Figure 3.1). A pressure valve was used to adjust the backpressure such that the gas stream was forced through the GDE into the catholyte, ensuring optimal gas-liquid contact. The electrolyte was circulated at 100 mL min^{-1}. After the system reached the open-circuit potential (OCP) and a blank measurement was recorded, a constant potential of –0.1 V versus RHE was applied for 2 h. The gas outlet was directed through a 0.5 M H_2SO_4 trap to capture gaseous ammonia formed during electrolysis. After each experiment, both the electrolyte and the acid trap were analyzed for ammonia by the indophenol blue method as described above.

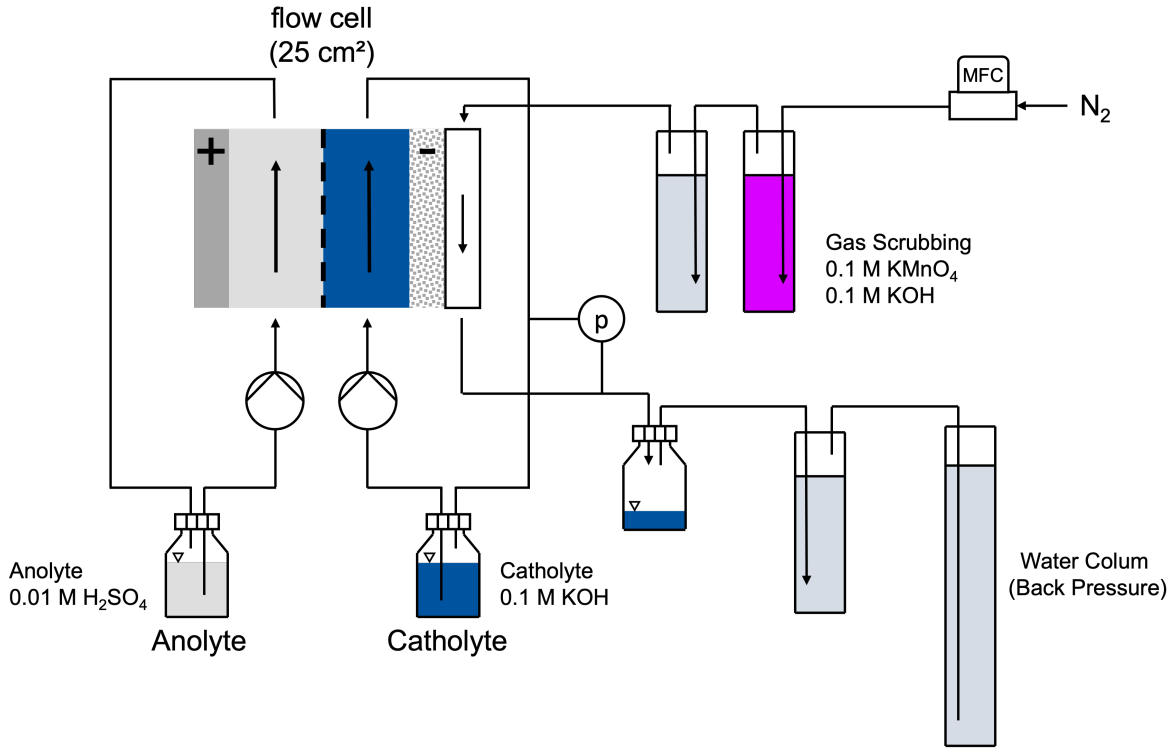

Figure 3.1.: Schematic of the used GDE setup including gas purification system for nitrogen feed and acid trap for ammonia collection.

3.3. Results and Discussion

3.3.1. Structural Characterization of MIL-100 and Basolite F300

The crystalline structure of the self-synthesized MIL-100 (Fe) was examined and compared to the commercially available Basolite®F300 and to the calculated reference pattern of MIL-100(Fe) reported by Horcajada and Férey et al. [Horc2007]. The reference structure was obtained from high-resolution synchrotron X-ray diffraction (XRD) data, where MIL-100(Fe) was described as an iron(III) carboxylate composed of Fe^{III} trimers of edge-sharing octahedral linked by benzene-1,3,5-tricarboxylate (BTC) ligands [Horc2007]. The resulting supertetrahedral network adopts a zeolitic topology, forming two types of mesoporous cages with free apertures of approximately 25 Å and 29 Å, consisting of smaller microporous pentagonal or hexagonal windows of 5.5 Å and 8.6 Å, respectively, that are formed by the mentioned iron trimers with ligand.

The experimental diffraction patterns are shown in Figure 3.2 The calculated pattern exhibits its strongest reflections below 12°, which correspond to the ordered arrangement of the two cage types in the crystalline framework. For the self-synthesized MIL-100 (Fe), the first reflection expected at $2\theta = 2.1°$ lies below the detection limit of the used XRD. Nevertheless, a distinct series of low-angle peaks can be assigned to the characteristic lattice planes of MIL-100 (Fe). The diffraction maxima at $2\theta = 4.0°$, 4.8°, 5.3°, 5.8°, and 6.3° reproduce the sequence and partially relative intensities of the reference pattern, demonstrating the successful formation of the target crystalline phase. The main predicted peaks at the low-angle region of $2\theta = 3.5°$ and 4.0° that originate from the main windows in the MOF can be seen as a weak shoulder at $2\theta = 3.5°$ and a sharp signal at $2\theta = 4.0°$. Additional reflections at $2\theta = 10.3°$ and 11.0° appear as well-resolved peaks, consistent with the reported MIL-100 (Fe) structure. Weak signals were further detected up to 20°, including a peak at 18.8° that is common to both materials and an additional reflection at 20.2° that is unique to the

self-synthesized MIL-100 (Fe).

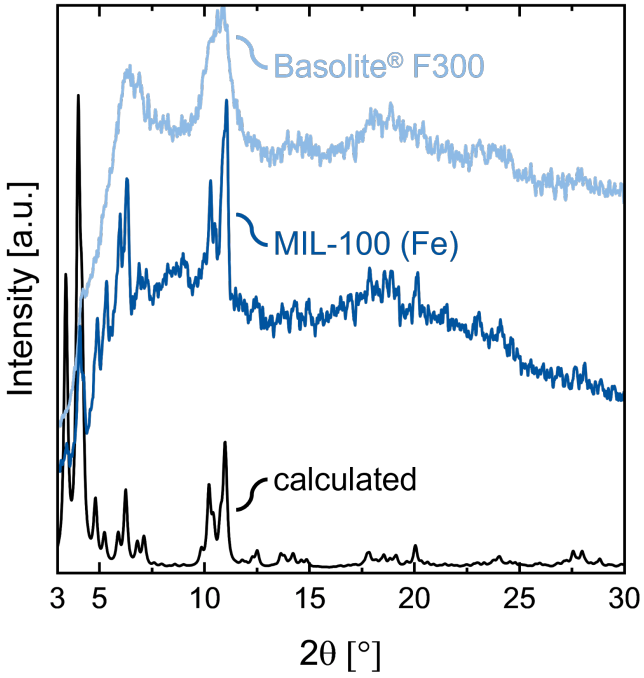

Figure 3.2.: XRD pattern of hydrothermally synthesized MIL-100 (Fe) , commercially available Basolite® F300, and the calculated pattern adapted from Horcajada[Horc2007] (CCDC 640536) with Cu K_α source.

In contrast, the pattern of Basolite®F300 reveals substantially broader and less intense reflections, indicating a lower degree of long-range order. Only a broad maxima is discernible in the range from $2\theta = 4°$ to 7°, overlapping with the main reflections of MIL-100(Fe). In the low-angle region, the distinct peaks at $2\theta = 4.8°$, 5.3°, and 5.8° observed for MIL-100(Fe) appear as a single broad feature for Basolite F300®. The two signals around 11.0° are not resolved and merge into a single, diffuse reflection. These differences in peak sharpness and multiplicity clearly indicate an enhanced crystallinity and structural ordering in the self-synthesized MIL-100 (Fe). The pronounced line broadening of the Basolite® F300 reflections can be attributed to smaller coherent scattering domains and partial amorphization of the framework.

Both samples show an increased background intensity in the diffraction pattern, which is mainly caused by x-ray fluorescence of iron under Cu K_α

irradiation. Although being aware of this, copper was still employed as the x-ray source, since it is commonly used in the literature. The elevated background and resulting noise level obscure potential minor impurity phases, but no additional crystalline reflections were detected within the sensitivity of the measurement. Therefore, both materials can be regarded as phase-pure within the detection limits of XRD.

In addition to the structural characterization, the specific surface area of both materials was determined by nitrogen physisorption. The Brunauer-Emmett-Teller (BET) surface area of the self-synthesized MIL-100 (Fe) amounts to 2132 $m^2 g^{-1}$, of which 2014 $m^2 g^{-1}$ originate from micropores. In comparison, the commercially available Basolite® F300 exhibits a significantly lower BET surface area of 1524 $m^2 g^{-1}$ and a micropore contribution of only 1021 $m^2 g^{-1}$. The high surface area and microporosity of the self-synthesized MIL-100 (Fe) underline its high crystallinity and well-developed porous framework, in agreement with the results from XRD. This large accessible surface is particularly advantageous for the subsequent thermal conversion to MOF-derived carbon.

The overall comparison confirms that the hydrothermal synthesis route yielded a MIL-100 (Fe) material with higher structural order and better correspondence to the ideal framework than the commercially available Basolite® F300. The sharper reflections and the presence of multiple low-angle peaks characteristic of the zeolitic topology demonstrate the successful formation of a highly crystalline MOF precursor suitable for subsequent thermal transformation. The structural coherence of the MIL-100 framework is expected to promote uniform carbonization behavior and to facilitate the preservation of the pore architecture during pyrolysis, providing a favorable starting point for the formation of conductive, iron-containing carbon materials for electrochemical nitrogen reduction.

3.3.2. Structural Evolution During Pyrolysis

The structural evolution of the MIL-100(Fe) framework during thermal treatment was analyzed by XRD (Mo Kα) of samples carbonized between 300 °C

and 1000 °C. The diffraction patterns, shown in Figure 3.3, reveal a distinct transformation of the crystalline phase with increasing pyrolysis temperature above the stability window of MIL-100(Fe). The parent MOF is reported stable up to approximately 270 °C.[Horc2007] Beyond this temperature the organic linker decomposes and the long-range crystallinity of the MOF collapses. In that case, the carbonized samples represent transformation products of the pristine framework.

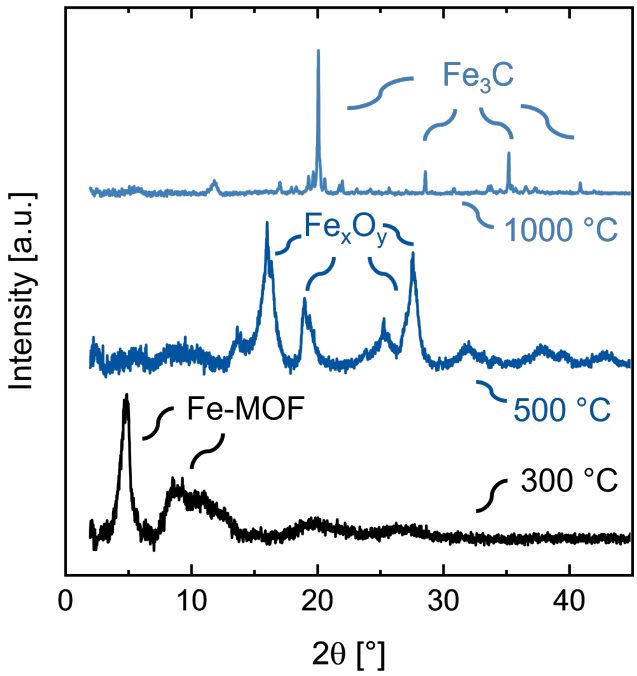

Figure 3.3.: Temperature-dependent XRD patterns (Mo Kα) of MIL-100(Fe)-derived carbons after pyrolysis at 300 °C, 500 °C, and 1000 °C. Fe_3O_4(ICSD-26410), Fe_3C(ICSD-99002). Mo K_α raditation.

At 300 °C, the pattern shows broad low-angle reflections at 2θ=4.9° and 8.9°, consistent with residual MOF-related order and the onset of framework collapse. Upon increasing the pyrolysis temperature to 500 °C, mixed iron oxides emerge. Reflections appear at 2θ=16.1°, 19.0°, 25.3°, and 27.6°, in good agreement with Fe_3O_4 (ICSD #26410), indicating a poorly crystalline magnetite-rich phase. The pronounced line broadening and elevated background suggest small oxide domains embedded in a partially amorphous carbon matrix and incomplete carbonization, which is consis-

tent with the low electrical conductivity observed for these materials.

At 1000 °C, the pattern changes markedly and exhibits sharp reflections at 2θ=12.1°, 28.7°, 35.3°, and 41.0°. These positions match iron carbide (Fe_3C) (ICSD #99002) and are close to the principal metallic Fe^0 reflections, evidencing extensive reduction and carbonization at high temperature. Concomitantly, the amorphous carbon background is reduced, indicating progressing graphitization of the carbon matrix. As observed by N_2 physisorption (Figure 3.4), the specific surface area decreases drastically with increasing temperature, consistent with coalescence and collapse of the original MOF porosity. This is mainly attributed to the collapse of the microporous structure during high-temperature treatment, leading to a significant reduction in surface area.

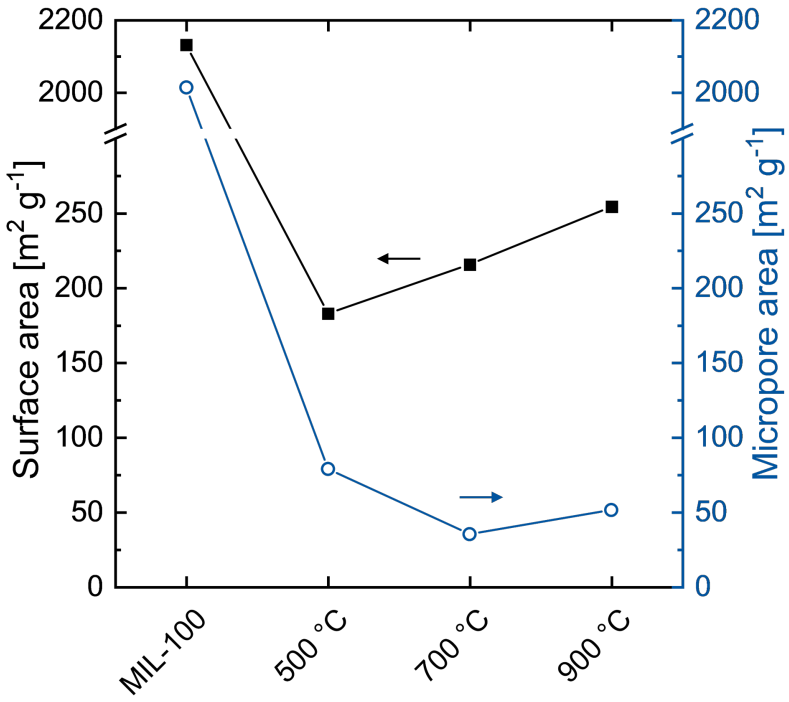

Figure 3.4.: Surface area and pore volume of MIL-100-derived carbons as a function of pyrolysis temperature.

The observed evolution can be summarized as three temperature regimes in Mo Kα XRD. First, an oxide-dominated regime at 300 to 500 °C (broad Fe_3O_4 reflections at 2θ=16 to 28°). Second, a transition regime at intermediate temperatures where the MOF is possibly reduced to iron par-

ticles in a carbon layer [Sant2015; Weze2016]. Unlikely, these particle are not stable after pyrolysis and oxidize immediately upon contact with air. Third, a carbide regime at 800 to 1000 °C was observed with well-defined Fe_3C reflections at 2θ=12.1°, 28.7°, 35.3°, and 41.0° and improved electrical conductivity due to carbide formation and partial graphitization.

The Rietveld analysis and subsequent application of the Scherrer equation yield Fe_3O_4 crystallite sizes in the range of 2 to 22 nm for samples pyrolyzed between 300 °C and 500 °C. In the intermediate temperature range between 600 °C and 700 °C, no stable, evaluable crystalline phases were detected, indicating the presence of largely amorphous or highly dispersed iron species. At higher temperatures, the formation of Fe_3C becomes evident, with crystallite sizes increasing from approximately 44 nm at 800 °C to 55 nm at 1000 °C, while an outlier at 900 °C deviates from this trend. With increasing pyrolysis temperature, Fe-based MOFs undergo framework collapse and transformation into Fe_0 / Fe_xC_y crystallites embedded in a carbon matrix. Higher temperatures enhance atomic diffusion and promote sintering/Ostwald ripening, so smaller Fe-containing crystallites coalesce into larger ones to reduce total surface and grain-boundary energy. Consequently, the average crystallite size typically increases as the pyrolysis temperature rises [Weze2016].

The double-layer capacitance, determined by electrochemical impedance spectroscopy and subsequent equivalent circuit fitting, decreases across the oxide regime from approximately 9 µF to 4 µF. In contrast, the carbide regime exhibits markedly higher capacitances in the range of 400 to 600 µF, again with a local minimum of about 100 µF at 900 °C. The inverse correlation between crystallite size and capacitance suggests that electrical conductivity decreases with increasing crystallite size. The decrease in double-layer capacitance with increasing crystallite size is consistent with a reduction in electrochemically accessible surface and interface area, which diminishes ion adsorption and interfacial charge storage. In composite electrodes, crystallite coarsening may also be accompanied by less favorable contact geometry and higher effective series resistance, further suppressing measured capacitance [Inag2010;

Mací2019].

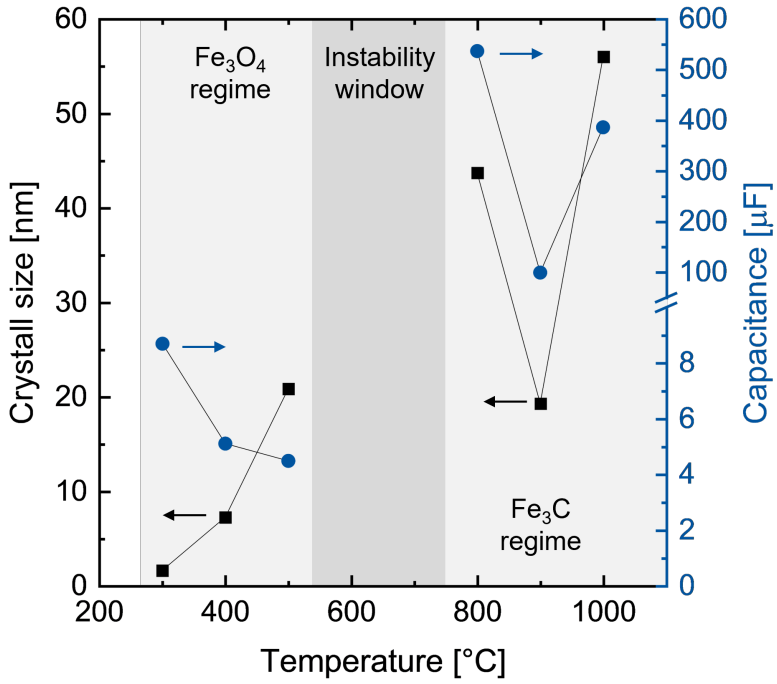

Figure 3.5.: Double-layer capacitance (left axis) and crystallite size from Rietveld refinement (right axis) and vs. pyrolysis temperature; iron oxide and carbide regimes highlighted.

Overall, these trends indicate that the iron oxide phases are significantly less conductive than the iron carbide phases. Furthermore, the decreasing double-layer capacitance with increasing crystallite size points to a decline in interfacial charge-transfer activity. In the following, Raman spectroscopy is employed to evaluate the ordering of the carbon matrix and its influence on electron transport properties.

3.3.3. Morphological Characterization

The morphology of the MIL-100(Fe)-derived carbon materials was investigated by scanning electron microscopy (SEM) and transmission electron microscopy (TEM) to elucidate the spatial distribution and accessibility of the iron-containing particles after pyrolysis (Figure 3.6). In the SEM images, larger particles with diameters ranging from 50 to 100 nm are observed on the external surface of the carbon framework. In contrast, TEM

imaging reveals significantly smaller particles of approximately 5 to 10 nm that appear to be embedded within the carbon matrix. While such encapsulation is beneficial for stabilizing the metallic phase during operation, it may simultaneously impede the accessibility of these particles as catalytic centers during electrolysis[Chen2015; Wu2020].

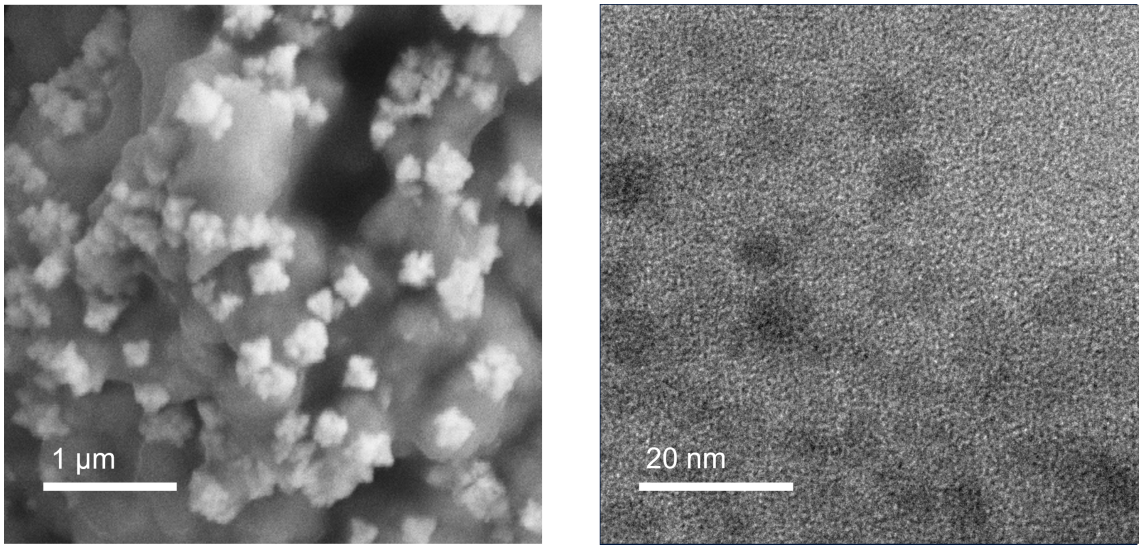

Figure 3.6.: SEM (left) and TEM (right) images of MIL-100 (Fe)-derived carbons at different 1000 °C.

The larger particles are likely composed of iron oxides that segregated during pyrolysis, consistent with the XRD analysis of samples carbonized at lower temperatures. The smaller, homogeneously dispersed nanoparticles within the carbon matrix can be attributed to metallic iron or iron carbide (Fe_3C) domains, depending on the pyrolysis temperature. Their uniform distribution indicates that iron reduction and carburization occurred within the pore network of the MOF-derived carbon. However, these encapsulated nanoparticles are only partially accessible to the electrolyte and may therefore contribute little to the overall electrochemical activity. In contrast, the larger, surface-exposed particles are expected to dominate the electrochemical response. This morphological heterogeneity highlights the complex interplay between particle dispersion, accessibility, and charge-transfer efficiency in the derived catalyst system.

3.3.4. Support Characterization

During pyrolysis of the MIL-100 (Fe), the organic linker decomposes to form a carbonaceous matrix that serves as a conductive support for the embedded iron species. The electrical conductivity of this carbon framework depends strongly on its degree of graphitization. A higher proportion of graphitic carbon facilitates efficient charge transport, whereas amorphous carbon structures exhibit lower conductivity. To evaluate this transformation and its impact on the electronic properties of the support, Raman spectroscopy was employed, as it provides a sensitive probe for the local ordering and defect structure of carbon materials.

All samples exhibit the characteristic D and G bands of carbon at approximately 1350 cm^{-1} and 1580 cm^{-1}, corresponding to disordered sp^2 carbon and the in-plane stretching mode of graphitic carbon, respectively (Figure 3.7)[Ferr2000; Hu2015; Yang2016]. The intensity ratio of these bands (I_D/I_G) serves as an indicator of the structural order and the average size of the graphitic domains in the carbon framework.

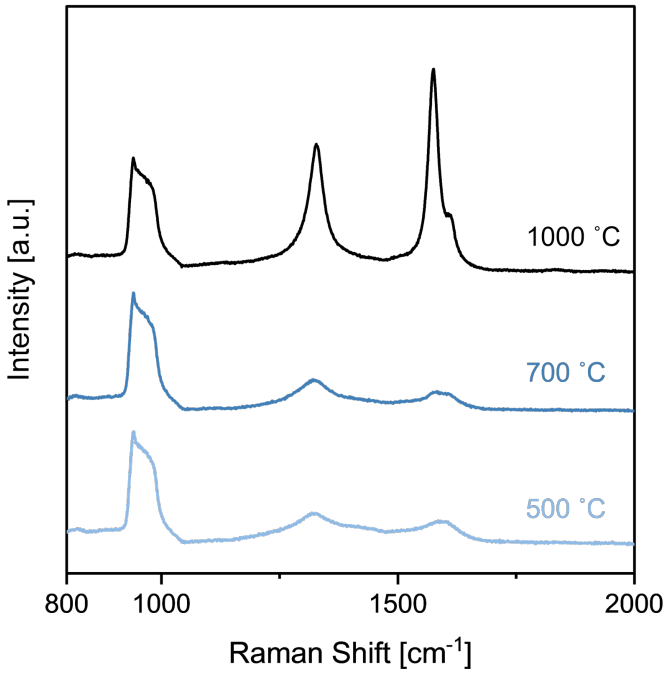

Figure 3.7.: Raman spectra of MIL-100 (Fe)-derived carbons after pyrolysis at different temperatures.

A systematic decrease of the I_D/I_G ratio from 2.0 at 500 °C to 1.7 at 700 °C and 0.9 at 1000 °C indicates a progressive transition from an amorphous to a more ordered, graphitic carbon structure with increasing pyrolysis temperature. This trend confirms the XRD observations of partial graphitization and explains the improved electrical conductivity of the samples carbonized at higher temperatures [Ferr2000; Yang2016].

In summary, Raman spectroscopy confirms that the degree of graphitization and thus the electronic conductivity of the carbon support increases with the pyrolysis temperature. The structural evolution from disordered carbon to graphitic domains defines the conductive network within the catalyst and determines the extent of charge transport to the iron-containing active sites. Consequently, the balance between high conductivity and defect density is a key factor influencing the electrochemical performance of the MIL-100(Fe)-derived catalysts, which will be evaluated in the following section.

3.3.5. Electrochemical Characterization

The electrochemical performance of the MIL-100 (Fe)-derived catalysts was evaluated in alkaline electrolyte to assess their activity for the eNRR. All measurements were performed in 0.1 M KOH electrolyte using a rotating disk electrode (RDE) configuration. Prior to each experiment, the electrolyte was saturated with high-purity nitrogen gas (N_2, 7.0) at a flow rate of 50 mL min^{-1}. To ensure the removal of NO_x-containing impurities, the nitrogen stream was sequentially passed through 0.1 M KOH and 0.1 M $KMnO_4$ scrubbers according to the protocol of Simonov and MacFarlane[Ande2019]. The same cleaning procedure was applied for argon when used as an inert purge gas to obtain baseline measurements.

LSV experiments were conducted in 0.1 M KOH under both N_2- and Ar-saturated conditions to distinguish between background current and potential nitrogen reduction activity. The measurements were performed using the catalyst derived from MIL-100 (Fe) pyrolyzed at 1000 °C. Figure 3.8 shows representative polarization curves for both gas atmospheres. A

slightly higher cathodic current was observed under N_2 compared to Ar saturation, which might indicate weak NRR activity. However, the current difference lies within the experimental error range and could also result from minor changes in gas solubility or bubble coverage at the electrode surface. Thus, no unambiguous catalytic activity can be concluded from these LSV results alone.

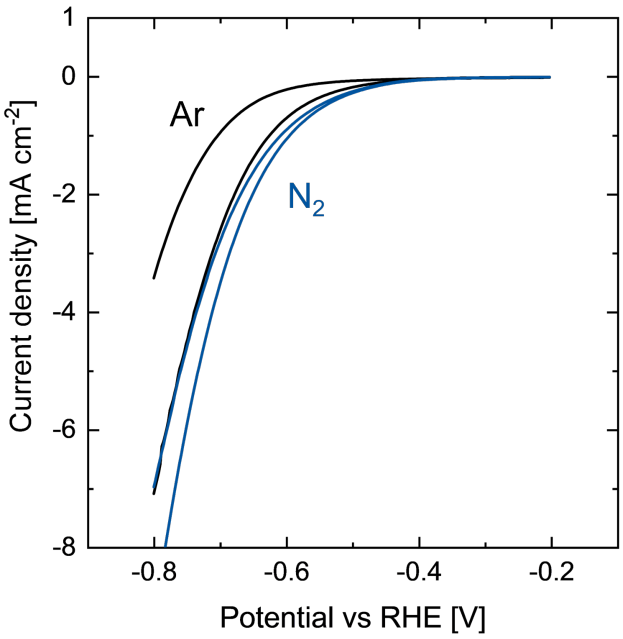

Figure 3.8.: Linear sweep voltammograms of MIL-100(Fe)-derived carbon pyrolyzed at 1000 °C in 0.1 M KOH electrolyte under Ar- (black line) and N_2- (blue line) saturated conditions for two consecutive measurements each.

To further assess the catalytic performance, constant potential electrolysis experiments were performed at –0.1 V versus the reversible hydrogen electrode (RHE) using a gas diffusion electrode (GDE) loaded with 5 mg cm^{-2} of catalyst. The catholyte consisted of 0.1 M KOH, while a 0.5 M H_2SO_4 solution was used as an ammonia trapping medium at the cell outlet. The nitrogen gas (7.0) was purified using the same KOH/$KMnO_4$ washing procedure described above.

The current density strongly depended on the degree of graphitization of the carbon support. The sample pyrolyzed at 300 °C exhibited only neg-

ligible currents due to its low electrical conductivity, whereas the sample prepared at 1000 °C reached current densities in the range of 1.5 mA cm^{-2}. Nevertheless, the current response was strongly fluctuating because of the nitrogen bubbles passing through the gas diffusion layer.

Quantification of ammonia in the acidic trap and the electrolyte revealed only trace amounts below 0.1 nmol cm^{-2} s^{-1} for both catalysts. For the material pyrolyzed at 300 °C, the calculated faradaic efficiency (FE) exceeded 200 %, which is physically implausible and attributed to artefacts such as electrochemical desorption from the membrane or residual contamination, despite rigorous cleaning of the gas supply and cell components. For the 1000 °C sample, the calculated production rates were similarly low, with a maximum FE of approximately 15 %. No detectable ammonia was found in the downstream acid trap. According to the criteria established by Simonov and MacFarlane, these values lie below the *red-light threshold* of 0.1 nmol cm^{-2} s^{-1}, which defines the lower limit for reliable quantification in NRR studies[Choi2020].

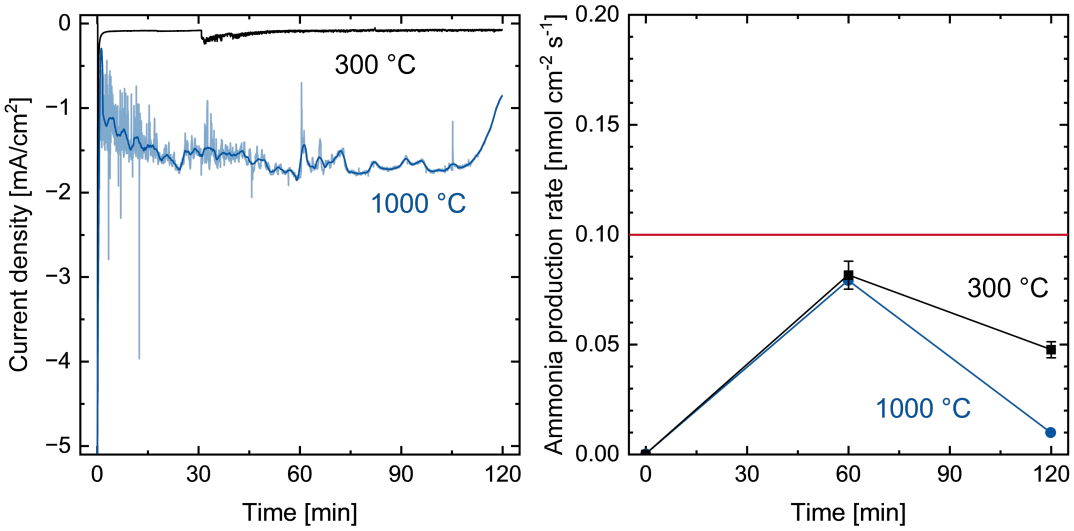

Figure 3.9.: Chronoamperometric response of MIL-100(Fe)-derived carbons at −0.1 V vs. RHE in 0.1 M KOH under purified N_2 feed.

The combined electrochemical results demonstrate that while the electrical conductivity of the materials increases markedly with pyrolysis temperature, the catalytic performance toward nitrogen reduction remains below

the reliable detection limit. The slight current enhancement observed under N_2 atmosphere can be attributed to capacitive contributions or residual surface reactions rather than genuine ammonia formation. These findings emphasize that conductivity and phase composition alone are not sufficient to achieve NRR activity and that a targeted design of accessible, catalytically active iron sites is required. Despite the lack of quantifiable ammonia formation, the experiments confirm that the MIL-100 (Fe)-derived carbon obtained at higher temperatures provides a stable electrode support suitable for further catalyst modification and testing in different reactions.

3.4. Conclusion

The systematic investigation of MIL-100(Fe)-derived carbons demonstrates a clear correlation between pyrolysis temperature, structural evolution, and electrochemical performance. The self-synthesized MIL-100(Fe) precursor exhibited significantly higher crystallinity and surface area than the commercial Basolite® F300, confirming the superior structural integrity of the hydrothermally synthesized MOF. Upon pyrolysis, the framework underwent a sequence of phase transformations: at low temperatures (300 to 500 °C), iron oxides with poor electrical conductivity were formed; in the intermediate regime (500 to 800 °C), the material became unstable and partially reduced; and at high temperatures (900 to 1000 °C), conductive iron carbide and metallic iron phases developed.

Rietveld refinement revealed that the crystallite size of the iron-containing phases increased from only a few nanometers in the oxide regime to approximately 55 nm in the carbide regime. In parallel, the double-layer capacitance rose by two orders of magnitude, confirming a strong dependence of the electronic properties on the pyrolysis temperature. SEM and TEM analyses showed the coexistence of small, encapsulated iron or iron carbide nanoparticles within the carbon matrix and larger, surface-exposed particles. The latter are electrochemically accessible and are therefore assumed to dominate the charge-transfer behavior of the material.

Raman spectroscopy revealed a decreasing I_D/I_G ratio from 2.0 to 0.9 with increasing temperature, indicating progressive graphitization of the carbon support and improved electrical conductivity. However, this graphitic ordering was accompanied by a reduction of defect sites that may contribute to catalytic activity. The overall results highlight that while high-temperature pyrolysis promotes conductivity and structural stability, it simultaneously reduces the number of accessible active centers.

Electrochemical testing confirmed the increased conductivity of the high-temperature materials but did not reveal reliable nitrogen reduction activity. The current differences between Ar- and N_2-saturated electrolytes

were within experimental uncertainty, and the measured ammonia production rates remained below the established detection threshold. These findings underline the need for controlled active-site engineering beyond conductivity enhancement to achieve verifiable NRR activity.

In summary, the MIL-100(Fe)-derived carbon obtained at elevated temperatures provides a robust and conductive electrode support but exhibits no significant intrinsic catalytic activity toward the electrochemical nitrogen reduction reaction. The insights gained from this systematic study establish a fundamental understanding of how the pyrolysis temperature governs phase composition, conductivity, and morphological accessibility, forming the basis for subsequent catalyst optimization and process development also for additional reactions.

4.

Electrochemical Nitrate Reduction in a Batch Cell

4.1. Introduction

The electrochemical nitrate reduction reaction (eNO_3RR) constitutes a promising alternative pathway for sustainable NH_3 production. In contrast to the direct electrochemical nitrogen reduction reaction (eNRR) from gaseous N_2, the use of oxidized nitrogen species such as nitrate (NO_3^-) offers thermodynamic and kinetic advantages, as the N–O bonds can be cleaved at comparatively low overpotentials. Moreover, nitrate is an abundant contaminant in industrial and agricultural wastewater streams and therefore represents both an environmental challenge and a valuable nitrogen source. Its electrochemical conversion to ammonia (NH_3) simultaneously mitigates nitrate pollution and provides a decentralized route for renewable fertilizer production [vLang2021].

In recent years, electrocatalytic eNO_3RR has been investigated on a broad range of transition-metal catalysts, including Cu-, Co-, Ni-, and Fe-based materials, often in nanostructured or foam-like morphologies. These studies have demonstrated that suitably engineered electrodes can reach high faradaic efficiencies (FEs) for NH_3 formation at technologically relevant current densities, even at millimolar nitrate concentrations, while suppressing undesired by-products such as N_2 and NO_2^- [Chen2022b; Fan2022a; Fang2023; Xu2023; Yuan2024]. At the same time, it has become evident that overall performance is not solely governed by the intrinsic catalyst activity but also by mass-transport limitations and local pH gradients, and the transport of counter-ions across the membrane separator. In these cases cell and membrane design play an equally important role as catalyst selection in determining selectivity and energy efficiency [Bae2007; Daiy2021; Pati2021; Wang2020; Wang2023b; Xion2024].

While the previous chapter elaborated the fundamental aspects of eNRR under gas-fed conditions, this chapter focuses on the electrochemical conversion of nitrate to ammonia in a liquid-phase batch configuration as a model system for eNO_3RR. The batch setup allows for the systematic investigation of the key parameters affecting the eNO_3RR, namely electrode material, current density, substrate conversion, as well as membrane type.

In particular, the use of three-dimensional metallic foams provides a well-defined platform to probe how catalyst identity and geometric surface area influence activity and selectivity under controlled mass-transport conditions.

The cell employed in this work consisted of a two-compartment electrochemical reactor separated by an ion-conducting membrane (see Figure 4.2). Nitrate-containing electrolytes were supplied to the catholyte compartment, where the reduction to NH_3 occurred, while oxygen evolution proceeded at the anode. The experiments were performed potentiostatically under ambient pressure and temperature conditions. Different membrane types (cation exchange membrane (CEM), anion exchange membrane (AEM), and bipolar membrane (BPM)) were compared to assess the effect of ion transport and species crossover on the FE and product selectivity. Likewise, metallic foam electrodes composed of copper, cobalt, and nickel were evaluated to determine their catalytic performance and to elucidate trends across different transition metals.

The subsequent sections present a detailed discussion of the experimental findings. Particular emphasis is placed on identifying how the interplay between transport phenomena, reaction kinetics, and membrane selectivity governs the overall nitrogen conversion. In this way, the batch-cell study served as a mechanistic link between catalyst-level phenomena and the process-intensified cell architectures that are developed and analyzed in the following chapter.

4.2. Experimental

This chapter summarizes the experimental methods employed for the electrochemical nitrate reduction experiments conducted in batch mode. First, the experimental setup and operating conditions of the electrochemical cell are described. Subsequently, the cell assembly and electrode materials are outlined, followed by the experimental procedure and the analytical methods used to quantify nitrogen species and hydrogen. Finally, the evaluation of the FE in the batch configuration is detailed.

4.2.1. Materials

Copper, cobalt, and nickel foam cathodes (pore density 50 ppi, thickness 2 mm) were obtained from commercial suppliers and used as received. Nickel foam (4 mm thickness) was employed as anode material. Bipolar membranes (fumasep® FBM) as well as cation and anion exchange membranes (fumapem® F-14100 and fumasep® FAB-PK-130, respectively) were supplied by Fumatech and were pre-treated according to the manufacturer's recommendations prior to use.

Potassium hydroxide (KOH, $\geq$85 %) and sulfuric acid (H_2SO_4, 5 M) were purchased from Sigma-Aldrich®. Potassium nitrate (KNO_3, $\geq$99 %) was obtained from Fisher Scientific®. Sodium sulfate (Na_2SO_4, $\geq$99 %) and tripotassium phosphate ($K_3PO_4 \cdot {}_3H_2O$, $\geq$99 %) were purchased from Carl Roth®. All electrolytes were prepared with deionized water (resistivity $\geq$18.2 MΩ cm).

4.2.2. Electrochemical Cell

The electrochemical cell consisted of a flow cell (Flex-E-cell, FXC Engineering) with a geometric electrode area of 25 cm^2. The assembly is illustrated in Figure 4.1. On the cathode side, a titanium flow field with a 1.5 mm deep recess defined the active area and acted as the current collector. A Santoprene gasket sealed the interface between housing and flow field. The bipolar membrane (fumasep® FBM or other ion exchange membranes as

specified) was placed centrally between two PTFE sealing frames with a 25 cm^2 window. On the anode side, a nickel foam electrode (4 mm thickness) was mounted with a second Santoprene gasket and a titanium current collector plate.

The cell was compressed with four bolts to a defined torque of 7 N m to ensure leak-tight operation and good electrical contact. Electrolyte flow through both compartments was directed from bottom to top to support efficient gas removal from the electrode surfaces.

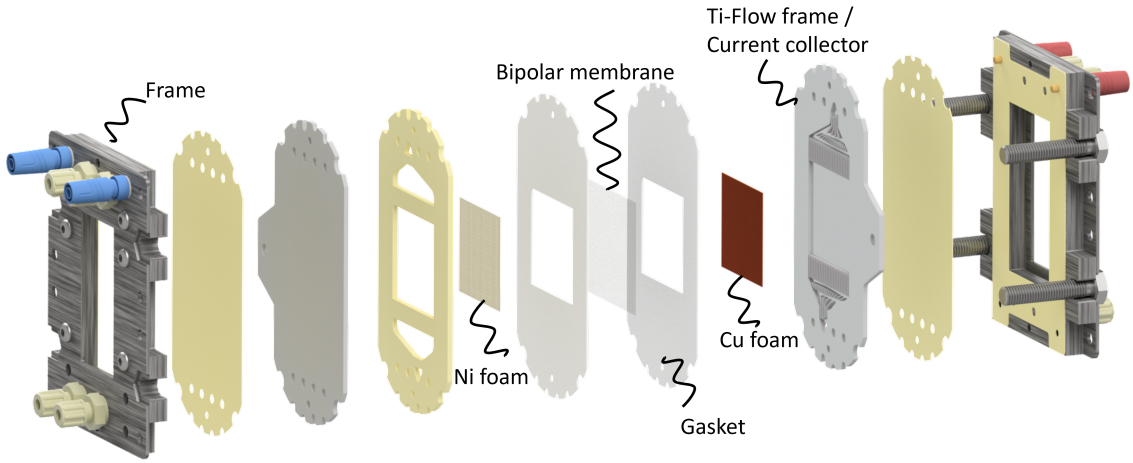

Figure 4.1.: Construction of the electrochemical cell (FXC GmbH) with anode on the left side and cathode on the right side. The bipolar membrane is placed centrally between the two flow fields.

4.2.3. Experimental Setup

All experiments in this chapter were carried out in a divided electrochemical cell operated in batch mode. The experimental setup is schematically depicted in Figure 4.2. The anolyte and catholyte were stored in Schott flasks and were continuously circulated through the respective cell compartments by piston pumps (Ismatec MCP series) at a flow rate of 100 mL min^{-1}, unless stated otherwise. The circulation ensured a well-mixed reactor volume on both sides.

The anolyte volume was 150 mL, and the catholyte volume 75 mL. Both

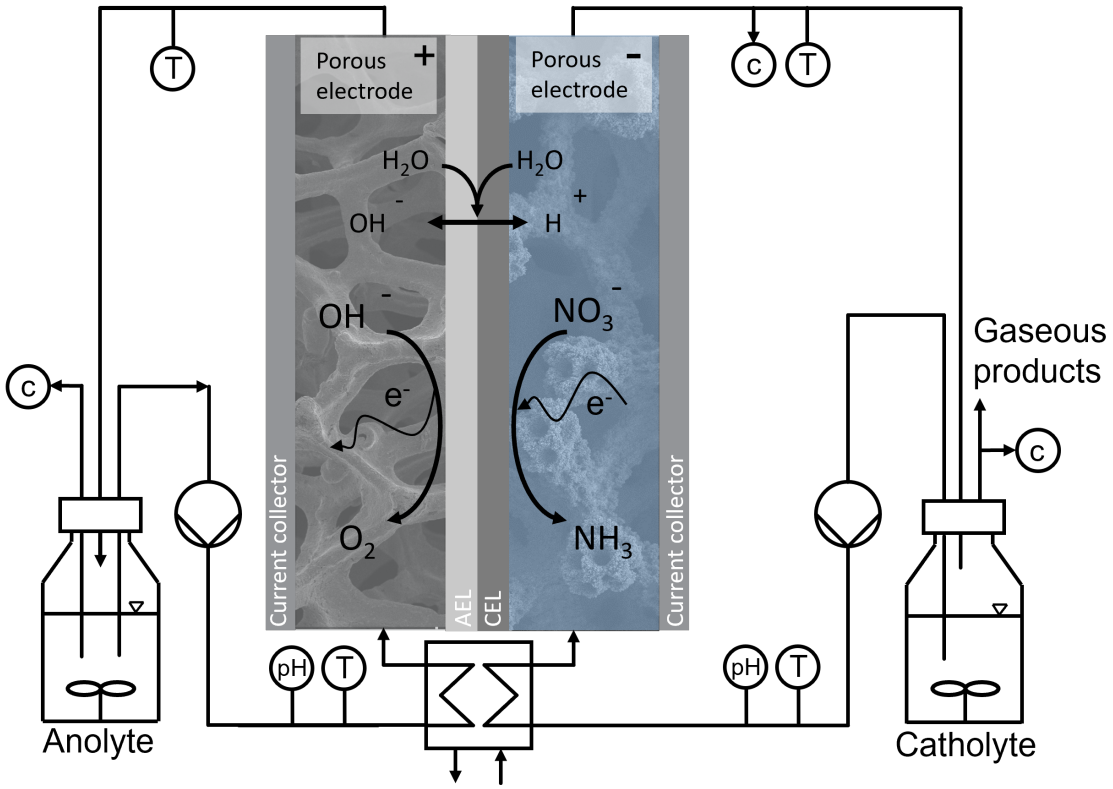

Figure 4.2.: Flow diagram of the experimental setup with electrochemical cell, anolyte and catholyte reservoirs, circulation pumps, heat exchanger, and analytical peripherals.

compartments operated as closed batch reactors. The electrolyte temperature was controlled via an external heat exchanger connected to a Julabo 900F cryostat and maintained at 20 °C. The pH of anolyte and catholyte was monitored inline with pH electrodes (Knick SE 555). All controllers and sensors were adjusted and data were recorded using an echem-workstation (ZUMOLab GmbH) and visualized in real time.

The gas space above the catholyte overflow vessel was continuously purged with N_2 at 50 mL min^{-1} to remove evolved gases and maintain an inert atmosphere. The outlet gas stream was intermittently analyzed by gas chromatography (GC) and the volumetric gas flow was determined with a soap-film flow meter for hydrogen quantification. All experiments were conducted at ambient pressure.

The cell was operated galvanostatically with a potentiostat (BioLogic SP-150e + VMP3B-20A booster). Cell voltage and current were recorded continuously. A reversible hydrogen electrode (RHE, Gaskatel HydroFlex)

placed in the catholyte reservoir was used to measure the cathode potential in a three-electrode configuration when required.

4.2.4. Electrode Materials

Metallic foam electrodes of copper, cobalt, and nickel were employed as cathodes for the nitrate reduction experiments. All foams had a nominal pore density of 50 ppi and a thickness of 2 mm. Rectangular pieces with a geometric area of 25 cm^2 were cut from the supplied foams and rinsed with ethanol and deionized water. Prior to installation, the electrodes were ultrasonically cleaned for 10 min in deionized water and dried in air.

Unless stated otherwise, no additional surface modification (e.g. electrodeposition or thermal oxidation) was performed for this chapter. Copper foam was used as the standard cathode material for parameter studies after the screening experiments, as it provided the highest FE and is economically favorable.

The anode consisted of nickel foam with a thickness of 2 mm and a geometric area matched to the cathode. The anolyte was typically 0.1 M KOH. The catholyte consisted of 0.1 M KOH containing KNO_3 at concentrations of 2000 mg L^{-1}, depending on the experiment.

4.2.5. Gas Analysis

The gas phase was analyzed with an Agilent 8890 GC system. Helium was used as the carrier gas. For H_2, O_2, and N_2 quantification, 100 µL of sample gas were injected and separated on a HaysepQQ, MS5A, and HaysepQ column sequence. Typical analysis time was 21 min per sample. The volumetric gas flow was determined with a soap-film flow meter, and the molar H_2 production rate was obtained from the product of the flow rate and the GC-determined hydrogen volume fraction. Ammonia in the gas phase was measured with a PoraPLOT Amines Column, but was not detected within the measurement accuracy in this work; ammonia was therefore evaluated via the liquid-phase ammonium concentration.

4.2.6. Ion Chromatography

Liquid samples were analyzed by ion chromatography for nitrate, nitrite, and ammonium. Anions were quantified using a 930 Compact IC Flex system with a Metrosep A Supp 7-250/4.0 column at 45 °C. The eluent was 3.6 mM Na_2CO_3 at a flow rate of 0.7 mL min^{-1}. Nitrite and nitrate showed characteristic retention times that were used for peak identification and quantification via calibration curves.

Cations were analyzed on a second 930 Compact IC Flex system equipped with a Metrosep C 6-250/4.0 column at 30 °C. The eluent consisted of 1.7 mM HNO_3 and 1.7 mM pyridine-2,6-dicarboxylic acid at a flow rate of 0.9 mL min^{-1}. All concentrations were calculated from calibration curves obtained with standard solutions.

To ensure that nitrite and ammonium were measured in their ionic forms, samples were diluted with deionized water and neutralized to approximately pH 7 using either diluted H_2SO_4 or K_3PO_4 solution prior to analysis, as the IC eluents were acidic.

4.2.7. Performance Parameters

FE was used as the main figure of merit to evaluate the selectivity of charge utilization for nitrate reduction to ammonia. The definition follows the general Faraday law:

$$FE = \frac{Q_{\text{product}}}{Q_{\text{total}}} = \frac{z\, n_{\text{product}}\, F}{Q_{\text{total}}} \tag{4.1}$$

For the nitrate reduction to ammonia, $NO_3^- \rightarrow NH_3$, eight electrons per mole of nitrogen are required ($z = 8$). The amount of ammonia formed in the catholyte at time t was calculated from the measured ammonium concentration $c_{NH_4^+}(t)$ assuming a well-mixed batch reactor:

$$n_{NH_3}(t) = c_{NH_4^+}(t)\, V_{\text{cath}} \tag{4.2}$$

The total charge passed was obtained from the applied constant current I and the electrolysis time t:

$$Q_{\text{total}}(t) = I\,t \tag{4.3}$$

The instantaneous FE towards ammonia at a given sampling time t was then evaluated as:

$$FE_{\text{NH}_3}(t) = \frac{z\,c_{\text{NH}_4^+}(t)\,V_{\text{cath}}\,F}{I\,t} \tag{4.4}$$

For comparison with the theoretical full conversion, the time t_{FE} at which sufficient charge for the complete reduction of all initially present nitrate is supplied was calculated as:

$$t_{\text{FE}} = \frac{c_{\text{NO}_3^-,0}\,V_{\text{cath}}\,z\,F}{I} \tag{4.5}$$

Apart from the FE, the nitrate conversion X, selectivity S, and yield Y were evaluated as additional performance indicators. Their definitions are as follows:

$$X_i = \frac{n_{i,0} - n_i}{n_{i,0}} \tag{4.6a}$$

$$S_j = \frac{n_j - n_{j,0}}{n_{i,0} - n_i} \cdot \frac{|\nu_i|}{|\nu_j|} \tag{4.6b}$$

$$Y_j = X_i \cdot S_j = \frac{|\nu_i|}{|\nu_j|} \cdot \frac{n_j - n_{j,0}}{n_{i,0}} \tag{4.6c}$$

4.3. Results and Discussion

The electrochemical reduction of nitrate to ammonia was successfully demonstrated in the batch cell configuration introduced above. The following section presents the systematic evaluation of process parameters with respect to their influence on FE, selectivity, and overall nitrogen conversion. Particular attention is paid to the role of ion transport through the membrane, the catalytic properties of the electrode material, and the hydrodynamic conditions inside the electrochemical cell.

4.3.1. Membrane Influence

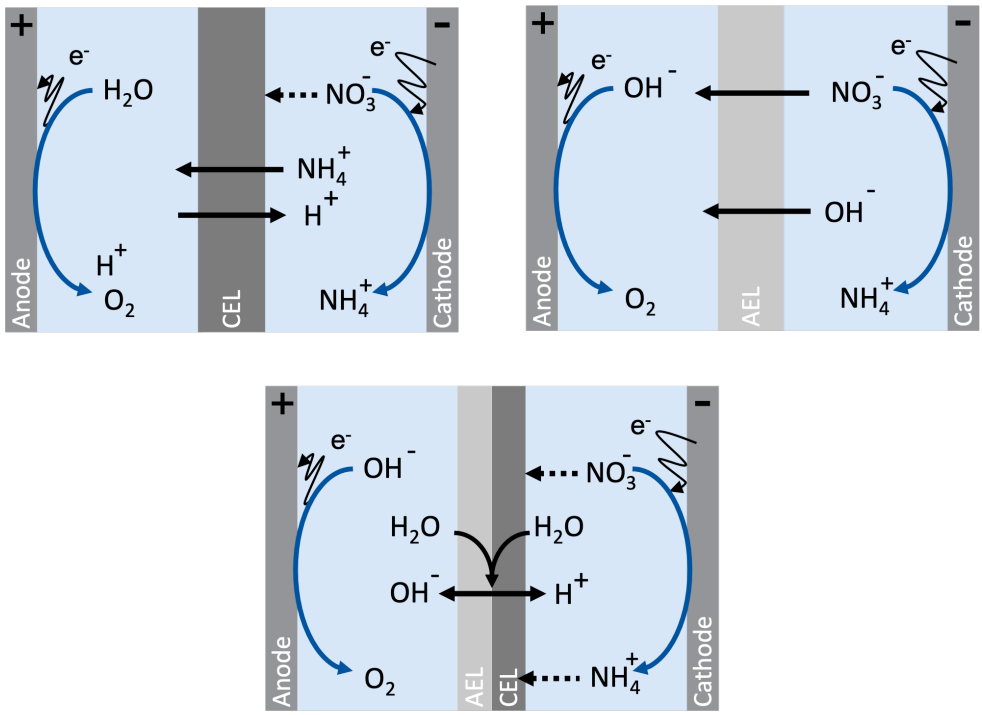

Figure 4.3.: Schematic depiction of ion migration and crossover phenomena for CEM, AEM, and BPM membranes during eNO_3RR.

The ion exchange membrane in an electrochemical cell governs the transport of charged species between the catholyte and the anolyte and thereby ensures charge neutrality during operation. Its selectivity determines whether anions, cations, or both can migrate in response to the ap-

plied electric field. In the context of the eNO_3RR, this ion transport strongly influences the distribution of nitrogen species, as both the substrate (NO_3^-) and the desired product (NH_4^+) are ionic. Without a separating membrane or porous separator, the reduced nitrogen species formed at the cathode, such as NO_2^-, NH_2OH, or NH_3/NH_4^+, would diffuse to the anode compartment, where they would be readily re-oxidized to nitrate or gaseous nitrogen oxides. This parasitic back-oxidation would lead to an apparent loss of product and severe underestimation of the FE [Wild2024; Pirr2024].

Consequently, the membrane not only serves as an ionic conductor but also as a physical and electrochemical barrier separating reduction and oxidation environments. However, the membrane's selective permeability simultaneously defines the extent of reactant and product crossover. Migration and diffusion of nitrate or ammonium species across the membrane can therefore directly alter the overall nitrogen balance and the apparent FE towards NH_3. The interplay between ion conduction and species confinement renders the choice of membrane a decisive parameter for the performance and selectivity of the eNO_3RR. To elucidate the influence of the membrane type on the eNO_3RR, three different ion exchange membranes were evaluated: a CEM (fumapem® F-14100), an AEM (fumasep® FAB-PK-130), and a BPM (fumasep® FBM).

When a CEM is employed, it is essential to consider that many commercial cation-exchange materials are proton-exchange-type polymers (often referred to as proton exchange membranes, PEMs) and are therefore optimized for high H^+ conductivity. Although such membranes preferentially transport protons, they are not perfectly selective under realistic operating conditions. Larger hydrated cations, including NH_4^+, can permeate the membrane to a limited extent *via* electro-migration, facilitated co-ion transport, or by diffusive flux through structural imperfections or transient swelling of the polymer matrix, particularly at elevated ionic strength, high current density, or extended operation [Wild2024]. In addition, neutral NH_3 can diffuse across the membrane due to its small kinetic diameter and significant solubility in hydrated polymer phases, causing further ammonia crossover to the anolyte [Sign2024; Wild2024]. Consequently,

non-negligible transport of ammonium species can occur. In this work, the resulting NH_4^+ accumulation in the anolyte (Figure 4.4) evidences this crossover. Once transferred, ammonium may undergo anodic oxidation or be stripped from the anolyte, both of which deplete the nitrogen-containing product and lower the apparent FE determined solely from catholyte analysis.

The AEM exhibits the opposite selectivity, enabling the transport of anions such as OH^- but also NO_3^- from the catholyte to the anolyte. In this configuration, NO_3^- are continuously removed from the catholyte by migration and diffusion, leading to a lower reactant concentration near the cathode and thus a loss of valuable educt, which can be seen by the rising NO_3^- concentration in the anolyte (Figure 4.4). Besides the fact that nitrate migration through anion-selective membranes leads to incomplete reduction and poor nitrogen utilization, the resulting imbalance also affects the local pH. The depletion of NO_3^- and concurrent transfer of OH^- alter the catholyte alkalinity, shifting the equilibrium between NH_3 and NH_4^+ and also influence the balance between hydrogen evolution reaction (HER) and eNO_3RR. Overall, the use of an AEM in the batch configuration results in substrate crossover, pH instability, and a reduction in eNO_3RR selectivity. While it maintains sufficient ionic conductivity to close the circuit, its anion-selective nature inherently promotes the loss of nitrate reactant and deteriorates the electrochemical environment for selective ammonia formation.

In contrast to single-ion exchange membranes, a BPM consists of a cationic and an anionic layer joined at an internal interface where water dissociation occurs [Pärn2021]. When operated in inside-out mode, the water splitting generates H^+ and OH^- ions that migrate toward the cathode and anode, respectively. This self-generated ionic flux maintains charge neutrality while simultaneously suppressing the migration of other ions such as NO_3^- and NH_4^+ across the membrane. Consequently, both the substrate and the product remain confined to the catholyte, drastically reducing cross-over losses. In the present study, the BPM configuration achieved the lowest cross-over of either NO_3^- or NH_4^+ yielding the high-

est FE, demonstrating that BPM can effectively retain ionic species within the catholyte during eNO_3RR operation.

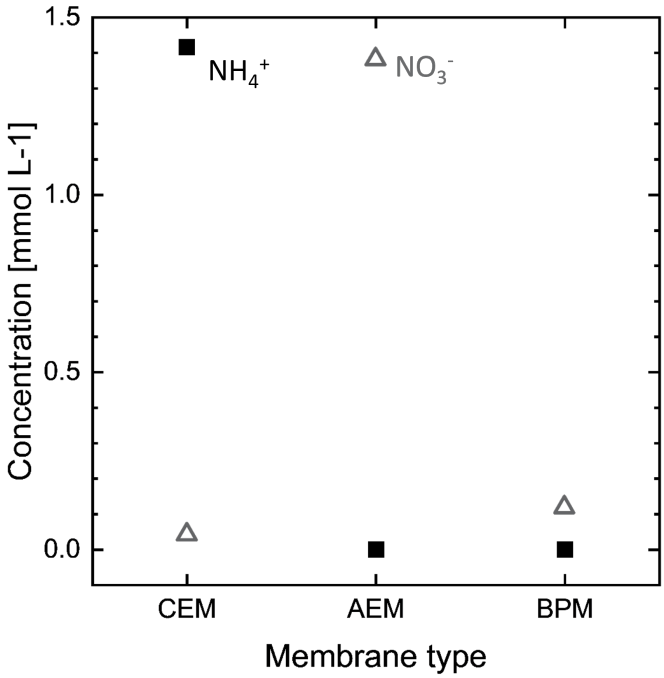

Figure 4.4.: Concentration of NH_4^+ (■) and NO_3^- (△) in the anolyte that originate from crossover for different types of membranes.

In summary, the membrane type governs the nitrogen distribution across the cell and thereby the apparent selectivity of the process. While CEM and AEM promote undesired cross-over of either product or substrate, the BPM successfully confines both within the catholyte, yielding the highest FE and operational stability. Hence, the results emphasize that ion transport phenomena must be considered and in further experiments the BPM configuration is employed to minimize crossover effects.

4.3.2. Electrode Material Screening

The cathode material plays a decisive role in governing both the activity and selectivity of the eNO_3RR, as it defines the adsorption strength of reaction intermediates and the competition with the HER. To systematically evaluate this influence, metallic foam electrodes composed of Cu, Co, and

Ni were tested under identical electrochemical conditions in the batch configuration.

Cu and Co foams exhibited superior activity for nitrate reduction, achieving FEs of approximately 48 % and 46 %, respectively, while Ni reached only about 5 % (Figure 4.5). The markedly lower performance of Ni was accompanied by a significantly increased hydrogen evolution rate, as observed by a higher gas-to-electrolyte ratio in the outlet stream. These results indicate that the HER dominates on Ni as also mentioned in literature [Wang2024]. In contrast, Cu and Co promote selective reduction of nitrate to ammonia.

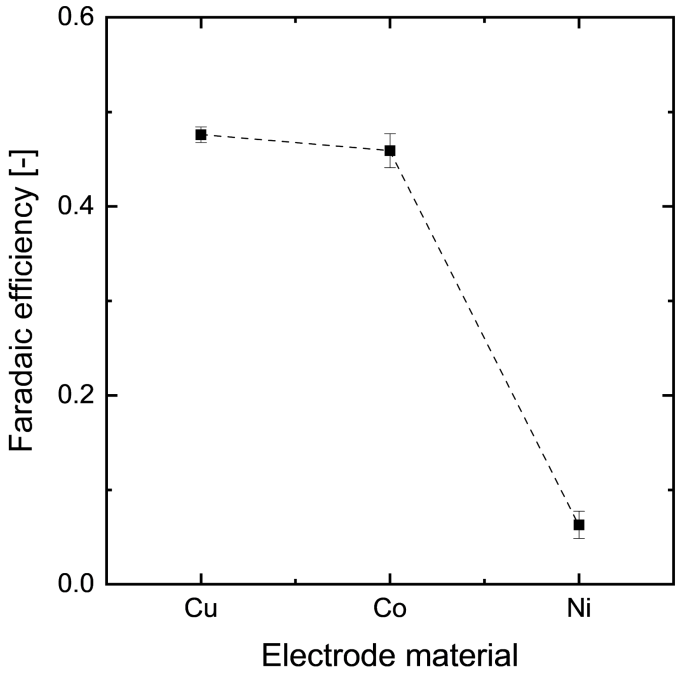

Figure 4.5.: Comparison of faradaic efficiencies for nitrate reduction to ammonia on Cu, Co, and Ni foam electrodes under identical electrochemical conditions; current density 100 mA cm^{-2}; catholyte: 0.1 M KOH, 2000 mg L^{-1} NO_3^- from KNO_3; bipolar membrane: fumasep FBM-PK-130.

The enhanced eNO_3RR activity on Cu and Co can be rationalized by their intermediate nitrogen-metal and hydrogen-metal binding energies, which provide a favorable balance between activation of the nitrate species and suppression of excessive hydrogen adsorption. On these surfaces, nitrate reduction is thought to proceed via stepwise proton-electron transfer reac-

tions involving NO_2^-, NH_2OH, and $\cdot NH_2$ intermediates before the formation of NH_3. Both Cu and Co are capable of stabilizing these intermediates sufficiently to enable complete reduction without excessive desorption or side reactions.[Hu2015; Garc2018]

This mechanistic interpretation aligns with recent computational and experimental studies. Karamad *et al.* [Kara2023; Yang2024] demonstrate that moderate nitrogen adsorption and hydroxide binding are key descriptors for selective nitrate-to-ammonia conversion. Metals with overly strong hydrogen affinity, such as Ni, favor the HER pathway due to the near thermoneutral binding energy of adsorbed hydrogen, whereas Cu and Co fall into a range that supports the adsorption and subsequent protonation of nitrogen intermediates.

Overall, the comparative screening highlights Cu and Co foams as the most suitable cathode materials for eNO_3RR in the batch configuration. Their electronic properties promote nitrate activation while mitigating parasitic hydrogen evolution. As Cu is more abundant and cost-effective, it was selected for further process optimization in subsequent experiments.

4.3.3. Influence of Nitrate Concentration

The availability of nitrate at the electrode-electrolyte interface is a key determinant for the selectivity of the eNO_3RR. In the batch configuration, both the bulk nitrate concentration and the applied current density define how rapidly nitrate can be replenished at the catalytic surface. Insufficient transport of NO_3^- leads to local depletion, which in turn promotes the competing HER.

The influence of substrate concentration was investigated at initial nitrate levels of 2000 mg L^{-1}, 1000 mg L^{-1}, and 500 mg L^{-1}. At 2000 mg L^{-1}, the eNO_3RR exhibited a Faraday efficiency (FE) of approximately 48 % (Figure 4.6). Reducing the nitrate concentration to 1000 mg L^{-1} decreased the FE to about 20 %, and at 500 mg L^{-1} the FE further declined to roughly 16 %. This systematic loss in selectivity reflects the increasingly limited diffusive supply of nitrate according to Fick's law to the electrode surface

as the bulk concentration decreases. When nitrate cannot be delivered at a rate sufficient to sustain the imposed current, the electrode potential shifts to more negative values and HER becomes the dominant cathodic pathway.

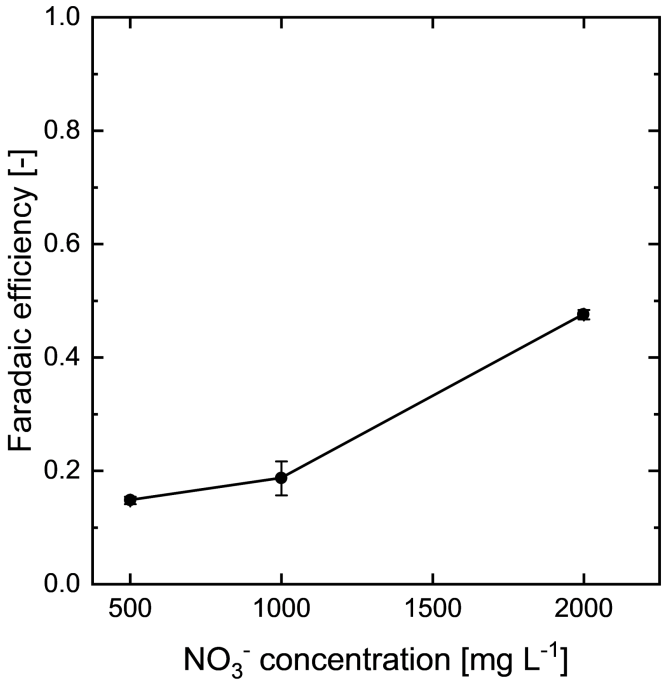

Figure 4.6.: Faradaic efficiency for nitrate reduction to ammonia for varying NO_3^- concentrations; cathode: copper foam; current density 100 mA cm^{-2}; supporting catholyte: 0.1 M KOH; bipolar membrane: fumasep FBM-PK-130.

The reduced surface availability of nitrogen-containing intermediates under low-concentration conditions further amplifies this effect. As the NO_3^- flux diminishes, the coverage of reactive intermediates such as NO_2^- and NH_2OH becomes too low to compete effectively with proton reduction, leading to a higher fraction of the current being diverted toward H_2 formation. This behavior is fully consistent with the drop in FE and working electrode potential observed during the nitrate conversion (Figure 4.7). The vertical dashed line in Figure 4.7 indicates the theoretical full conversion based on one faradaic equivalent, beyond which nitrate conversion reduces and HER starts, which can be seen in the potential drop and also the evolution of hydrogen could be observed.

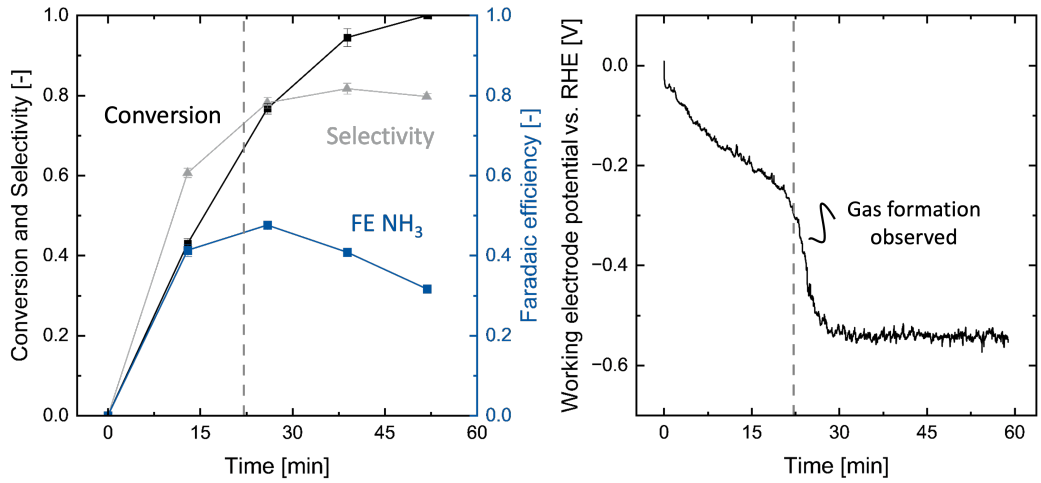

Figure 4.7.: Conversion, selectivity and faradaic efficiency for nitrate reduction to ammonia during batch electrolysis over time (left) and working electrode potential over time (right); cathode: copper foam; current density 100 mA cm^{-2}; supporting catholyte: 0.1 M KOH; bipolar membrane: fumasep FBM-PK-130. Vertical dashed line indicates theoretical full conversion time based on one faradaic equivalent.

In summary, decreasing nitrate concentration reduce the effective supply of nitrate to the electrode, thereby shifting the reaction competition toward hydrogen evolution. These finding indicates the mass-transport-controlled nature of the eNO_3RR in batch operation and underscore the importance of balancing substrate availability with applied current to maintain high ammonia selectivity.

4.3.4. Effect of Hydrodynamics and Spacer Geometry

The hydrodynamic environment in the catholyte compartment was modified by introducing a polymeric spacer between the membrane and the cathode. This configuration increases the interelectrode gap, reduces the local Reynolds number, and thereby alters the balance between convective transport and diffusive replenishment of reactants and intermediates. In contrast to the zero-gap setup, where strong forced convection continuously sweeps species away from the electrode surface, the spacer establishes a more diffusion-dominated regime.

The introduction of the spacer resulted in a measurable increase in the

FE towards NH_3. This improvement can be attributed to the reduced convective removal of reactive intermediates such as NO_2^- and NH_2OH, which require sufficient residence time at the electrode to undergo further proton-electron transfer steps. Under zero-gap conditions, these intermediates are more readily transported away from the catalytic surface before full reduction can occur, lowering the overall selectivity. In the spacer configuration, the moderated hydrodynamics promote their retention within the reaction zone, allowing more complete conversion to NH_3.

The experimental trends support this mechanistic interpretation. In the zero-gap cell, higher concentrations of nitrite were detected in the catholyte, indicating incomplete reduction and faster removal of intermediates. When the spacer was applied, significantly lower nitrite concentrations were observed throughout the experiment, and toward the end no detectable nitrite remained. This disappearance suggests that the intermediates formed during eNO_3RR were successfully converted further to NH_3 rather than being lost to transport effects. The corresponding data are provided in the appendix for reference.

Besides altered mass transport, changes in the local pH environment may also contribute to the improved performance. The reduced convective mixing within the spacer region can stabilize localized alkalinity near the cathode surface, which is known to facilitate the protonation and reduction of NO_x^- intermediates [Pére2017].

During batch experiments, steady-state conditions could not be not reached. Hence, the adsorption and desorption of ionic species, particularly NH_4^+ within the membrane phase, led to transient variations in product concentration and apparent FE. These effects complicate the quantitative evaluation of the batch data and highlight the necessity of continuous operation. The subsequent chapter therefore transitions to a feed-and-bleed configuration to decouple transport and adsorption effects and to establish stable reaction conditions.

4.4. Conclusion

In this chapter, the electrochemical reduction of nitrate to ammonia was demonstrated in a two-compartment batch cell and systematically analyzed with respect to membrane type, electrode material, nitrate concentration, and hydrodynamic conditions. The study highlights that all of these parameters are strongly interlinked through ion transport, mass transfer, and reaction selectivity.

The membrane screening revealed that the ion exchange membrane critically governs the nitrogen distribution between catholyte and anolyte. The CEM allowed significant crossover of NH_4^+ and NH_3 toward the anolyte, where back-oxidation and stripping processes led to an apparent loss of product and reduced FE. The AEM, in contrast, promoted migration of the substrate NO_3^- to the anolyte, decreasing the reactant availability in the catholyte and inducing pH imbalances that favored the HER over the eNO_3RR. Only the BPM operated in inside-out mode effectively confined both nitrate and ammonium species to the catholyte, thereby minimizing crossover and enabling the highest FEs. For all subsequent experiments, the BPM configuration was therefore selected as the reference setup.

The electrode material screening demonstrated that Cu and Co foams are significantly more selective towards ammonia formation than Ni foam. Under identical conditions, Cu and Co achieved FEs of approximately 48 % and 46 %, respectively, whereas Ni reached only about 5 %. The poor performance of Ni was accompanied by pronounced hydrogen evolution, indicating that the HER is thermodynamically favored over nitrate activation. Cu, being both highly selective and economically attractive, was chosen as the cathode material for further investigations.

Variation of the nitrate concentration showed that decreasing the initial NO_3^- level from 2000 mg L^{-1} to 1000 mg L^{-1} and 500 mg L^{-1} caused a strong decline in FE from about 48 % to 20 % and 16 %, respectively. This trend was attributed to mass-transport limitations at low substrate concentration, which reduce nitrate availability at the electrode surface and shift the reaction competition towards hydrogen evolution. A similar loss in se-

lectivity was observed at elevated current densities, where the imposed electron flux exceeded the rate at which nitrate could be supplied, again driving the system into a regime dominated by HER. These observations underline the mass-transport-controlled nature of the eNO_3RR in batch operation.

Finally, the hydrodynamic conditions were tuned by inserting a polymeric spacer between membrane and electrode. The spacer increased the inter-electrode gap and reduced convective mixing, which led to higher FEs towards NH_3 and markedly lower concentrations of nitrite intermediates. Toward the end of the experiments with the spacer, no nitrite was detected, indicating more complete conversion of intermediates to ammonia. Besides the modified mass transport, localized pH effects likely contributed to the improved performance, although they cannot be fully decoupled in the present configuration.

Overall, the batch experiments identified a bipolar membrane in inside-out operation, copper foam cathodes, sufficiently high nitrate concentration, and moderate hydrodynamics as key design elements for selective nitrate reduction to ammonia. At the same time, the non-steady-state behavior and transient adsorption phenomena observed in the batch cell limit the quantitative assessment of long-term performance. These findings motivate the transition to a continuous feed-and-bleed operation, which is examined in the subsequent chapter to achieve stable reaction conditions and improved nitrogen utilization.

5.

Electrochemical Nitrate Reduction in a Continuous Feed-and-Bleed Reactor

Parts of this chapter are published:
Yannick Sebastian Mürtz, Franz Röllgen, Ulrich Simon, Matthias Wessling, Robert Keller
Engineering mass transport for scalable acidic nitrate-to-ammonia electrolysis in a continuous flow reactor

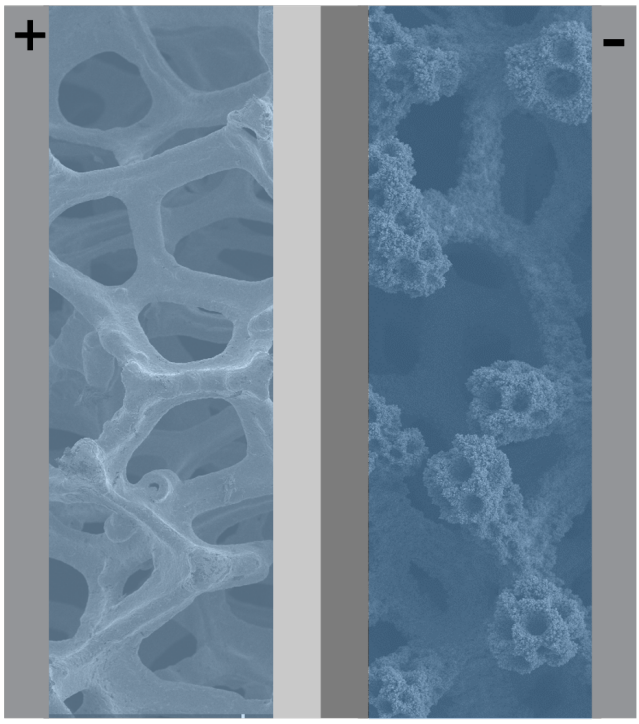

5.1. Introduction

The overarching objective of this dissertation is to develop a mechanistic and engineering-based understanding of electrochemical pathways for sustainable ammonia (NH_3) production from reactive nitrogen species, with a particular focus on nitrate-containing waste streams and their integration into decentralized nitrogen management concepts. Previous chapters have introduced the thermodynamic and kinetic fundamentals of electrochemical nitrogen conversion, including the electrochemical nitrogen reduction reaction (eNRR) and the electrochemical nitrate reduction reaction (eNO_3RR), and have discussed the design and performance of heterogeneous electrocatalysts, for example based on Metal-Organic-Frameworks (MOFs) and their derivatives, for NH_3 formation. These catalyst-centered investigations have highlighted that, beyond intrinsic activity and selectivity, macroscopic cell design, mass transport, and reactor operation strongly influence the overall process efficiency[Paid2002].

Building on this foundation, the present chapter shifts the focus from catalyst discovery to electrochemical reactor and process design for eNO_3RR.

The central question addressed here is how electrolyte composition, hydrodynamics, and operating conditions in a continuous flow cell determine the achievable current densities, Faradaic efficiencies, and energy efficiency for nitrate-to-ammonia conversion. In particular, we aim to disentangle intrinsic catalytic effects from mass-transport-induced limitations and to derive design principles for scalable, decentralized nitrate valorization.

Nitrate contamination, primarily originating from agricultural runoff and industrial effluents, poses serious ecological and human health risks[Guti2018]. Conventional remediation strategies often generate concentrated waste streams that require costly disposal[Barr2023; Guid2022; Huan2024b]. The eNO_3RR to ammonia (NH_3) offers a promising alternative by converting nitrate into a valuable industrial feedstock, thereby mitigating waste accumulation and advancing a circular nitrogen economy[Plet1979; MacF2020; Liu2022; Zhan2024a]. In the broader context of this dissertation, eNO_3RR thus represents a complementary route to eNRR for accessing sustainable ammonia while simultaneously addressing nitrogen pollution.

Beyond waste valorization, the electrochemical synthesis of ammonia provides a sustainable alternative to the energy-intensive Haber-Bosch process, which currently depends on hydrogen derived from fossil fuels. The electrochemical route eliminates the need for external hydrogen production, envisioning ammonia synthesis under ambient conditions powered by renewable electricity. This approach supports decentralized ammonia production, reducing energy consumption and associated carbon emissions[Xu2023; Chen2024a; Yuan2024; Guo2024]. From a systems' perspective, as developed in the introductory chapters of this dissertation, such decentralized schemes become particularly attractive when they can be coupled to local waste streams, thus shortening nitrogen and energy supply chains [McEn2020].

The electrochemical conversion of nitrate to ammonia offers an opportunity to close the anthropogenic nitrogen cycle and restore the balance of reactive nitrogen. The electrochemical reduction of NO_3^- to ammonia

is inherently favorable, in contrast to denitrification pathways yielding N_2, which require subsequent cleavage of the strong triple bond in N≡N, as in the classical Haber-Bosch process or the eNRR[Choi2020]. In addition, diverse wastewater streams, such as agricultural runoff, industrial effluents, and even low-level nuclear waste, can serve as nitrate sources for ammonia production[vLang2021]. However, the typically low and fluctuating nitrate concentrations in these streams, together with variations in wastewater composition, can impact process performance and therefore require tailored reactor design strategies. One of the overarching themes of this dissertation is that successful implementation of eNO_3RR technologies must therefore couple catalyst design to robust reactor concepts capable of dealing with variable feed compositions.

Multiple reviews have emphasized the chemical and morphological modification of copper surfaces to enhance catalytic efficiency[Bae2007; Chen2022a; Daiy2021; Pati2021; Ren2021; Wang2020; Wang2023b; Xion2024]. High faradaic efficiency (FE) values of around 95 % have been achieved, for instance, by tailoring the surface morphology through nanostructuring, such as creating porous Cu electrodes or Cu coatings[Fang2023], or by chemically doping Cu with Ru to introduce new active sites[Liu2022]. Recent studies have demonstrated remarkable activity even at low nitrate concentrations (2000 mg L^{-1}), reaching industrially relevant current densities above 1000 mA cm^{-2} with Faradaic efficiencies frequently exceeding 80 to 90 %[Chen2022b; Fan2022a; Fang2023; Xu2023]. Moreover, Yuan et al.[Yuan2024] reported that sequential electrocatalytic nitrate-to-ammonia conversion in a single-pass cell can be tuned by controlling the intermediate residence time, which strongly influences product selectivity. These works, discussed in the state-of-the-art section of this dissertation, underscore that reactor hydrodynamics and transport phenomena are as decisive as catalyst composition for achieving high FE at technologically relevant rates. Gao et al. present a membrane-free flow electrolyzer that couples the cathodic nitrate reduction reaction (eNO_3RR) to NH_3 with the anodic chlorine evolution reaction from Cl^-, using nitrate- and chloride-containing wastewaters as electrolytes[Gao2024]. The core

of the concept is a gas-extraction electrode, in which a Cu- or RuO_2-based electrocatalyst layer is integrated with a hydrophobic gas-diffusion layer to form a three-phase boundary that simultaneously enables high-rate electrosynthesis and in situ stripping of NH_3 and Cl_2, thereby suppressing their mutual homogeneous reaction and product losses. It was demonstrated that the residual concentrations of N/Cl species were below regulatory limits for wastewater discharges into receiving waters bodies[Gao2024].

Most literature studies have been conducted in alkaline electrolytes, which permit the use of non-noble metal electrodes and generally mitigate parasitic hydrogen evolution reaction (HER) at low pH values. In neutral or alkaline environments, the electrochemical reduction of nitrate proceeds according to

$$NO_3^- + 6\,H_2O + 8\,e^- \longrightarrow NH_3 + 9\,OH^- \tag{5.1}$$

$$H_2O \longrightarrow H^* + OH^* \tag{5.2}$$

and involves a complex nine-proton-coupled electron transfer mechanism. This pathway depends on proton supply via water dissociation (reaction 5.2), leading to high energy barriers and sluggish kinetics. In contrast, conducting nitrate reduction under acidic conditions offers several distinct advantages.[Zhan2023] The direct availability of protons promotes more efficient electron transfer and thereby reduces the required energy input and is thermodynamically favorable (s. Figure A.1). However, most previous studies have employed batch reactors or simple single-pass flow cells, which do not adequately resolve challenges related to concentration gradients along the electrode during scale-up, stable operation, thermal management, or mass transport. Systematic investigations of reactor design remain scarce. Yuan et al.[Yuan2024], for instance, examined different cell configurations and achieved a 91 % FE in a 5 cm^2 electrolyzer but could not explore high conversion rates or phenomena independent of the NO_3^- concentration.

In this chapter, the eNO_3RR is investigated in acidic media to prevent ammonia losses through volatilization, a common issue in neutral and

alkaline systems. Under these conditions, stable ammonium-containing compounds such as NH_4NO_3 and $(NH_4)_2SO_4$ are formed, which can be directly utilized as nitrogen-rich fertilizers in agricultural applications. A temperature-controlled continuous reactor operating in feed-and-bleed mode is employed[Baes2025]. This configuration decouples conversion from mass transfer, a feature that cannot be achieved with conventional single-pass or batch reactors, and thus provides a well-defined platform to probe mass-transport-controlled regimes and intrinsic selectivity.

The specific objectives of this chapter are threefold. First, a continuous feed-and-bleed electrochemical reactor is designed and characterized, which is equipped with a copper foam cathode modified by electrodeposited Cu dendrites, and operated with a bipolar membrane under acidic conditions. Second, the influence of electrolyte composition and pH, steady-state nitrate concentration, and applied current density on cell voltage is systematically investigated, as well as the product distribution, and FE, with particular attention to the onset of mass-transport limitations and membrane degradation by NH_4^+. Third, the role of hydrodynamics is analyzed by varying the catholyte recirculation flow rate and interpreting the resulting trends in terms of diffusion-layer thickness and transport numbers, thereby deriving reactor-level design guidelines that complement the catalyst-focused insights of previous chapters.

5.2. Materials and Methods

5.2.1. Experimental Setup

A continuous feed-and-bleed set-up, schematically illustrated in Figure 5.1 and shown photographically in the Supplementary Figures of this dissertation, was utilized on the cathode side to investigate the electrochemical reduction of nitrate to ammonia. A detailed description of the feed-and-bleed set-up can be found in the work of Bäßler et al. [Baes2025]. In short, a circulation pump is used to recirculate catholyte continuously through the electrochemical cell. A phase separator, also referred to as an overflow, functions both as gas-liquid separator and catholyte reservoir. In this reservoir, fresh catholyte can be fed (feed) to replenish consumed nitrate. An overflow (bleed) is then continuously drawn from the system to maintain a constant catholyte volume. This operation mode ensures decoupled mass transfer and conversion. The recirculation pump determines the hydrodynamic conditions and thus the mass transfer coefficient, while the feed pump sets the net conversion by adjusting the residence time of the electrolyte. With the conditions employed in this chapter, steady-state operation of the cathode side of the cell was typically achieved after approximately 20 min (Figure A.2), as evidenced by constant concentrations of nitrate and ammonia. The corresponding nitrate and ammonia concentrations are referred to as steady-state concentrations in the following.

5.2.2. Electrochemical Cell

A zero-gap electrochemical cell (Flex-E-Cell, FXC Engineering) was used, equipped with a titanium flow field and a copper foam cathode with a geometric area of 5 cm by 5 cm (1.6 mm thick, 50 ppi, $\geq$ 99.9 % purity, AlCarbon). The cathode was further modified via rapid electrodeposition of copper dendrites to increase the electrochemically active surface area, adapted from Bäßler et al.[Baes2024] without the oxidation step[Huan2016; Huan2017]. The copper dendrites were deposited using an electrolyte of 3 mol L^{-1} H_2SO_4 and 0.1 mol L^{-1} $CuSO_4$ (Sigma Aldrich,

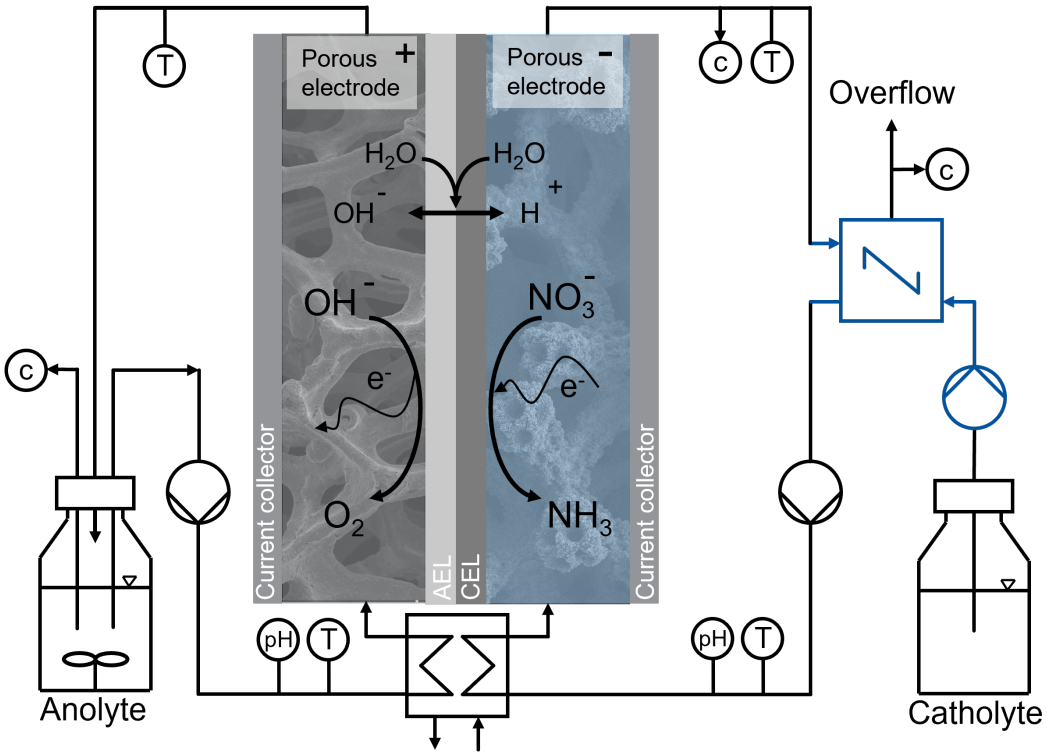

Figure 5.1.: Schematic of the feed-and-bleed setup, including the two electrolyte circuits (anolyte and catholyte), the electrochemical cell, and the additional feed and overflow lines for electrolyte and produced gas. Changes compared to the batch setup are highlighted in blue.

$\geq$ 99 % purity). A constant current density of 1500 mA cm^{-2} was applied for 60 s, corresponding to a charge of 90 C cm^{-2}, followed by washing with ultrapure water (resistivity: 18.2 MΩ cm).

A bipolar membrane (Fumatech FBM PK-75) in reverse bias was used as separator between catholyte and anolyte. The anode consisted of nickel foam (4 mm thick, $\geq$ 99.8 % purity, Sigma Aldrich) and was paired with a self-made titanium flow field as current collector, analogous to the cathode side. All gaskets were fabricated from Santoprene to ensure tight sealing and chemical resistance. Electrolyte flow through the cell was oriented bottom-to-top to facilitate gas removal.

Electrolyte solutions were prepared using ultrapure water (resistivity: 18.2 MΩ cm) in 5 L batches. Supporting electrolytes were KOH (Sigma Aldrich, $\geq$ 90 % purity), H_2SO_4 (Sigma Aldrich, 5 M stock), or Na_2SO_4 (Carl Roth, $\geq$ 99 % purity). Nitrate substrate was provided as KNO_3 (Fisher Scientific, $\geq$ 99 % purity). As starting electrolyte, nitrate concentrations of $c_0(NO_3^-) = 4000$ mg L^{-1} were chosen. During the experiments, conversions of 62.5 %, 75 %, and 87.5 % were targeted, corresponding to steady-state nitrate concentrations of 1500, 1000, and 500 mg L^{-1} in the circulating electrolyte.

The catholyte and anolyte were stored in separate 250 mL Schott flasks. Catholyte circulation was facilitated by gear pumps (GATHER) at a standard flow rate of 100 mL min^{-1}, unless otherwise specified, while anolyte circulation employed valveless rotary piston dispensing pumps (MCP-CPF, Ismatec). A digital peristaltic pump (Ismatec) delivered fresh catholyte at a controlled feed rate into the overflow reservoir.

The electrolyte temperature was regulated using a Julabo Cryostat 900F. The temperature and pH of both electrolyte inlets were continuously monitored using a Knick SE 555X/1-NMSN pH sensor, while Pt100 thermosensors were used to record the outlet temperature. Nitrogen gas (purity $\geq$ 99.999 %) and CO_2 (purity $\geq$ 99.998 %) were supplied at constant flow rates of 195 mL min^{-1} and 5 mL min^{-1}, respectively, through the overflow vessel to maintain an inert atmosphere and to provide a defined CO_2 dopant for gas analysis. Gas flow rates were regulated by a digital flow

controller (Analyt-MTC, MFC). The outlet gas flow was measured redundantly using a mass flow meter (Alicat Whisper, MFM) and by calculating the volume flow of CO_2 from its known inlet flow and its fraction in the outlet stream determined by gas chromatography (GC). All controllers and sensors were adjusted, and data were recorded using an echem-workstation (ZUMOLab GmbH).

5.2.3. Experimental Procedure

The electrochemical cell was assembled as described above, and the circuits were flushed with the respective electrolytes to remove air until all channels were completely filled. Nitrogen was purged into the overflow reservoir to establish an inert atmosphere and to degas the electrolyte. All experiments were operated until a steady state was reached, which was then maintained for at least 30 min.

Experiments were conducted under galvanostatic control using a Bio-Logic SP-150e potentiostat equipped with a VMP3B-20 booster. Applied current densities ranged from 50 to 450 mA cm^{-2}, and the cell voltage was recorded continuously. Potentials were measured using a reversible hydrogen electrode (RHE, Hydroflex, Gaskatel). Samples of the catholyte were collected every 5 min, while anolyte samples were collected every 15 min.

5.2.4. Transient Phase

The transient phase refers to the period in which the product concentration is < 98 % of the steady-state value. The duration of the transient phase t_{98} can be calculated using the following equation derived from the ideally-mixed model:[Baes2025]

$$t_{98} = -\frac{V_R}{\dot{V}_{\text{feed}}} \ln(1 - 0.98) \tag{5.3}$$

5.2.5. Analysis

Gas-phase analysis was performed using an Agilent 8890 GC system with helium as carrier gas. For H_2, O_2, and N_2 analysis, 100 µL samples were injected into a HaysepQQ column (3 m, 1 mm ID), an MS5A column (1.5 m, 1 mm ID), and a HaysepQ column (1.5 m, 1 mm ID), with helium flowing at 6.43 mL min^{-1}. NH_3 and N_2O were analyzed using a PoraPlot Amine column (25 m, 0.53 mm ID) with a 250 µL sample loop and a helium flow rate of 4.77 mL min^{-1}. The oven temperature was set to 50 °C. Chromatograms were processed using OpenLab CDS software. To calculate the flow rates of the investigated gaseous species, the total gas flow was determined as described above by direct measurement and by CO_2-based calibration. For all experiments, no ammonia could be detected in the gas phase above the 50 mg L^{-1} detection limit.

Liquid electrolyte samples were analyzed for nitrate, nitrite, ammonium, sodium, and chloride using ion chromatography (IC) (two 930 Compact IC Flex systems, one configured for anions and one for cations) with conductivity detection. For anion measurements, the eluent was a 3.6 mM Na_2CO_3 solution delivered at 0.7 mL min^{-1} under 11.49 MPa pressure. Analysis was performed over 35 min using a Metrosep A Supp 7–250/4.0 column maintained at 45 °C. For cation measurements, the eluent consisted of 1.7 mM HNO_3 and 1.7 mM dipicolinic acid, was pressurized to 11.66 MPa, and was pumped at 0.9 mL min^{-1} through a Metrosep C 6-250/4.0 column at 30 °C.

To ensure accurate quantification, all measured species had to remain in their ionic forms. Nitrate is fully dissociated in water (pK_a of HNO_3 = –1.37). Nitrite (HNO_2, $pK_a = 3.3$) requires a pH above 4 for accurate measurement, while ammonium (pK_a of NH_4^+ = 9.25) requires conditions below pH 9. Therefore, samples were diluted and adjusted to near-neutral conditions with K_3PO_4 prior to analysis. Precipitates were removed using a 0.2 µm filter (Chromafil Xtra PTFE, Macherey-Nagel) before injection.

Process performance was quantified in terms of FE for each product, evaluated following the approach of Bäßler et al.[Baes2025]. The FE was consistently calculated as a discrete value at each sampling time (Equation S1), rather than as a cumulative average over the entire experiment, to

capture rapid dynamic changes during transient and quasi-steady operation.

5.3. Results and Discussion

The performance of electrochemical nitrate reduction toward ammonia in the continuous feed-and-bleed reactor was investigated as a function of electrolyte composition, pH, steady-state nitrate concentration, applied current density, and catholyte recirculation flow rate. This section first compares acidic, neutral, and alkaline conditions, then examines the influence of nitrate conversion and product accumulation on cell voltage and FE, and finally analyzes mass-transport phenomena using both current-density-dependent behavior and hydrodynamic variation.

The reaction medium and pH are known to strongly influence product formation and, consequently, the FE of electrochemical nitrate reduction[Guo2023; Barr2023]. Figure 5.2 compares the FE for NH_3 under acidic (H_2SO_4), neutral (Na_2SO_4), and alkaline (KOH) conditions at high conversion rates ($\geq 95\,\%$), corresponding to steady-state nitrate concentrations $c(NO_3^-) \leq 300\,\mathrm{mg\,L^{-1}}$. All experiments employed an initial nitrate concentration $c_0(NO_3^-) = 4000\,\mathrm{mg\,L^{-1}}$ in 0.1 M supporting electrolyte and a current density of $150\,\mathrm{mA\,cm^{-2}}$.

The highest FE toward NH_3 is achieved under acidic conditions. In contrast, both the NH_3-specific and overall FE decrease in neutral and alkaline electrolytes. Under these conditions, additional side products such as NO_2^- are formed, and the reduced total FE suggests the formation of nitrogen-containing gases [Dort2013]. We propose that the rate-determining step in the NO_3^- reduction pathway shifts with the pH of the electrolyte [Cost2025]. In alkaline media, the reduction of NO_3^- to NO_2^- occurs efficiently, but the limited proton availability hampers further protonation steps, leading to the formation of undetected by-products and a lower overall FE [Plet1979; Pére2017; Barr2023; Zhan2023]. In acidic media, by contrast, the initial reduction step is rate-limiting, while subsequent protonation steps proceed rapidly owing to the high proton concentration [Zhan2023].

Copper exhibits limited stability in strongly acidic environments, resulting in minor corrosion even under cathodic protection. Although copper

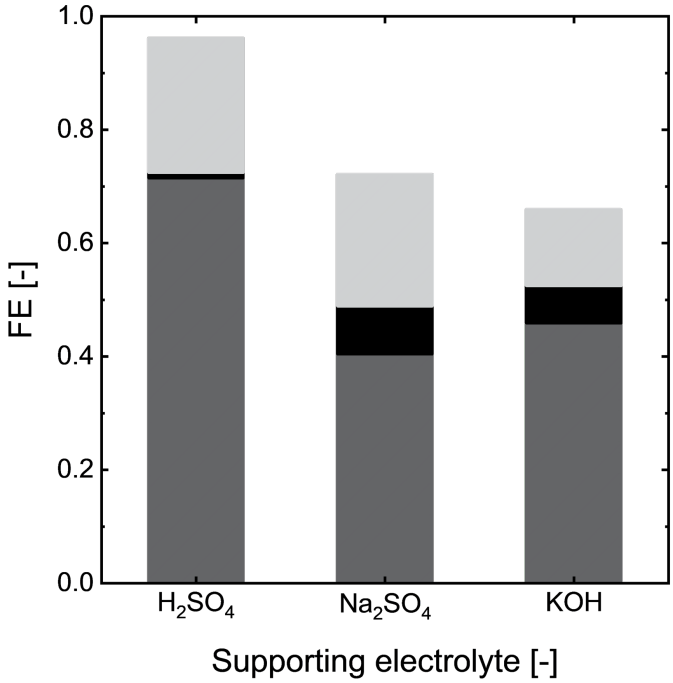

Figure 5.2.: Comparison of the FE for acidic (H_2SO_4), neutral (Na_2SO_4), and alkaline (KOH) conditions at high conversion rates ($X_{NO_3^-} \geq 95\,\%$), corresponding to steady-state nitrate concentrations $c(NO_3^-) \leq 300\,mg\,L^{-1}$. Electrolyte: $c_0(NO_3^-) = 4000\,mg\,L^{-1}$ in 0.1 M H_2SO_4, Na_2SO_4, or KOH; current density: $150\,mA\,cm^{-2}$.

corrosion was not quantified in this chapter, electrode stability remains a critical parameter for industrial applications. The use of corrosion-resistant coatings or copper-based alloys could mitigate this issue[dVooy2000; Guan2024; Phu2024; Chen2024b; Yang2023]. Despite these challenges, acidic conditions were selected for the subsequent experiments in this chapter, unlike most previous work [Xu2023; Yuan2024] because of their superior selectivity toward NH_3.

The FE strongly depends on the steady-state NO_3^- concentration, particularly when high conversion of initially low nitrate concentrations is targeted. Figure 5.3 shows the FE to ammonia at different steady-state NO_3^- concentrations and various current densities. At a low current density of $50\,mA\,cm^{-2}$, the highest FE of 94 % is observed. At lower nitrate concentrations, the FE toward NH_3 decreases slightly, and a small increase in H_2 formation is detected. Similar trends are observed up to $150\,mA\,cm^{-2}$.

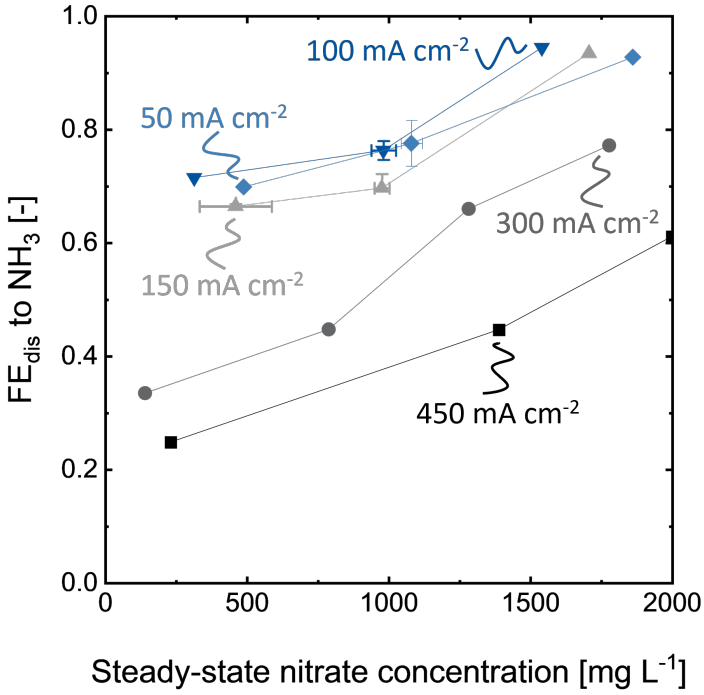

Figure 5.3.: Dependence of the FE on steady-state nitrate concentration $c(NO_3^-)$ for different current densities (50 , 100 , 150 , 300 , and 450 mA cm^{-2}). Electrolyte: $c_0(NO_3^-) = 4000$ mg L^{-1} in 0.1 M H_2SO_4; error bars for 50 , 100 , and 150 mA cm^{-2} represent triplicate experiments.

At higher current densities, a significant increase in H_2 production is observed. At 450 mA cm^{-2}, a moderate FE of about 40 % is achieved at 1500 mg L^{-1} nitrate, which decreases to approximately 20 % at 500 mg L^{-1} nitrate. This trend suggests that mass transport increasingly limits the reaction under such conditions. Assuming diffusion is the dominant mode of mass transfer, Fick's law predicts a linear relationship between substrate flux and the concentration gradient between the bulk electrolyte and the electrode surface. Consequently, a twofold increase in nitrate concentration should double the diffusive flux and proportionally enhance the FE until a regime no longer limited by diffusion is reached.

Additionally, the product concentration plays a significant role in determining the reaction outcome. This initially appears counterintuitive, given the large overpotentials applied for eNO_3RR. However, because the working electrode potential is close to the onset potential of the HER, already

small changes in product accumulation can shift the Nernst potential of nitrate reduction below the HER onset, thereby suppressing the desired NH_3 formation and favoring H_2 evolution [Wang2023a; Syam2025]. Literature also suggests that the formed NH_3 may facilitate HER by enhancing proton transfer toward the electrode [Zhan2024b]. At the same time, the formation of NH_4^+ consumes protons and increases the local pH, which can slow down further NH_3 formation. Thus, increasing conversion deteriorates FE in two ways: mass-transfer limitations reduce nitrate availability, and thermodynamic shifts favor competing side reactions.

Figure 5.4 further illustrates the dependence of FE toward NH_3 and the main side products H_2 and NO_2^- on current density at a fixed steady-state nitrate concentration of 2000 mg L^{-1}. At 50 mA cm^{-2}, NH_3 is formed with an FE of approximately 94 %. Above 150 mA cm^{-2}, the FE toward NH_3 declines sharply, while H_2 formation increases. Nitrite is formed at low rates at small current densities and its observed concentration decreases with increasing current, suggesting that NO_2^- is a key intermediate that is more efficiently reduced to NH_3 at higher electron flux. The concomitant increase in H_2 indicates a transition to a regime where nitrate mass transport and/or proton availability are no longer sufficient to sustain selective eNO_3RR.

The effects of current density and steady-state bulk nitrate concentration on cell voltage were next examined under acidic conditions. In the feed-and-bleed configuration, steady-state operation was typically achieved within approximately 20 min (Figure A.2). As shown in Figure 5.5, the extent of NO_3^- conversion to NH_3 strongly influences the cell potential. Increasing the NO_3^- conversion from 1500 mg L^{-1} to 500 mg L^{-1} steady-state nitrate concentration, with a corresponding rise in NH_4^+ concentration from 500 mg L^{-1} to 800 mg L^{-1}, raised the cell voltage by approximately 2 V at a current density of 450 mA cm^{-2}.

We hypothesize that the observed increase in cell potential arises primarily from a substantial rise in the ohmic resistance of the bipolar membrane. This effect is macroscopically evident from the membrane's brownish discoloration and blister formation. In contrast, the cathode potential remained largely unchanged (Figure 5.5 (right)), indicating that the varia-

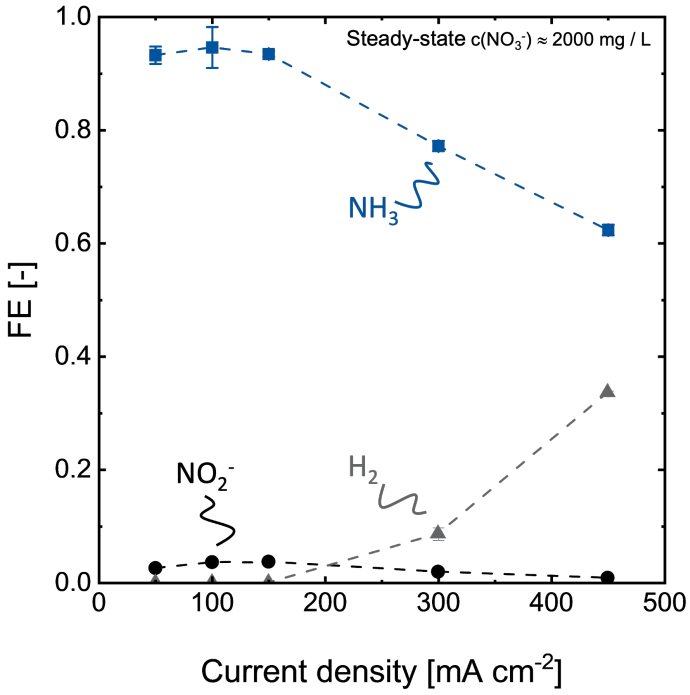

Figure 5.4.: Influence of current density on the FE toward NH_3 and the side products H_2 and NO_2^-. Steady-state nitrate concentration $c(NO_3^-) = 2000\,\mathrm{mg\,L^{-1}}$; electrolyte: $c_0(NO_3^-) = 4000\,\mathrm{mg\,L^{-1}}$ in 0.1 M H_2SO_4.

tion originates from changes within the membrane itself rather than from altered cathode kinetics. An increase in membrane resistance caused by NH_4^+ is well established in fuel cell studies [Raja2003; Hals2004; Hals2006; Huan2025]. NH_4^+ ions displace H_3O^+ from sulfonate sites in cation-exchange layers via electrostatic and van der Waals interactions, thereby reducing the number of mobile protons, decreasing membrane hydration, and increasing the energy barrier for ion transport [Urib2002; Raja2003; Hals2006; Mitt2007; Huan2025]. These combined effects diminish ionic conductivity. Mitigation strategies include using membranes with low affinity for NH_4^+ and operating conditions that limit ammonium uptake, maintain hydration, and preserve the proton-conductive form of nitrogen species.

To further elucidate mass-transport effects, the partial current density for NH_3 formation is plotted as a function of total current density in Figure 5.6 for different steady-state nitrate concentrations. For all shown concentrations, an almost linear increase in NH_3 partial current

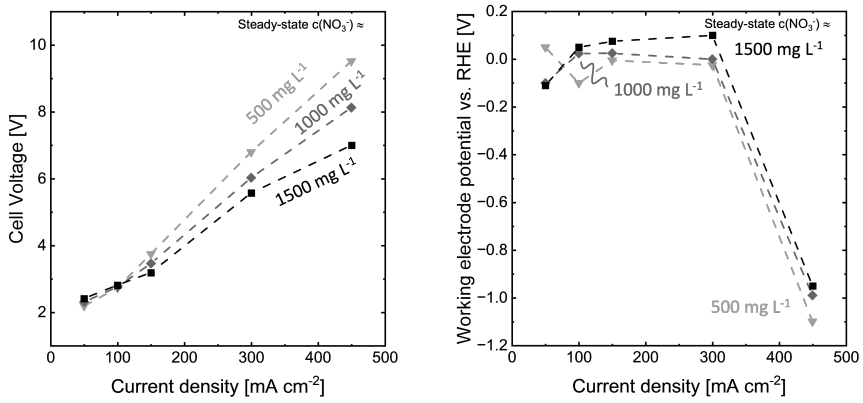

Figure 5.5.: Dependence of the cell voltage on current density for different steady-state nitrate concentrations $c(NO_3^-)$ in the range 500 to 1500 mg L^{-1}. Starting electrolyte $c_0(NO_3^-) = 4000$ mg L^{-1} in 0.1 M H_2SO_4.

density is observed with increasing total current density up to approximately 150 mA cm^{-2}. Beyond this point, the rate of increase approaches a plateau below 300 mA cm^{-2}, with a maximum production rate of about 1.27 mmol cm^{-2} h^{-1} (Figure S3). The plateau level strongly depends on the steady-state nitrate concentration.

Under these conditions, nitrate mass transport becomes limiting, leading to a decline in FE toward NH_3 due to competing HER. While FE remains close to 100 % at low current densities, it decreases at higher current densities as hydrogen evolution gains in importance. The rising electrode potential at higher currents further promotes HER [Adam1971; Jans1978; Wang2023a; Syam2025]. On the one hand, hydrogen bubbles may enhance NH_3 production by increasing local convection near the electrode, thereby improving mass transport. On the other hand, increased proton consumption by HER alters the local pH toward more alkaline conditions at the catalyst surface, potentially slowing protonation steps and thus reducing NH_3 yield [dVooy2000]. These opposing mechanisms highlight the complex interplay of kinetics and transport in porous electrodes.

To experimentally confirm the hypothesis of mass-transport limitation and to probe hydrodynamic effects, the catholyte recirculation flow rate through the cell was systematically varied. Higher flow rates reduce the diffusion-layer thickness and thereby enhance mass transfer within the

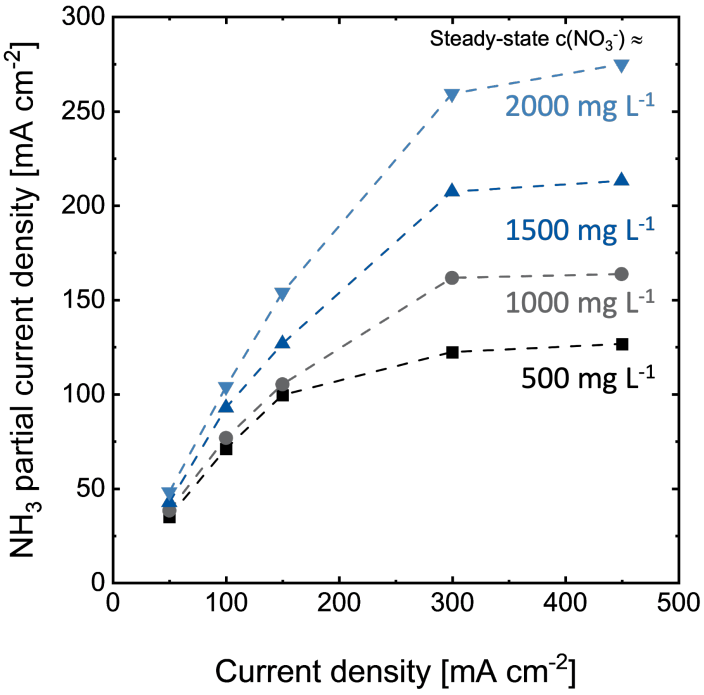

Figure 5.6.: Influence of current density on the partial current density toward NH_3 for different steady-state nitrate concentrations in the range 500 to 2000 mg L^{-1}. Electrolyte: $c_0(NO_3^-) = 4000$ mg L^{-1} in 0.1 M H_2SO_4.

electrode structure. By gradually increasing the recirculation rate from 100 mL min^{-1} to 700 mL min^{-1}, the diffusive boundary layer was progressively thinned, while the copper foam cathode additionally acted as a static mixer.

Figure 5.7 illustrates the resulting FE toward NH_3, NO_2^-, and H_2 at a fixed current density of 150 mA cm^{-2} and steady-state nitrate concentration of 200 mg L^{-1}. The feed-and-bleed setup enables steady-state operation at constant bulk nitrate concentration independent of the recirculation rate, such that changes in FE can be attributed primarily to hydrodynamics.

As the recirculation flow rate increases, FE toward NH_3 initially increases markedly. Tripling the recirculation flow from 100 mL min^{-1} to 300 mL min^{-1} significantly enhances the FE, reflecting improved reactant supply at the electrode surface. At higher flow rates, the gains in FE become smaller, approaching a plateau consistent with the exponential thinning of the diffusive boundary layer expected from classical mass-transfer correla-

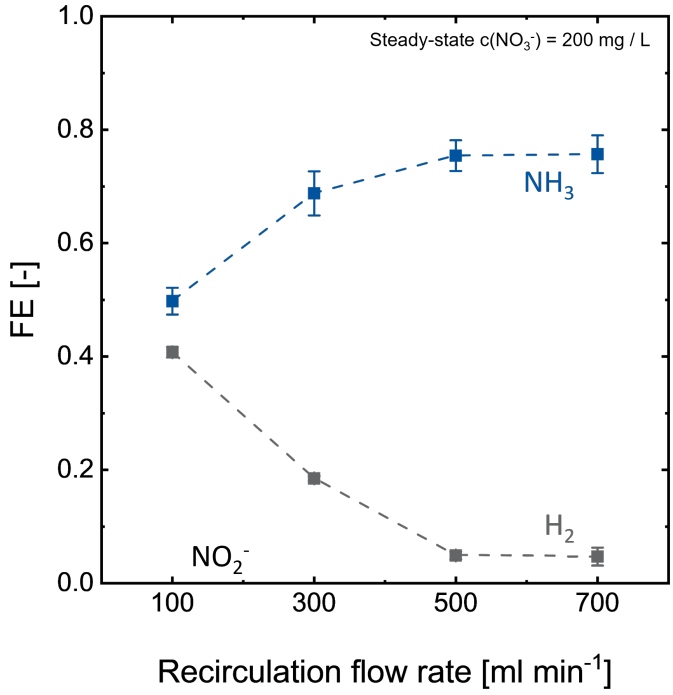

Figure 5.7.: FE for NH_3, NO_2^-, and H_2 at different recirculation flow rates. Steady-state nitrate concentration $c(NO_3^-) = 200\,mg\,L^{-1}$; electrolyte: $c_0(NO_3^-) = 4000\,mg\,L^{-1}$ in 0.1 M H_2SO_4; current density: $150\,mA\,cm^{-2}$.

tions[Schm2003].

Hydrodynamics also affects gas bubble behavior. Higher flow rates reduce the residence time and size of hydrogen bubbles before detachment, thereby preventing blockage of active sites and increasing the effective surface area of the electrode [Liu2015; Rox2023]. Consequently, boundary layer thickness, mixing, and surface availability are improved. At the same time, a minor increase in nitrite formation is observed at high recirculation flow (Figure 5.7). This behavior can be attributed to the thinner boundary layer, which allows reactive intermediates such as NO_2^- to diffuse into the bulk electrolyte before further reduction. As a result, fewer intermediates remain in the vicinity of the catalyst for conversion to NH_3, slightly lowering the FE toward the desired product and decreasing the overall nitrogen balance within the cathode compartment.

To quantitatively validate diffusion limitation, the effective diffusion-layer thickness was estimated using the ratio of bulk nitrate concentration to the

limiting current for NH_3 formation. Because the effective diffusion coefficient differs in porous media, an explicit value is difficult to obtain; instead, the ratio $i_{\text{lim}}/c_{\text{bulk}}$ is evaluated at different flow rates. This ratio represents a measure of the mass-transfer performance analogous to k_{L} and can be interpreted as an effective transport resistance. As shown in Figure 5.8, this normalized quantity increases with increasing recirculation flow rate. This trend confirms that enhanced hydrodynamics improve mass transport to the electrode surface, thereby mitigating diffusion limitations. The observed behavior aligns with established correlations between Sherwood and Reynolds numbers for interstitial and superficial flow in the foam, which predict improved mass transfer with increasing flow velocity (Figure A.3) [Lang1989a; Lang1989b; Lang1990a; Lang1990b; Brow1994]. This leads to the conclusion, that increasing the recirculation flow rate can still effectively enhance mass transport above the investigated regime.

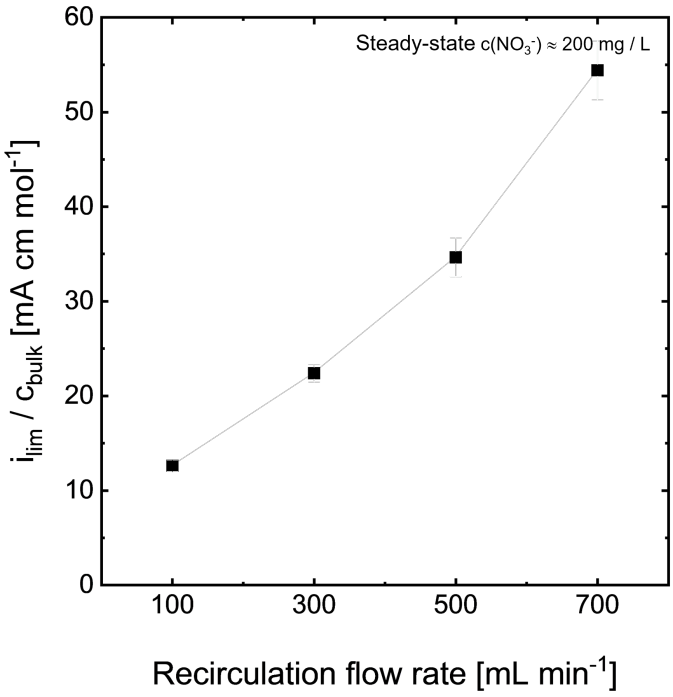

Figure 5.8.: Dependence of the limiting current divided by the bulk concentration, $i_{\text{lim}}/c_{\text{bulk}}$, on recirculation flow rate. Steady-state nitrate concentration $c(NO_3^-) \approx 200\,\text{mg}\,\text{L}^{-1}$; electrolyte: $c_0(NO_3^-) = 4000\,\text{mg}\,\text{L}^{-1}$ in 0.1 M H_2SO_4; current density: $150\,\text{mA}\,\text{cm}^{-2}$.

Enhancing the cell with the gained knowledge and operating at a cur-

rent density of 600 mA cm^{-2} and a recirculation flow rate of 1000 mL min^{-1} yielded a FE of 94.6 % and a nitrate conversion of 50 %, thereby demonstrating the practical viability of the feed-and-bleed concept for high-rate ammonia synthesis from nitrate-contaminated waters.

These findings demonstrate that enhanced mixing, achieved through higher recirculation flow rates and appropriate electrode geometries, can effectively mitigate mass-transport limitations and improve the efficiency of ammonia production. They also provide a quantitative basis for linking hydrodynamic operation windows, characterized by Reynolds and Sherwood numbers, to electrochemical performance.

5.4. Conclusion

In this chapter, the electrochemical reduction of nitrate to ammonia was investigated in a temperature-controlled, continuous feed-and-bleed reactor equipped with a dendrite-modified copper foam cathode and operated under acidic conditions. By systematically varying electrolyte composition and pH, steady-state nitrate concentration, current density, and recirculation flow rate, we identified the key physicochemical factors governing FE, cell voltage, and overall process performance under near-industrial conditions.

First, acidic electrolytes were shown to provide the highest FE toward NH_3, with values up to 94 % at low current densities. The high proton availability in acidic media facilitates the multistep proton-coupled electron transfer sequence required for nitrate reduction and suppresses the accumulation of nitrite and other intermediates. Neutral and alkaline conditions, by contrast, exhibited lower FE and higher fractions of side products, consistent with limited proton supply and altered rate-determining steps. From a broader dissertation perspective, this result complements the thermodynamic analysis presented in the fundamentals chapter by demonstrating, under realistic operating conditions, that acidic environments can be preferable for eNO_3RR despite concerns about catalyst stability.

Second, the feed-and-bleed reactor configuration enabled steady-state operation at controlled nitrate concentrations and revealed the strong influence of product accumulation on cell voltage and membrane resistance. Increasing nitrate conversion, and with it the NH_4^+ concentration, caused a substantial rise in cell voltage, which was traced back to increased ohmic resistance and physical degradation of the bipolar membrane. This behavior is consistent with literature on NH_4^+ crossover in fuel cell membranes and underscores the need for ammonia-tolerant ion-exchange materials in eNO_3RR electrolyzers.

Third, by decoupling conversion from hydrodynamics, the feed-and-bleed setup allowed a clean identification of mass-transport limitations. The partial current density for NH_3 increased linearly with total current up

to about 150 mA cm^{-2} and then plateaued, indicating a transition from kinetically controlled to diffusion-limited operation. The onset of this plateau, and the concomitant increase in HER, was strongly dependent on steady-state nitrate concentration. This behavior was quantitatively linked to an effective diffusion-layer thickness that decreases logarithmically with recirculation flow rate, a hallmark of transport-limited processes in porous media. These results provide an experimentally grounded basis for the dimensionless transport framework (based on Re and Sh) developed in the electrochemical fundamentals chapter and demonstrate how it can be applied to real flow-cell geometries.

Fourth, hydrodynamic optimization by increasing the recirculation flow rate markedly enhanced the FE toward NH_3, particularly when transitioning from low to intermediate flow. In this regime, higher flow rates thinned the diffusion layer, promoted bubble detachment, and increased the effectively wetted electrode area, thereby alleviating mass-transport limitations. At very high flow rates, however, the incremental benefits diminished and a slight increase in nitrite formation was observed, which can be attributed to the enhanced escape of reaction intermediates into the bulk electrolyte. These findings highlight the existence of an optimal hydrodynamic operating window in which mass transport is intensified without compromising intermediate retention and selectivity. Operating the cell at a current density of 600 mA cm^{-2} and a recirculation flow rate of 1000 mL min^{-1} yielded an FE of 94.6 % and a nitrate conversion of 50 %, thereby demonstrating the practical viability of the feed-and-bleed concept for high-rate ammonia synthesis from nitrate-contaminated waters.

From a process integration perspective, the feed-and-bleed reactor concept studied bridges the gap between fundamental catalyst screening and realistic process configurations capable of handling fluctuating nitrate loads from wastewater streams. The insights gained regarding the interplay of conversion, hydrodynamics, and membrane behavior provide a crucial intermediate scale in the multiscale narrative of this dissertation: they connect the nanoscale catalyst properties and local reaction mechanisms discussed in earlier chapters to the system-level techno-economic and life-

cycle considerations that will be developed in the subsequent chapter.

Future work could involve detailed computational fluid dynamics simulations to further elucidate the interplay between flow patterns, mass transport, and reaction kinetics within the porous electrode structure. Additionally, further work should focus on tailoring electrode geometries with enhanced mixing performance (for example, graded-porosity foams or structured flow-through channels), on developing ammonia-tolerant bipolar membranes with reduced NH_4^+ uptake, and on extending the feed-and-bleed concept to real wastewater matrices with multi-component ionic backgrounds. The transition toward a wastewater electrolyzer will be subject of the next chapter.

6.

Catalyst-coated Membranes for Zero-Gap Nitrate Reduction

6.1. Introduction

The preceding chapters of this dissertation established a mechanistic framework for the electrochemical nitrate reduction reaction (electrochemical nitrate reduction reaction (eNO_3RR)) on copper-based electrodes in divided flow cells. In batch mode (chapter 4), the interplay between membrane selectivity, electrode material, and electrolyte composition was shown to govern faradaic efficiency (FE), product distribution, and nitrogen balance. In the continuous feed-and-bleed configuration (chapter 5), the focus shifted to hydrodynamics and mass transfer: by decoupling recirculation flow and residence time, the onset of mass-transport limitation and the role of diffusion-layer thickness were quantified for copper foams operated predominantly in alkaline media. Together, these chapters demonstrated that at high nitrate concentrations and sufficient ionic strength, copper foams can achieve FE_{NH_3} above 92 % at current densities up to 600 mA cm^{-2}. At lower nitrate concentrations or in neutral electrolytes without supporting electrolyte, however, the reaction becomes strongly hydrogen evolution reaction (HER)-dominated due to limited proton availability and severe mass-transport constraints.

Recent studies on eNO_3RR in membrane-based and zero-gap reactors demonstrate that copper remains a highly competitive catalyst class when combined with appropriate reactor engineering. Yuan et al.[Yuan2024] reported a current density of 395 mA cm^{-2} with a FE_{NH_3} of 70 % in a single-pass membrane electrode assembly (MEA) reactor using a copper-sputtered carbon substrate and a Nafion™ N117 separator, corresponding to an ammonia production rate of 1.78 mmol h^{-1} cm^{-2} in 1 mol L^{-1} KOH with 0.1 mol L^{-1} KNO_3.[Yuan2024] Li et al.[Li2023] achieved a FE_{NH_3} of 90 % at 400 mA cm^{-2} and an ammonia production rate of 1.6 mmol h^{-1} cm^{-2} using an oxide-derived copper catalyst on a copper mesh in a batch-flow cell with a Nafion™ N117 membrane and a recirculating catholyte containing 1 mol L^{-1} KOH and 0.1 mol L^{-1} KNO_3; when industrial wastewater was used as the catholyte, nitrate conversion of 99.3 % was obtained within 6 h.[Li2023]

Beyond classical two-chamber configurations, Chen et al.[Chen2024a] developed a three-chamber electrochemical reactor incorporating a porous solid electrolyte layer, enabling alkali cation shuttling without large amounts of supporting salt and achieving FE_{NH_3} of 90 % at 100 mA cm^{-2} for nitrate concentrations of 2000 mg L^{-1} in single-pass mode.[Chen2024a] Although many publications focussing on zero-gap electrolysis with the catalyst pressed against the membrane, only a few sources studied catalyst-coated membrane (CCM). Boppella et al.[Bopp2024] employed pulsed electrolysis in a CCM-based reactor with $Cu_x - Ru_y$ alloy catalysts and showed that dynamic operation can nearly double the FE and triple the ammonia yield rate compared to steady-state electrolysis; in an anion exchange membrane (AEM)-based CCM, they reported $FE_{NH_3} > 90$ % at 200 mA cm^{-2}, an ammonia yield rate of (5.74 ± 0.27) mmol h^{-1} cm^{-2}, and stable operation over 100 h at 600 mA cm^{-2}.[Bopp2024] Complementary studies by Huang et al.[Huan2024b] with a $RuIn_3$/C catalyst in 0.1 mol L^{-1} KOH containing 10 mmol L^{-1} NO_3^- achieved a FE_{NH_3} of 97.6 %, an ammonia yield rate of 2.7 mmol h^{-1} mg^{-1}_{Ru}, and a nitrate conversion of approximately 96.4 % under pulsed electrolysis conditions.[Huan2024b]

With the setup used in chapter 5 for copper foams operated in neutral electrolytes, it was shown the eNO_3RR towards ammonia becomes less decisive and intermediates such as nitrite and hydrogen forming instead. Without further supporting salts, HER becomes even more dominant. Under these conditions, the limiting factor is not the intrinsic activity of copper but rather the inability to provide sufficient protons to protonate nitrate and its intermediates at the catalyst surface [Huan2024b]. A natural extension is therefore to employ a CCM on a cation exchange membrane (CEM). In this configuration, sulfonic acid groups in the ionomer and membrane can maintain a locally acidic, proton-rich microenvironment at the copper catalyst, even if the bulk catholyte is only weakly acidic or has low ionic strength. This decoupling of bulk composition and interfacial pH is expected to facilitate the proton-coupled electron transfer steps in the eNO_3RR and to mitigate the HER dominance observed for copper foams in neutral media.

Motivated by these considerations, this chapter investigates eNO_3RR on copper-based CCMs operated in a zero-gap flow cell. It is hypothesized that the ionomer-membrane microenvironment can restore high local proton availability and thereby enhance FE_{NH_3} at moderate and high nitrate concentrations compared to neutral, foam-based systems.

6.2. Materials and Methods

6.2.1. Membrane Electrode Assembly and Cell Configuration

The experiments in this chapter were conducted in a modified zero-gap flow cell based on the Flex-E-Cell design already introduced (chapter 5). In contrast to the copper foam cathodes used previously, the cathode used in this chapter consisted of a copper-based CCM mounted between two titanium gas diffusion layers (Ti-gas diffusion layers (GDLs) (Ti-GDL, 250 µm, Quintech)) with flow-by electrolyte flow behind the CCM.

The cell configuration employed a geometric active area of 1 cm^2 for both anode and cathode. On each side, a VeroClear polymer flow field was sealed to the housing by a Santoprene® gasket and connected to a titanium current collector. The current collector featured two longitudinal slits facing the housing and a central grid region supporting the Ti-GDL. The catholyte entered the lower slit, was forced through the Ti-GDL and the adjacent CCM, and exited through the upper slit, thereby establishing a well-defined through-plane flow and a thin hydrodynamic boundary layer at the catalyst-electrolyte interface. A shallow recess in the titanium plate accommodated a ePTFE frame that sealed the periphery of the CCM and defined the active area.

On the anode side, an analogous configuration was used. A platinum-coated Ti-GDL served as anode. The two half-cells were assembled symmetrically, with the CCM centered between the GDLs and compressed to a defined torque of 5 N m using four bolts. This torque was determined from pressure-sensitive film measurements to produce a homogeneous surface pressure on the MEA while avoiding mechanical damage to the membrane.

Pressure film tests confirmed that in this configuration the contact pressure was uniform over the pressurized active area and that no internal or external leakage paths remained. Regions of high pressure coincided with the titanium grid, while electrolyte channels were visible as low-pressure regions between grid bars. Outside the grid, the pressure distribution was

homogeneous, indicating reliable sealing against the environment. These mechanical diagnostics were essential to ensure that the electrochemical measurements discussed below are not artifacts of membrane bypass currents or leakage flows.

6.2.2. Preparation of Copper-Based Catalyst-Coated Membranes

Copper-based CCMs were prepared on Nafion™ N117 using a decal transfer protocol adapted from standard fuel-cell practice and optimized for nanoparticulate copper catalysts.

Membrane Pretreatment

Prior to catalyst deposition, Nafion™ N117 membranes were cut into squares of 4 cm $\times$ 4 cm and subjected to a three-step pretreatment to remove organic contaminants, oxidizable residues and ionic impurities. The membranes were first sonicated in ultrapure water for 15 min, then immersed in 3 % hydrogen peroxide at 80 °C for 1 h to oxidatively remove organic species. After thorough rinsing with ultrapure water, the membranes were boiled in ultrapure water at 80 °C for 1 h to remove residual peroxide and low-molecular-weight species. Finally, they were treated in 0.5 mol L^{-1} H_2SO_4 at 80 °C for 1 h to protonate the sulfonic acid groups and displace cationic impurities. The membranes were subsequently rinsed with ultrapure water and stored fully hydrated until use.

Ink Preparation

The ink consisted of copper nanoparticles (Copper powder, 25 nm, 99.5%, Iolitec), deionized water, 1-propanol, and a low fraction of ionomer binder (Nafion™ (Nafion solution, 5 wt%, Quintech) or Sustainion® (Sustainion XA-9, 5 wt%, Dioxide Materials)). Two main ink compositions were employed, corresponding to ionomer-to-catalyst mass ratios (I/C) of 0.1 and 0.05, respectively.

For each batch, CuNPs was weighed into a glass vial and dispersed in deionized water by ultrasonication. 1-propanol and the desired ionomer solution were added to reach the target I_C ratio and overall solid content. The suspension was sonicated again and then magnetically stirred at 300 min^{-1} for at least 12 h to ensure homogenization. Immediately before coating, the ink was mixed and sonicated to break up any agglomerates.

Catalyst Coating

Catalyst layers were prepared on a 10 cm $\times$ 10 cm polytetrafluoroethylene (PTFE) substrate using a mechanically fixed PTFE frame as coating mask. The frame, with a central cut-out of 1 cm $\times$ 1 cm and a thickness of 25 µm, was hot-pressed onto the substrate at 160 °C and 50 bar to prevent ink ingress underneath the mask. After cooling, 40 µL of ink were dispensed into the window and spread with a razor blade to obtain a uniform wet film. The coated substrates were dried at ambient conditions for at least 12 h until the solvents had fully evaporated, leaving an adherent copper-ionomer layer on the PTFE.

Decal Transfer

Decal transfer of the dried catalyst layer onto the pretreated Nafion™ membrane was performed in a two-step hot-pressing procedure. The dry membrane was first equilibrated in a vacuum oven at 80 °C to remove excess water while preserving partial hydration. The membrane was then placed onto the catalyst-coated PTFE substrate, covered with a thin PTFE protection sheet, wrapped in laboratory paper and positioned in the hot-press.

In the first step, the stack was pressed at 140 °C and 20 bar for 3 min. Immediately afterward, it was transferred to a cooled compartment of the press and cold-pressed at the same pressure for 1 min to promote adhesion while preventing excessive membrane deformation. After disassembly, the PTFE substrate was carefully peeled away and inspected for residual catalyst. Complete transfer resulted in a clean PTFE surface and

a visually uniform copper catalyst layer on the membrane. The CCM was then stored in dry-state until use.

6.2.3. Electrochemical Operation and Analytics

The electrochemical setup, feed-and-bleed configuration, and analytical methods closely follow those described in chapter 5. Unless stated otherwise, experiments were performed at 20 °C with a total catholyte loop volume of 35 mL and an anolyte volume of 150 mL. Anolyte and catholyte were circulated in separate loops. Catholyte operation was in feed-and-bleed mode with a controlled feed rate $\dot{V}_{\text{feed}}$, while the anolyte was circulated in batch mode.

The standard catholyte consisted of 0.1 mol L^{-1} H_2SO_4 containing nitrate at concentrations between 4000 mg L^{-1} and 12 000 mg L^{-1}, supplied as HNO_3. The anolyte was 0.1 mol L^{-1} H_2SO_4. For experiments without supporting electrolyte, the catholyte contained nitrate solely as HNO_3 without additional H_2SO_4, while the anolyte remained unchanged.

All electrochemical measurements were conducted at constant current with a BioLogic SP-150e potentiostat. constant current (CC) experiments were performed at current densities of 50 mA cm^{-2}, 100 mA cm^{-2}, and 150 mA cm^{-2}. Pulsed electrolysis experiments used symmetrical current pulses with $t_{\text{on}} = t_{\text{off}} = 0.1$ s; during t_{on} the current density was set to twice the current density of the CC experiment and to zero during t_{off}, such that the time-averaged current density matched the corresponding CC experiment. Galvanostatic electrochemical impedance spectroscopy (GEIS) was employed at selected operating points to determine the high-frequency resistance and to qualitatively assess interfacial dynamics.

Gas-phase analysis was carried out every 20 min by gas chromatography as in Chapter 5, using N_2 and CO_2 as carrier and tracer gases. Liquid catholyte samples (1 mL) were taken every 5 min and were analyzed by ion chromatography for nitrate, nitrite and ammonium. The FE was evaluated from the concentration-time data using the feed-and-bleed expressions derived in Chapter 5. No modifications to these equations were required

for the present system.

6.3. Results and Discussion

In this section, investigations will be presented to test the hypothesis that the ionomer-membrane microenvironment can restore high local proton availability and thereby enhance ammonia formation. First, the mechanical and hydraulic constraints of the CCM cell are discussed to justify the final active area and operating window. Subsequently, the dependence of FE_{NH_3} and production rate on nitrate concentration and hydrodynamics is examined. The impact of pulsed electrolysis on the local microenvironment is then evaluated, followed by a comparison of Nafion™and Sustainion® binders. Finally, the performance without supporting electrolyte is analyzed to assess the suitability of CCMs for low-ionic-strength wastewaters.

The initial implementation of the CCM concept employed an active area of 5 cm $\times$ 5 cm with Ti-GDLs and a mixed-metal iridium oxide anode, analogous to the 25 cm^2 configuration used in Chapter 5. In practice, however, it was not possible to obtain mechanically robust and hydraulically tight MEAs at this scale. Copper-based catalyst inks often cracked and delaminated during the drying process, causing the catalyst layer to detach from the substrate. Additionally, small defects in the gasket compression translated into electrolyte leakage and internal bypass channels. These effects compromised cell integrity and reproducibility to an extent that systematic studies were not feasible. To ensure reliable operation, the active area was therefore reduced to 1 cm $\times$ 1 cm, which allowed for stable, crack-free catalyst layers and reproducible, leak-tight assembly of the MEA.

This pragmatic reduction in electrode area introduces additional constraints for the interpretation of the data. First, the absolute gas and product formation rates scale directly with the geometric area. At a given current density, the total current of a 1 cm^2 electrode is a factor of 25 lower than in the 25 cm^2 configuration, so that the molar formation rates of NH_3 and gaseous by-products approach the detection limits of gas-phase analysis and require longer sampling times and carefully optimized analytical protocols. The ratio of reactor volume to reaction rate is thus increased, and the system responds more slowly in terms of measurable concentration

changes.

Second, the reduction in area also affects the approach to steady state in feed-and-bleed operation. For a given catholyte volume and practically achievable feed flow rates, the turnover in the present configuration with only a small active area is significantly lower than in the larger cell of Chapter 5. While the larger electrode allowed the use of relatively high feed rates and typical times to steady state on the order of 20 min, the combination of small geometric area and limited feed flow in the present setup results in much longer characteristic times to steady state, as estimated from the ideal mixing analysis in Equation (5.3). In practical terms, this means that several hundred minutes of operation would be required to reach fully developed steady-state outlet compositions for each new operating point.

As a consequence, most experiments in this chapter were evaluated under quasi-transient but slowly varying conditions. The focus is placed on FE and nitrogen balances in the later stages of each experiment, where the outlet composition changes only gradually, rather than on strictly stationary states. It is hypothesized that the CCM microenvironment can be analyzed under well-defined hydrodynamic and transport conditions[Lore2025].

6.3.1. Effect of Nitrate Concentration

A central element of the working hypothesis is that, once proton supply and local acidity are ensured by the CCM and the CEM, mass transport of nitrate through the electrolyte and the ionomer film becomes the dominant rate-limiting step. It is therefore hypothesized that an increase in the bulk nitrate concentration $c_0(NO_3^-)$ enlarges the diffusion-driven flux of NO_3^- towards the catalyst layer and thereby increases both the Faradaic efficiency towards ammonia FE_{NH_3} and the ammonia production rate. To test this hypothesis, galvanostatic experiments were performed at a fixed current density of 100 mA cm^{-2} in a catholyte consisting of 0.1 mol L^{-1} H_2SO_4 with bulk nitrate concentrations of 4000 mg L^{-1}, 8000 mg L^{-1}, and 12 000 mg L^{-1}.

Under the assumption of a stagnant diffusion layer with effective thick-

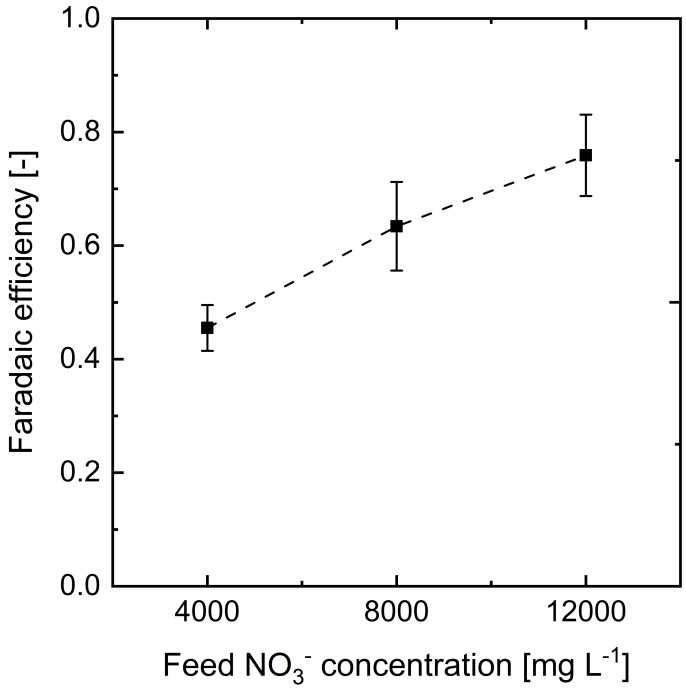

Figure 6.1.: Dependence of the Faradaic efficiency for NH_4^+ on the bulk NO_3^- feed concentration. Feed electrolyte $c_0(NO_3^-) = 4000$ to 12 000 mg L^{-1} in 0.1 M H_2SO_4; current density: 100 mA cm^{-2}; recirculation flow rate: 100 mL min^{-1}.

ness δ, the diffusion-limited molar flux of nitrate towards the catalyst surface can be approximated by Fick's law. As long as the surface concentration $c_{surf}(NO_3^-)$ remains small, the flux scales approximately linearly with $c_0(NO_3^-)$ (Equation (2.20)). In the CCM configuration, an increase in $c_0(NO_3^-)$ is thus expected to mitigate mass-transport limitations and to increase FE_{NH_3} at fixed current density.

At nitrate concentrations of 4000 mg L^{-1}, the Faradaic efficiency towards ammonia reached approximately 45 % and an almost closed total Faradaic efficiency. The corresponding ammonia production rate was 0.21 mmol h^{-1} cm^{-2}. The deficit in the nitrogen balance is consistent with minor analytical uncertainties and potential corrosion of residual copper on the GDL.

Increasing the nitrate concentration to 8000 mg L^{-1} led to an increase in FE_{NH_3} to about 63 % and an ammonia production rate of 0.29 mmol h^{-1} cm^{-2}. The apparent excess in the total Faradaic efficiency

is attributed to the limited temporal resolution and the detection threshold of the gas analysis rather than to systematic errors in liquid-phase quantification.

At the highest nitrate concentration of 12 000 mg L^{-1}, the Faradaic efficiency towards ammonia increased further to approximately 76 %, with an associated production rate of 0.35 mmol h^{-1} cm^{-2}. Under these conditions, no hydrogen was detected by the gas-phase analysis, even though gas evolution was observed at the cathode, indicating the formation of hydrogen gas below the detection limit. The nitrogen balance slightly exceeded 100 %, which reflects the combined effect of analytical uncertainty and the detection limit of the gas-phase measurements.

Across the investigated concentration range, the FE_{NH_3} increased approximately linearly with the bulk nitrate concentration. This trend is consistent with the diffusion model by Fick, in which the diffusion-limited flux $J_{NO_3^-}$ scales with $c_0(NO_3^-)$ for low surface concentrations. The data therefore confirm the hypothesis that, in the CCM configuration operated under acidic conditions, nitrate mass transport remains the primary rate-limiting factor once proton supply and local acidity are secured.

The average cell voltage decreased from about 2.7 V at $c_0(NO_3^-)$ = 4000 to 8000 mg L^{-1} to approximately 2.4 V at $c_0(NO_3^-)$ = 12 000 mg L^{-1}. The change in equilibrium potential expected from the Nernst equation for a threefold concentration change is on the order of a few mV and is therefore negligible compared to the observed difference in cell voltage. The lower cell voltage at higher nitrate concentration is attributed to improved interfacial kinetics and reduced local overpotentials, facilitated by the higher nitrate flux and a more homogeneous current distribution at the catalyst surface. The overall energy efficiency $\eta_{electr.}$ reached approximately 28 % at $c_0(NO_3^-)$ = 12 000 mg L^{-1}, compared to values in the range of 15-21 % at lower concentrations.

These results partially confirm the initial transport-limitation hypothesis. At moderate to high nitrate concentrations, the CCM architecture operated in acidic media delivers FE_{NH_3} up to approximately 76 %. At $c_0(NO_3^-) = 4000$ mg L^{-1}, a concentration already relevant for many nitrate-

rich wastewaters, FE_{NH_3} remains limited to roughly 45 %, which is significantly below the values achieved for copper foams at higher nitrate concentrations in Chapter 5. The working hypothesis that CCMs can fully compensate the limitations of porous electrodes at low nitrate concentrations is therefore refined as follows: once proton supply is ensured, nitrate mass transport through the electrolyte and ionomer layer remains the dominant limitation, and the planar geometry together with the finite diffusion path length in the CCM introduces additional transport constraints that cannot be overcome by proton enrichment alone.

6.3.2. Influence of Catholyte Circulation Flow

To further probe the role of mass transfer in the CCM configuration, the catholyte recirculation flow rate was varied at constant nitrate concentration $c_0(NO_3^-) = 12\,000\,\mathrm{mg\,L^{-1}}$ and current density $j = 100\,\mathrm{mA\,cm^{-2}}$. According to the one-dimensional Nernst–Planck description introduced in Equation (2.19), an increase in the convective velocity in the vicinity of the catalyst layer reduces the effective diffusion-layer thickness, steepens the concentration gradient, and thereby increases the flux of NO_3^- towards the catalyst. In hydrodynamically developed channel flow, this behavior is commonly expressed by an increase in the mass-transfer coefficient and the Sherwood number with increasing Reynolds number. An increase in recirculation flow rate is therefore expected to enhance the transport of nitrate to the CCM, mitigate local depletion, and improve FE_{NH_3}. In addition, higher flow rates are expected to facilitate the removal of gas bubbles from the catalyst surface, which may reduce the cell voltage.

At a recirculation rate of $80\,\mathrm{mL\,min^{-1}}$, the Faradaic efficiency towards ammonia was approximately 46 %, with a total Faradaic efficiency close to unity and an average cell voltage of about 2.6 V. Increasing the flow rate to $150\,\mathrm{mL\,min^{-1}}$ raised FE_{NH_3} to roughly 55 %, while the average cell voltage decreased slightly to approximately 2.5 V. At the highest flow rate of $220\,\mathrm{mL\,min^{-1}}$, the Faradaic efficiency towards ammonia reached the previously discussed value of about 76 %, and the average cell voltage further

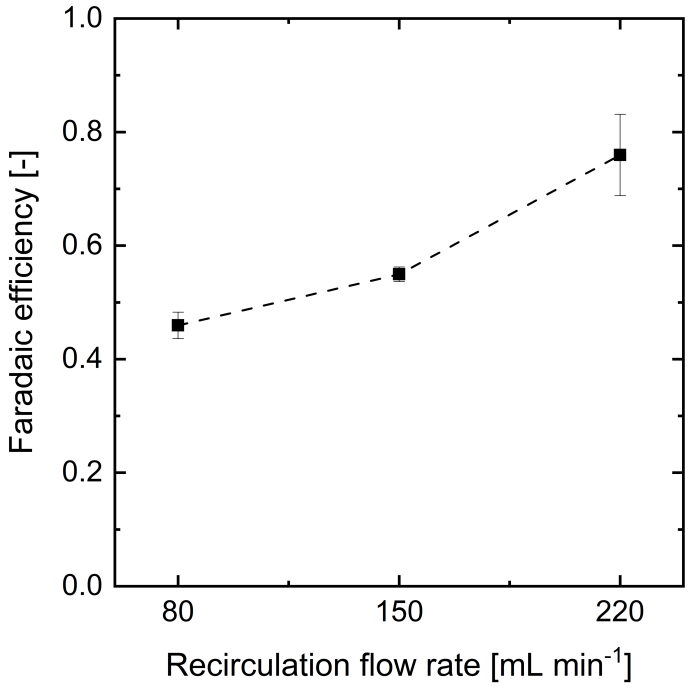

Figure 6.2.: Faradaic efficiency for NH_4^+ as a function of the recirculation flow rate. Starting electrolyte $c_0(NO_3^-) = 12\,000\,\mathrm{mg\,L^{-1}}$ in 0.1 M H_2SO_4; current density: $100\,\mathrm{mA\,cm^{-2}}$; recirculation flow rate: 80 to 220 $\mathrm{mL\,min^{-1}}$.

decreased to approximately 2.4 V.

For all three flow rates, the nitrogen balances were within a few percent of 100 %, indicating that ammonium and residual nitrate constituted the dominant nitrogen-containing species, while nitrite and gaseous nitrogen species remained negligible under the chosen conditions. The quasi-linear increase of FE_{NH_3} with recirculation flow rate is consistent with the increase in convective transport predicted by the hydrodynamic mass-transfer correlations introduced in Section 2.1.8. Enhanced convection at the CCM surface is thus almost as effective as an increase in bulk nitrate concentration in alleviating mass-transport limitations at fixed current density.

The observed decrease in cell voltage with increasing flow rate cannot be explained by changes in the thermodynamic equilibrium potentials, since the bulk electrolyte composition is maintained and the Nernst potentials of the relevant half-reactions remain essentially constant. Instead, the trend reflects a combination of hydrodynamic and interfacial effects. More ef-

ficient removal of gas bubbles from the catalyst surface increases the effectively wetted electrochemically active area and lowers the local current density. At the same time, thinner diffusion layers reduce concentration overpotentials for both eNO_3RR and HER and promote a more homogeneous current distribution across the CCM. Small variations in cell assembly and mechanical compression between individual experiments may influence the absolute voltage levels, but the monotonic decrease in cell voltage with increasing flow rate is indicative of a genuine hydrodynamic effect.

These results confirm the hydrodynamic hypothesis for the CCM system and are analogous to the behavior observed for copper foam electrodes discussed in Chapter 5. For a given nitrate concentration, increasing the recirculation flow rate significantly enhances FE_{NH_3} and the associated energy efficiency by increasing the convective contribution to mass transfer, thinning the effective diffusion layer, and stabilizing the local reaction environment at the catalyst–electrolyte interface. However, even at the highest flow rate, the Faradaic efficiency at a nitrate concentration of 4000 mg L^{-1} would remain limited by the lower bulk nitrate concentration. This observation underscores that hydrodynamic optimization and an increase in bulk nitrate concentration act as complementary control parameters rather than interchangeable levers for overcoming mass-transport limitations in the CCM architecture.

6.3.3. Pulsed Electrolysis and Local Microenvironment

Pulsed electrolysis (PE) aims to exploit the different time scales of reaction kinetics and mass transfer to periodically regenerate the concentration and bubble distribution in the vicinity of the electrode. The underlying hypothesis is that, during short zero-current intervals t_{off}, nitrate can diffuse back into the depleted boundary layer and gas bubbles can detach from the surface, so that the subsequent active interval t_{on} proceeds under more favorable local conditions than in continuous mode at the same average current density. In this picture, pulsed operation should mitigate local nitrate depletion and bubble coverage and thereby increase FE_{NH_3} relative to

continuous operation at identical average current density.

In this study, symmetric current pulses with $t_{on} = t_{off}$ = 0.1 s were applied. During t_{on}, the current density was doubled compared to the corresponding CC experiment (for example 200 mA cm^{-2} instead of 100 mA cm^{-2}), such that the time-averaged current density remained identical. Experiments were performed at average current densities of 50 mA cm^{-2}, 100 mA cm^{-2}, and 150 mA cm^{-2}.

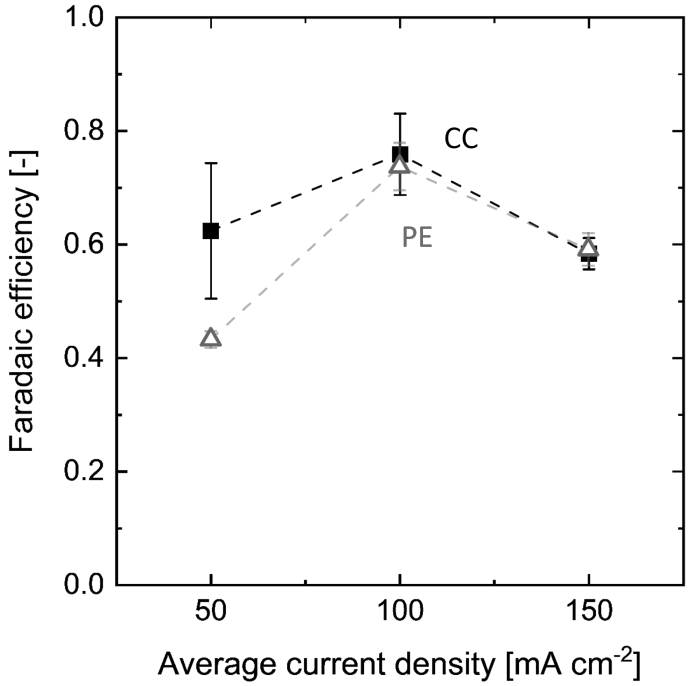

Figure 6.3.: Faradaic efficiency for NH_4^+ as a function of average current density for constant-current (CC) experiments (■) and pulsed electrolysis (PE, △); $t_{on} = t_{off}$ = 0.1 s. Starting electrolyte $c_0(NO_3^-) = 12\,000$ mg L^{-1} in 0.1 M H_2SO_4; recirculation flow rate: 220 mL min^{-1}.

At an average current density of 50 mA cm^{-2}, the CC experiment achieved $FE_{NH_3} \approx 62$ %, whereas the pulsed operation yielded only approximately 43 %. In this case, however, the CCM used for the pulsed experiment had a noticeably lower catalyst loading of about 0.8 mg cm^{-2} compared to up to 1.6 mg cm^{-2} in the CC experiment. A direct attribution of the lower FE_{NH_3} to the pulse protocol alone is therefore not justified as the experiments at this current density did not achieve stable operating conditions due to the low conversion and associated analytical challenges.

At average current densities of 100 mA cm^{-2} and 150 mA cm^{-2}, where the catalyst loading was identical for CC and pulsed operation, the Faradaic efficiencies were nearly indistinguishable: $FE_{NH_3} \approx 76$ % versus 74 % at 100 mA cm^{-2}, and $FE_{NH_3} \approx 59$ % in both cases at 150 mA cm^{-2}. Under these conditions, no systematic improvement of FE_{NH_3} can be attributed to pulsed operation when compared at the same average current density.

The absence of a clear macroscopic benefit from pulsed electrolysis at identical average current density suggests that the applied pulse parameters do not sufficiently decouple the characteristic time scales of reaction and mass transfer. The characteristic diffusion time over a given diffusion-layer thickness was introduced in Equation (2.22) and yields values on the order of 0.017 to 1.7 s for diffusion lengths in the range of 10 to 100 µm and the diffusion coefficient of nitrate in water. For larger effective diffusion-layer thicknesses, for example when transport through the ionomer and porous support is included and thicknesses above 600 µm are considered, the corresponding diffusion times extend into the regime of seconds up to minutes. The chosen t_{off} = 0.1 s is thus comparable only to the lower bound of these characteristic times and is likely insufficient to substantially relax the nitrate concentration gradient in the extended diffusion path of the CCM, particularly at higher current densities where nitrate is rapidly consumed during t_{on}. In addition, the elevated current during t_{on} may intensify bubble formation and local ohmic heating, partially compensating any replenishment of nitrate during t_{off}.

Besides the duration of t_{off}, the choice of t_{on} also affects the local microenvironment. Very short t_{on} intervals predominantly charge the electrochemical double layer and only weakly deplete nitrate, so that a substantial fraction of the pulse charge is non-faradaic and the intended coupling between reaction and mass transfer is weakened. Moderately extended t_{on} intervals beyond the double-layer charging time, combined with significantly longer t_{off} periods, would allow each pulse to reach a quasi-steady Faradaic regime in which nitrate is measurably depleted and the subsequent relaxation during t_{off} becomes more effective.

A relevant observation is that, at 100 mA cm^{-2} average current density,

the PE protocol maintains FE_{NH_3} close to the value of the CC experiment, although the instantaneous current density during t_{on} is doubled. Continuous operation at such elevated current densities typically leads to a pronounced decrease in FE_{NH_3} due to stronger nitrate depletion and enhanced HER. The fact that FE_{NH_3} remains high in the pulsed case indicates that the local microenvironment during t_{on} is partially stabilized by the intermittent relaxation phases and that pulsed operation mitigates, but does not eliminate, mass-transport limitations. Nevertheless, when evaluated at identical average current density, pulsed operation does not provide a net gain in FE_{NH_3} or productivity compared to continuous galvanostatic operation within the investigated parameter space.

Thus, the specific implementation of pulsed electrolysis in this work does not confirm the general hypothesis that dynamic operation inherently improves FE_{NH_3} in the CCM configuration. The results suggest that meaningful benefits would require significantly longer t_{off} intervals, reduced peak current densities, or more sophisticated pulse shapes that explicitly account for the characteristic diffusion times and bubble dynamics of the system. At the same time, the partial stabilization of FE_{NH_3} at doubled instantaneous current density indicates that mass-transport effects are not the sole limitation. The data is consistent with the interpretation that proton supply within the catalyst layer remains constrained by the ionomer phase, so that the local proton activity and nitrate accessibility cannot be simultaneously optimized by pulsing alone. This motivates the subsequent investigation of the binder chemistry, where replacing the cation-exchange binder by an anion-conducting ionomer is hypothesized to reduce nitrate exclusion in the ionomer phase and to further decouple proton transport from nitrate mass transport in the CCM architecture.

6.3.4. Influence of Ionomer Binder

The ionomer binder in the catalyst layer not only provides mechanical cohesion and ionic conductivity but also defines the local electrostatic and chemical microenvironment of the active sites. In Nafion™-based CCMs,

sulfonic acid groups confer high proton conductivity and impart a negative fixed charge to the ionomer phase, which promotes the uptake of cations and induces Donnan exclusion of anions such as NO_3^-. Based on this electrostatic picture, replacing Nafion™ by an anion-conducting ionomer such as Sustainion®, bearing quaternary ammonium groups and a positive fixed charge, can be expected to facilitate NO_3^- transport through the ionomer phase and increase the nitrate flux to the copper surface. Hence, it was hypothesized that Sustainion®-based CCMs should exhibit equal or higher FE_{NH_3} than Nafion™-based CCMs under comparable operating conditions.

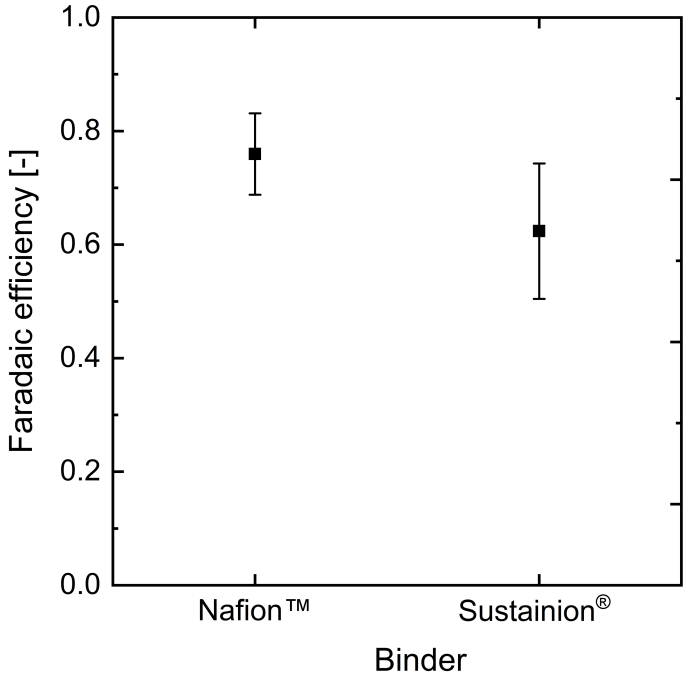

Figure 6.4.: Faradaic efficiency for NH_4^+ as a function of the ionomer binder used in the catalyst layer. Starting electrolyte $c_0(NO_3^-) = 12\,000\,\mathrm{mg\,L^{-1}}$ in 0.1 M H_2SO_4; current density: $50\,\mathrm{mA\,cm^{-2}}$; recirculation flow rate: $220\,\mathrm{mL\,min^{-1}}$.

To test this hypothesis, CCMs were prepared with identical copper loading and ionomer-to-carbon ratio in the ink, using either Nafion™ or Sustainion® as binder. Experiments were conducted at a current density of $50\,\mathrm{mA\,cm^{-2}}$ in a catholyte of $0.05\,\mathrm{mol\,L^{-1}}$ H_2SO_4 containing $12\,000\,\mathrm{mg\,L^{-1}}$ nitrate supplied as HNO_3. Under these conditions, the Nafion™-based

CCM yielded $FE_{NH_3} \approx 77$ %, whereas the Sustainion®-based CCM reached only about 62 %. In both cases, the nitrogen balances were close to 100 %, with negligible nitrite formation, indicating that ammonium and residual nitrate remained the dominant nitrogen-containing species.

This outcome contradicts the initial sub-hypothesis and suggests that, in the present CCM system, proton availability and local acidity are more critical performance determinants than facilitated nitrate transport through the ionomer phase. In the Nafion™-based CCM, the sulfonic acid groups establish a strongly acidic environment within the catalyst layer and effectively couple the proton activity at the membrane side to the electrolyte-facing side of the copper layer. This minimizes internal pH gradients and lowers the barriers for proton-coupled elementary steps in the eNO_3RR sequence. In contrast, the Sustainion®-based layer, when combined with an underlying CEM, forms a bipolar interface in which cation- and anion-conducting domains are in direct contact. The resulting acid–base neutralization and ion partitioning effects tend to establish a locally less acidic microenvironment at the copper surface, which can hinder protonation steps in the eNO_3RR pathway and favor the HER, even if the nominal nitrate permeability of the ionomer phase is higher.

The absence of detectable nitrite and the comparable ammonia production rates indicate that the binder change does not induce a qualitatively different reaction pathway with increased accumulation of intermediates, but rather modifies the relative rates of eNO_3RR and HER by changing the local proton activity and electric field distribution within the catalyst layer. The refined hypothesis emerging from these observations is that, for eNO_3RR on CCMs, a proton-conducting, strongly acidic ionomer such as Nafion™ is beneficial, even if it may partially repel nitrate ions electrostatically. The critical design variable is therefore the balance between proton conduction and nitrate mass transport, rather than solely the sign of the ionomer's fixed charge. In combination with the pulsed electrolysis results, this supports the interpretation that improving nitrate access alone is insufficient to overcome the intrinsic limitations of proton supply in the current CCM architecture and that binder selection must primarily ensure

a favorable acidic microenvironment for the desired reaction sequence.

6.3.5. Operation without Supporting Electrolyte

A central motivation for the zero-gap electrolysis of NO_3^- is the treatment of nitrate-contaminated wastewaters, where the addition of supporting electrolyte is undesirable and nitrate itself represents the target pollutant. In such streams, nitrate and protons must act simultaneously as reactants and charge carriers. Previous experiments with porous copper foam electrodes at low electrolyte conductivity have shown that, under these conditions, only a fraction of the geometric foam area remains electrochemically active due to extended current paths and limited proton supply. The CCM architecture was therefore proposed as an alternative concept, in which a geometrically well-defined catalyst layer is in direct contact with a CEM. It was hypothesized that the locally acidic microenvironment of the Nafion™-based CCM would maintain reasonable FE_{NH_3} at low ionic strength by ensuring efficient proton delivery from the CEM, even when the bulk catholyte contains nitrate as essentially the only ionic species.

To test this hypothesis, experiments were conducted with catholytes containing 4000 mg L^{-1} nitrate, supplied solely as HNO_3, without additional supporting salt (Figure 6.5). The anolyte remained 0.1 mol L^{-1} H_2SO_4. At average current densities of 50 mA cm^{-2} and 100 mA cm^{-2}, the Faradaic efficiency towards ammonia decreased to approximately 30 % in both cases, significantly lower than the corresponding values obtained in the presence of supporting electrolyte at the same nitrate concentration. The cell voltage increased compared to the acid-supported cases, and GEIS measurements revealed a substantially higher high-frequency resistance, consistent with the reduced ionic conductivity of the catholyte.

In the absence of supporting electrolyte, the electric field in the catholyte is sustained predominantly by the reactive ions NO_3^- and H^+. As NO_3^- is reduced at the cathode, its local concentration near the CCM decreases and so does the local conductivity[Czer2025]. This coupling between reaction and charge transport leads to pronounced field inhomogeneities and

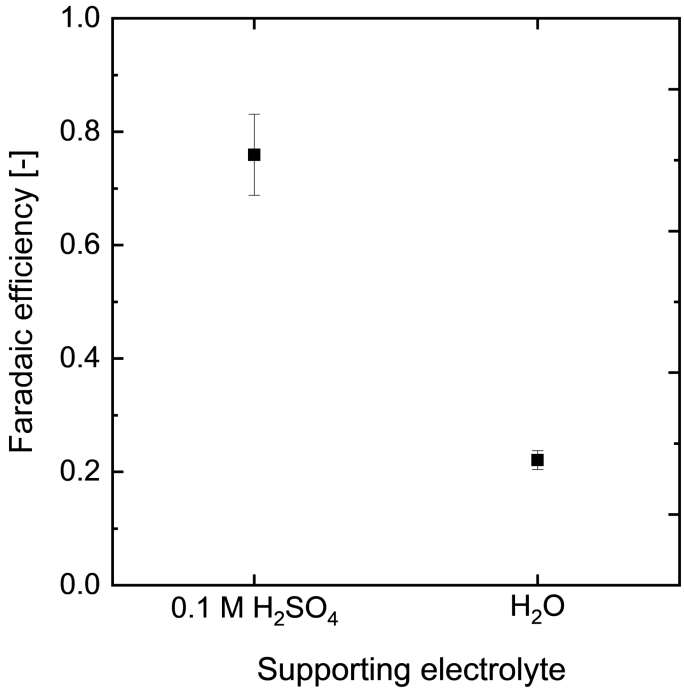

Figure 6.5.: Faradaic efficiency for NH_4^+ as a function of the supporting electrolyte. Starting electrolyte $c_0(NO_3^-) = 12\,000\,\text{mg}\,\text{L}^{-1}$ in 0.1 M H_2SO_4 or ultrapure water; current density: $100\,\text{mA}\,\text{cm}^{-2}$; recirculation flow rate: $220\,\text{mL}\,\text{min}^{-1}$.

spatially varying current densities across the CCM. Regions with initially higher conductivity carry more current, but experience accelerated nitrate depletion, which further amplifies the inhomogeneity and promotes the development of locally transport-limited zones. At the same time, the reduced ionic strength increases the Debye length and alters interfacial properties such as double-layer structure, wetting behavior, and bubble nucleation and detachment. Experimentally, gas bubbles were observed to adhere more strongly to the catalyst surface, intermittently blocking active sites and further reducing the effective area available for eNO_3RR.

The elevated high-frequency resistance obtained from GEIS and the increased noise in the mid-frequency range of the impedance spectra corroborate this picture. The high-frequency response reflects the increased ohmic resistance of the catholyte, while the mid-frequency fluctuations indicate dynamic changes in local conductivity and interfacial area driven by gas evolution and transient nitrate depletion. These coupled effects of re-

active charge transport, field focusing, and bubble coverage collectively limit the achievable FE_{NH_3} and ammonia production rate, despite the presence of a strongly acidic CCM microenvironment and an efficient proton supply from the CEM.

These observations do not confirm the hypothesis that a CCM on a CEM is sufficient to maintain high FE_{NH_3} at low ionic strength and low nitrate concentration. While proton delivery from the membrane effectively prevents the local pH from becoming alkaline, the lack of inert charge carriers causes severe conductivity and mass-transport limitations because nitrate itself must carry the current and is simultaneously consumed as reactant. In this regime, the planar CCM configuration does not offer a clear advantage over porous electrodes; its lower geometric area and the additional ionomer diffusion layer can even exacerbate the challenges posed by low ionic strength. For practical wastewater applications without electrolyte addition, alternative strategies such as larger-area porous electrodes with optimized flow and current distribution, segmented electrodes with local conductivity enhancement, or hybrid processes combining electrochemical and biological denitrification are likely more promising than relying solely on planar CCM architectures.

6.4. Conclusion

This chapter investigated electrochemical nitrate reduction to ammonia on copper-based catalyst-coated membranes in a zero-gap flow cell, with emphasis on the role of the ionomer–membrane microenvironment under conditions relevant to nitrate-containing wastewaters. The working hypothesis was that a CCM on a CEM can restore high local proton availability and thereby improve FE_{NH_3} at moderate nitrate concentrations, but becomes mass-transport-limited at low concentrations and low ionic strength. This hypothesis was systematically tested and refined by varying nitrate concentration, hydrodynamics, dynamic operation, ionomer binder chemistry, and supporting electrolyte.

At fixed current density, increasing the nitrate concentration from 4000 mg L^{-1} to 12 000 mg L^{-1} led to a quasi-linear increase in FE_{NH_3} from about 45 % to roughly 76 % and in ammonia production rate from approximately 0.21 mmol h^{-1} cm^{-2} to 0.35 mmol h^{-1} cm^{-2}. In parallel, raising the catholyte recirculation flow from 80 mL min^{-1} to 220 mL min^{-1} significantly enhanced FE_{NH_3} by about 66 % and reduced the cell voltage about 15 %. Together, these results highlight the central role of mass transfer and hydrodynamics in the CCM architecture and confirm that, once proton delivery from the CEM and the ionomer is ensured, nitrate mass transport through the diffusion layer and the ionomer becomes the dominant limitation. The CCM configuration is therefore well suited for concentrated nitrate streams and conditions where supporting electrolyte can be supplied, achieving FE_{NH_3} up to about 76 % at 100 mA cm^{-2} with moderate cell voltages.

Pulsed electrolysis with short, symmetrical current pulses did not yield measurable improvements over continuous galvanostatic operation within the explored parameter space. The selected pulse period of 0.2 s per cycle is comparable to or shorter than the characteristic diffusion times of nitrate in the extended transport path of the CCM and the time scales of bubble evolution, so that the intended concentration-reset effect could not be fully realized. At identical average current density, FE_{NH_3} under pulsed condi-

tions remained similar to that under continuous operation, even though the instantaneous current density during the active phase was doubled. This indicates a partial stabilization of the local microenvironment by the intermittent relaxation phases, but does not translate into a net gain in FE_{NH_3} or productivity under the chosen conditions. For pulsed operation to be beneficial in CCM-based eNO_3RR, longer relaxation times, reduced peak currents, and tailored pulse shapes that explicitly account for diffusion and bubble dynamics would be required.

The comparison between Nafion™- and Sustainion®-based CCMs demonstrated that a strongly acidic, proton-conducting ionomer is advantageous under the present conditions. Contrary to the initial expectation that an anion-conducting binder would facilitate nitrate access and thus improve performance, the Sustainion®-based CCM exhibited a slight but insignificant lower FE_{NH_3} than its Nafion™-based counterpart at comparable loading and operating conditions. This indicates that, in the regime studied here, proton availability and a homogeneous acidic microenvironment within the catalyst layer are more critical than electrostatic facilitation of nitrate transport through the ionomer. The results support the interpretation that the ionomer must primarily ensure efficient proton conduction and stabilization of a favorable local pH, while increased nitrate permeability alone does not compensate for a less acidic microenvironment.

Operation without supporting electrolyte revealed a fundamental limitation of the CCM concept for low-ionic-strength wastewaters. When nitrate and protons act simultaneously as reactants and charge carriers, the consumption of NO_3^- near the cathode leads to strong conductivity gradients, field inhomogeneities, and enhanced bubble-induced blockage of active sites. Under these conditions, FE_{NH_3} dropped to about 30 %, despite the presence of a strongly acidic CCM and direct proton supply from the CEM. The planar geometry and the additional ionomer transport layer do not compensate for the lack of inert charge carriers; instead, they aggravate the transport limitations because nitrate becomes locally scarce precisely in those regions where it must carry the current. This refined view shows that, in the electrolyte-free regime, proton availability is not

the primary bottleneck, while nitrate transport and reactive charge-carrier limitations become decisive.

The CCM architecture thus introduces new transport constraints. Compared to three-dimensional foams, the geometric surface area of a planar CCM is smaller, the electrolyte flow field is less effective at promoting convective mixing immediately at the catalyst interface, and the ionomer binder introduces an additional porous transport layer for nitrate ions. At low nitrate concentrations and low ionic strength, these effects reduce nitrate flux to the catalyst and promote a proton-rich, nitrate-poor microenvironment that again favors the HER. From a reactor-design perspective, it therefore remains uncertain whether a CCM-based zero-gap configuration is advantageous for dilute nitrate streams, as encountered in treated wastewaters, or whether porous foams with optimized hydrodynamics and current distribution remain superior in this regime.

7.

Conclusion and Perspectives

This dissertation examined electrochemical pathways for sustainable NH_3 production from nitrogen species with a focus on the electrochemical nitrate reduction reaction (eNO_3RR) in flow-cell architectures compatible with nitrate-containing wastewaters. This chapter answers the research questions raised in Chapter 1 by summarizing the key findings from each chapter and their key contributions.

By combining Metal-Organic-Framework (MOF)-derived model catalysts, copper-based porous electrodes, ion-exchange and bipolar membranes, and hydrodynamically controlled reactors, the work linked catalyst structure, membrane configuration, local microenvironment, and macroscopic transport to faradaic efficiency (FE), energy efficiency, and process relevance in a circular nitrogen economy.

The first central result is the consistent adherence to the protocol for the electrochemical nitrogen reduction reaction (eNRR), whereby nitrogen-free catalysts were synthesized and tested in the form of MOF-derived carbons. MIL-100(Fe) precursors were synthesized and pyrolyzed over a wide temperature range. Their phase evolution, graphitization, and porosity were characterized using Raman spectroscopy, XRD and gas sorption. Although high-temperature treatment produced conductive iron carbide and metallic phases and improved capacitive behavior, rigorous $^{15}N_2$/Ar testing following state-of-the-art protocols revealed no N_2-to-NH_3 activity above the established red-light detection limit. The residual apparent NH_3 formation could be fully rationalized by background contamination and

nitrogen-containing impurities. This negative result supports the emerging consensus that, under realistic aqueous conditions, most reported eNRR activities on similar materials are artifacts and that nitrate-based electrochemical routes currently offer a far more robust basis for sustainable NH_3 synthesis.

A second key finding is the identification of transport- and membrane-controlled operating regimes in copper-foam-based eNO_3RR reactors. In divided flow cells with porous Cu foams, nitrate reduction to NH_3 was shown to be highly sensitive to membrane selection, nitrate concentration, and hydrodynamics. Bipolar membranes operated in inside-out mode effectively suppressed NO_3^- and NH_4^+ crossover and enabled high FEs toward NH_3, whereas cation- and anion-exchange membranes suffered from significant ammonium crossover or nitrate depletion and associated back-oxidation. Switching from batch to continuous feed-and-bleed operation enabled the steady-state mapping of partial current densities, cell voltages, and FEs as a function of recirculation flow and nitrate conversion. This revealed that an increase in NH_4^+ concentration raises cell resistance and exacerbates bipolar membrane (BPM) stress. This finding is in agreement with literature on ammonia poisoning of ionomers and cation exchange membranes (CEMs) [Urib2002; Hals2004; Hals2006]. By coupling electrochemical data with mass-transfer correlations, the work demonstrated that the onset of diffusion limitation and the balance between eNO_3RR and hydrogen evolution reaction HER can be related qualitatively to effective diffusion-layer thicknesses and Reynolds and Sherwood numbers in the porous electrode and flow channel.

A third major outcome is the refined assessment of copper-based catalyst-coated membranes (CCMs) in zero-gap cells as an alternative architecture for eNO_3RR. In these systems, an acidic ionomer on a cation-exchange membrane creates a proton-rich microenvironment at the catalyst layer that is partially decoupled from the bulk catholyte. Under concentrated nitrate feeds and with supporting electrolyte present, CCMs with Nafion® binders achieved FEs toward NH_3 up to approximately 76 % at 100 mA cm^{-2}, benefiting strongly from higher recirculation flows and high-

lighting the importance of balanced proton and nitrate supply within the ionomer-membrane domain. At the same time, operation in low-ionic-strength nitrate solutions without supporting electrolyte exposed a fundamental limitation: when nitrate and protons act as both reactants and charge carriers, their local depletion leads to steep conductivity gradients, field focusing, and bubble coverage that cannot be fully compensated by the planar CCM geometry, causing FEs toward NH_3 to drop despite a strongly acidic microenvironment. In this regime, three-dimensional porous electrodes with optimized flow fields may remain the more robust option.

Overall, the thesis moves electrochemical nitrate reduction on copper from a predominantly catalyst-centric half-reaction toward a process-relevant unit operation that can be embedded in realistic nitrogen-management and wastewater-treatment contexts. It demonstrates that high FEs and technologically relevant current densities can be achieved when catalyst structure, membrane configuration, nitrate concentration, ionic strength, and hydrodynamics are co-optimized and clarifies that up to now foam-based electrodes are preferred against zero-gap CCMs. These insights offer quantitative design principles, such as structures that improve mixing properties. These principles can guide the integration of eNO_3RR into distributed NH_3 production schemes and nitrate-removal processes.

A central challenge for future development is to retain high FEs and current densities under supporting-electrolyte-free or low-ionic-strength conditions, as encountered in many treated wastewaters and environmental streams. The present results show that, in such media, nitrate and protons themselves become the dominant charge carriers and their consumption near the cathode leads to strong conductivity gradients, local field intensification, and enhanced bubble coverage, which in turn promote HER and suppress eNO_3RR [Adam1971; Jans1978; Huan2016; Huan2017; Venn2019; Wang2023a; Rox2023; Huan2024a] Future work should therefore explore electrode architectures and flow fields that homogenize current distribution and convectively renew both reactants

and charge carriers, for example graded-porosity foams, interdigitated flow-through channels, or segmented current collectors with locally tailored current densities [Brow1994; Lang1989a; Lang1989b; Lang1990a; Lang1990b; Rox2023; Baes2025]. On the materials side, ionomers and membranes with high proton conductivity at low ionic strength and reduced uptake of NH_4^+ are needed to limit resistance growth and degradation without introducing additional supporting ions, building on insights from ammonia contamination studies in CEMs and ion-exchange membranes [Urib2002; Hals2004; Hals2006; Gome2018; Mitt2007; Huan2025; Skol2022; Sign2024; Wild2024; Joos2025; Salv2021].

A second important direction is the integration of eNO_3RR with upstream pretreatment by reverse osmosis (RO), electrodialysis (ED), or ion exchange. These processes can concentrate nitrate from raw wastewaters with NO_3^- levels below 10 mmol L^{-1} into brines on the order of 100-150 mmol L^{-1}, thereby increasing both nitrogen content and ionic strength by more than an order of magnitude [Abas2022; Guti2018; Garc2018; Mart2017; Huo2020]. The present work, together with recent ED and redox-electrode concepts, shows that such enriched feeds are beneficial for eNO_3RR, pushing the onset of mass-transport limitation to higher current densities, raising FEs toward NH_3, and lowering cell voltages [McEn2020; Kim2023; Guo2024; Chen2020; Chen2022b; Daiy2021; Fang2023; Hoan2024]. Future research should therefore address the process-level design and optimization of coupled RO/ED/ion-exchange-eNO_3RR flowsheets, including the role of co-ions such as Cl^- and SO_4^{2-} on catalyst stability and membrane performance, and evaluate techno-economic and life-cycle performance against biological and physico-chemical nitrate-removal benchmarks.[Mart2017; Garc2018; Wang2021; Guid2022; Gao2024; Simo2025]

A third promising line of work concerns continuous separation and recovery of the produced NH_3. In the systems studied here, NH_3 is mainly recovered from the liquid phase, while crossover and sorption in membranes and ionomers contribute to resistance increase and degradation [Urib2002; Hals2004; Hals2006; Gome2018; Skol2022; Bi2023; Sign2024; Wild2024;

Huan2025]. Gas diffusion electrodes (GDEs) or hollow-fiber architectures that promote NH_3 desorption into a gas phase, followed by acid scrubbing, could generate concentrated ammonium salt solutions suitable for direct fertilizer use and, in some cases, allow simultaneous anodic production of chlorine or other value-added oxidants [Venn2019; Salv2021; Gao2024; Baes2024]. Alternatively, coupling the catholyte loop to membrane contactors or air-stripping units, as already demonstrated for ammonia recovery from ion-exchange regenerant brines, offers a path to continuous NH_3 removal without major modification of the electrochemical cell [Huo2020; Guid2022]. Careful co-optimization of hydrodynamics and interfacial area in these separation steps with electrochemical operation will be essential to avoid new mass-transfer bottlenecks while maintaining high FEs and low cell voltages.

Beyond pure NH_3 production, the process window identified in this work suggests that deliberate partial nitrate conversion may be utilized to tailor fertilizer formulations. If approximately 50 % of the nitrate in a concentrated, charge-balanced stream is reduced to ammonium, the resulting solution approaches an equimolar NH_4^+/NO_3^- mixture, i.e., liquid ammonium nitrate (NH_4NO_3). Such a product is a widely used nitrogen fertilizer that combines fast-acting nitrate with more gradually assimilated ammonium and can be dosed directly into fertilization systems without additional neutralization or blending [Eris2008; Lim2021; vLang2021; Hoan2024]. Producing ammonium nitrate solutions on-site from preconcentrated nitrate streams at wastewater-treatment plants or agricultural drainage hubs would reduce transport and storage requirements, avoid safety issues associated with solid ammonium nitrate handling, and enable nitrogen formulations tuned to local soil conditions and crop demands [MacF2020; Smit2020; IREN2022; Guid2022; Guo2024; Gao2024]. Designing control strategies that stabilize operation at target nitrate conversions and product ratios, for instance by combining electrochemical feedback with inline analytics, represents an attractive topic for future research.

Finally, the electrochemical nitrate-to-ammonia concepts developed here open additional application spaces that merit exploration. High-

nitrate industrial effluents from fertilizer, explosives, mining, or metallurgical operations often already exhibit nitrate concentrations and ionic strengths within the favorable operating window identified for copper foams and CCMs [Mart2017; Garc2018; Daiy2021; Mari2024; Hoan2024; Duan2025]. In such settings, on-site eNO_3RR reactors could convert waste nitrate into reusable ammonium or ammonium nitrate solutions, closing local nitrogen loops and reducing dependence on centralized Haber-Bosch (HB) plants [Appl2011; Smit2020; IEA2021; IREN2022]. In decentralized contexts, modular eNO_3RR units coupled to renewable electricity and upstream ED or ion-exchange preconcentration could enable "power-to-fertilizer" schemes that simultaneously mitigate nitrate pollution and provide flexible demand-side management for power grids [McEn2020; Kim2023; Guo2024; Guid2022; Simo2025]. Pairing cathodic eNO_3RR with value-added anodic reactions, such as selective oxidation of organics or halide-to-halogen conversion, further offers the potential for paired electrosynthesis with improved overall atom and energy efficiency [Baes2024; Gao2024; Shen2025].

In summary, the present work establishes eNO_3RR on copper-based electrodes as a promising building block for low-carbon ammonia and ammonium nitrate production integrated with wastewater treatment. By clarifying the roles of catalyst structure, membrane selection, microenvironment, and hydrodynamics, it provides a mechanistic and engineering foundation on which future developments in materials, reactor design, and process integration can build. Realizing the full potential of these concepts will require close interaction between electrochemistry, membrane science, reaction engineering, and environmental systems analysis, but the pathways outlined here indicate that electrochemical nitrate-to-ammonia conversion can contribute meaningfully to a more circular and climate-compatible nitrogen economy.

A.
Figures

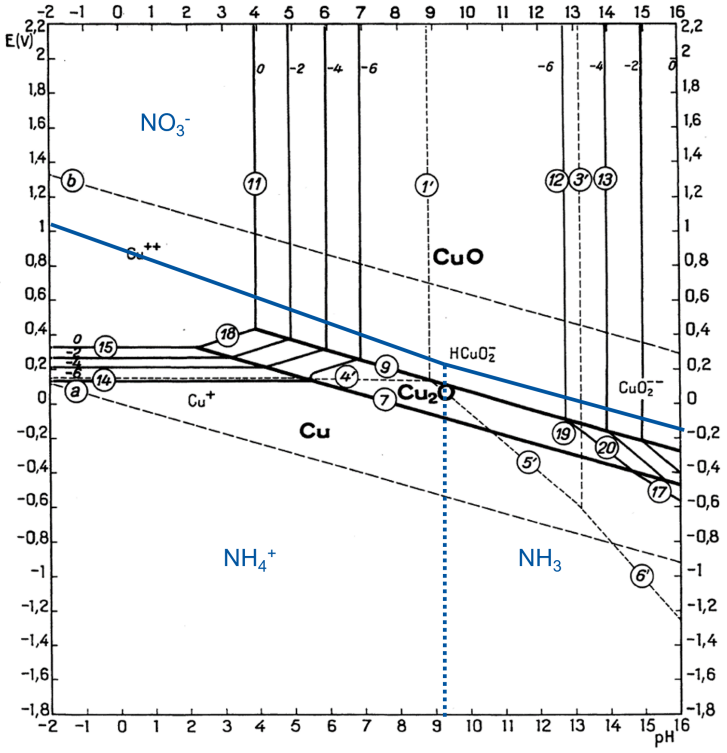

Figure A.1.: Pourbaix diagram of the nitrogen-water system at copper electrodes. Standard entropy and enthalpy for calculation (blue) obtained from NIST database. [Pour1974]

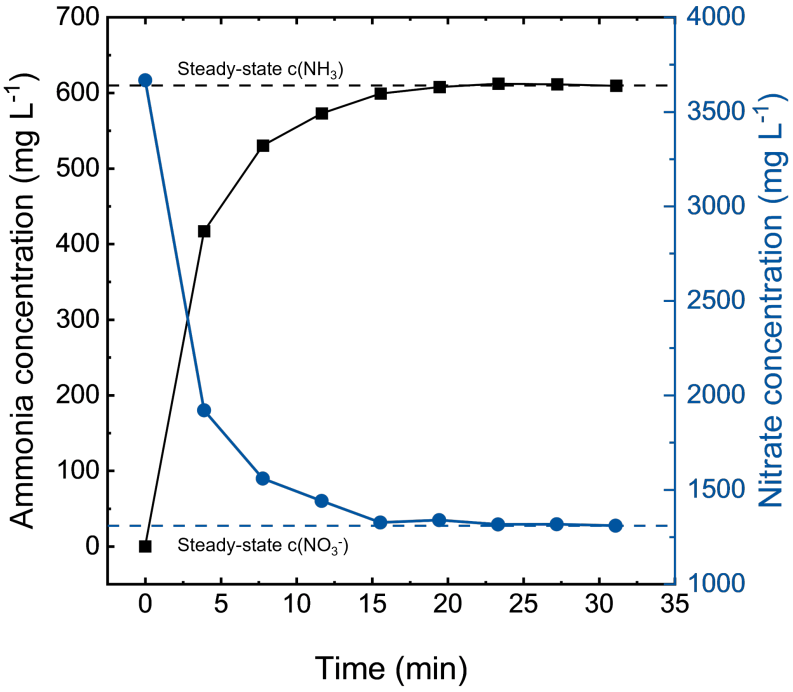

Figure A.2.: Evolution of ammonium and nitrate concentrations over time as an indicator of the cell's startup behavior. Steady-state conditions are typically reached after 20 min.

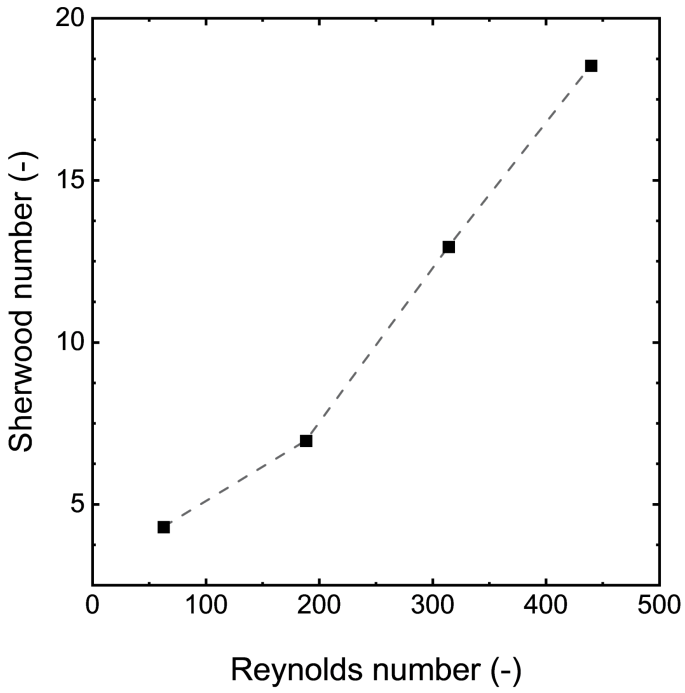

Figure A.3.: Evolution of the Sherwood number with increasing Reynolds number for interstitial and superficial flow in a channel.

Bibliography

[Abas2022] E. Abascal, L. Gómez-Coma, I. Ortiz, and A. Ortiz. “Global diagnosis of nitrate pollution in groundwater and review of removal technologies”. *Science of The Total Environment*, vol. 810. Mar. 2022. doi: 10.1016/j.scitotenv.2021.152233 (cit. on pp. 29, 134).

[Adam1971] E. Adam, J. Venczel, and E. Schalch. “Stofftransport bei der Elektrolyse mit Gasrührung”. *Chemie Ingenieur Technik*, vol. 43, no. 4. 1971. doi: 10.1002/cite.330430418 (cit. on pp. 94, 133).

[Agou2023] A. M. Agour, E. Elkersh, G. E. Khedr, H. G. El-Aqapa, and N. K. Allam. “Fe-Single-Atom Catalysts on Nitrogen-Doped Carbon Nanosheets for Electrochemical Conversion of Nitrogen to Ammonia”. *ACS Appl. Nano Mater.*, vol. 6, no. 17. Sep. 2023. doi: 10.1021/acsanm.3c02948 (cit. on p. 34).

[Ande2019] S. Z. Andersen et al. “A rigorous electrochemical ammonia synthesis protocol with quantitative isotope measurements”. *Nature*, vol. 570, no. 7762. Jun. 2019. doi: 10.1038/s41586-019-1260-x (cit. on pp. 4, 35, 38, 39, 50).

[Appl2011] M. Appl. “Ammonia, 2. Production Processes”, in: *Ullmann’s Encyclopedia of Industrial Chemistry*. Wiley-VCH, Ed., 1st ed., Wiley, Oct. 2011. isbn: 978-3-527-30385-4.doi: 10.1002/14356007.o02_o11 (cit. on pp. 1, 24, 136).

[Bae2007] S.-E. Bae, K. L. Stewart, and A. A. Gewirth. “Nitrate Adsorption and Reduction on Cu(100) in Acidic Solution”. *J. Am. Chem. Soc.*, vol. 129, no. 33. Aug. 2007. doi: 10.1021/ja071330n (cit. on pp. 58, 80).

[Baes2024] J. Baessler, N. Vollmert, J. Vehrenberg, M. Mineur, S. Schenke, L. Griesberg, P. M. Pineda, and R. Keller. “Reaction engineering for high yield electrosynthesis: Unraveling the impact of reaction conditions and conversion on methanol oxidation to formate”. *Chem. Eng. J.*, vol. 495. Sep. 2024. doi: 10.1016/j.cej.2024.153000 (cit. on pp. 83, 135, 136).

[Baes2025] J. Baessler, M. Wehner, M. Mohseni, J. Neumann, M. Wessling, and R. Keller. “Feed and Bleed Operating Mode for Electrochemical Flow Cells: Challenges, Solutions and Practical Insights”. *ChemElectroChem*, vol. 12, no. 12. Mar. 2025. doi: 10.1002/celc.202500034 (cit. on pp. 11, 18, 19, 82, 83, 86, 87, 134).

[Bard2001] A. J. Bard and L. R. Faulkner. *Electrochemical Methods: Fundamentals and Applications*. 2. edition. New York Weinheim: Wiley, 2001. isbn: 978-0-471-04372-0. (Cit. on pp. 9, 15, 16, 18).

[Barr2023] L. Barrera, R. Silcox, K. Giammalvo, E. Brower, E. Isip, and R. Bala Chandran. “Combined Effects of Concentration, pH, and Polycrystalline Copper Surfaces on Electrocatalytic Nitrate-to-Ammonia Activity and Selectivity”. *Am. Chem. Soc. Catal.*, vol. 13, no. 7. Apr. 2023. doi: 10.1021/acscatal.2c05136 (cit. on pp. 2, 79, 89).

[Bi2023] W. Bi, E. Gyenge, and D. P. Wilkinson. “Crossover, volatilization, and adsorption of ammonium ions in a proton-exchange membrane electrolyzer in relation to electrochemical ammonia production”. *Chemical Engineering Journal*, vol. 478. Dec. 2023. doi: 10.1016/j.cej.2023.147359 (cit. on p. 134).

[Blom2020] M. A. Blommaert, J. A. H. Verdonk, H. C. Blommaert, W. A. Smith, and D. A. Vermaas. “Reduced Ion Crossover in Bipolar Membrane Electrolysis via Increased Current Density, Molecular Size, and Valence”. *ACS Appl. Energy Mater.*, vol. 3, no. 6. Jun. 2020. doi: 10.1021/acsaem.0c00687 (cit. on p. 13).

[Blom2021] M. A. Blommaert, D. Aili, R. A. Tufa, Q. Li, W. A. Smith, and D. A. Vermaas. “Insights and Challenges for Applying Bipolar Membranes in Advanced Electrochemical Energy Systems”. *ACS Energy Lett.*, vol. 6, no. 7. Jul. 2021. doi: 10.1021/acsenergylett.1c00618 (cit. on p. 13).

[Boer2019] L. Boerner, *Industrial ammonia production emits more CO2 than any other chemical-making reaction. Chemists want to change that*, https://cen.acs.org/environment/green-chemistry/Industrial-ammonia-production-emits-CO2/97/i24, Jun. 2019. Accessed: Nov. 7, 2025 (cit. on p. 32).

[Bohn2003] M. Bohnet and F. Ullmann, Eds. *Ullmann's Encyclopedia of Industrial Chemistry*. 6., completely revised ed. Weinheim: Wiley-VCH, 2003. isbn: 978-3-527-30385-4. (Cit. on p. 25).

[Bopp2024] R. Boppella, M. Ahmadi, B. M. Arndt, D. R. Lustig, and M. Nazemi. "Pulsed Electrolysis in Membrane Electrode Assembly Architecture for Enhanced Electrochemical Nitrate Reduction Reaction to Ammonia". *ACS Catal.*, vol. 14, no. 23. Dec. 2024. doi: 10.1021/acscatal.4c05225 (cit. on pp. 4, 105).

[Brow1994] C. Brown, D. Pletcher, F. Walsh, J. Hammond, and D. Robinson. "Studies of three-dimensional electrodes in the FMO1-LC laboratory electrolyser". *J Appl Electrochem*, vol. 24, no. 2. Feb. 1994. doi: 10.1007/BF00247779 (cit. on pp. 4, 22, 23, 97, 134).

[Case2021] R. Casebolt, K. Levine, J. Suntivich, and T. Hanrath. "Pulse check: Potential opportunities in pulsed electrochemical CO2 reduction". *Joule*, vol. 5, no. 8. Aug. 2021. doi: 10.1016/j.joule.2021.05.014 (cit. on p. 4).

[Chen2015] K. Cheng, Z. Kou, J. Zhang, M. Jiang, H. Wu, L. Hu, X. Yang, M. Pan, and S. Mu. "Ultrathin carbon layer stabilized metal catalysts towards oxygen reduction". *J. Mater. Chem. A*, vol. 3, no. 26. Jun. 2015. doi: 10.1039/C5TA02386F (cit. on p. 48).

[Chen2020] G.-F. Chen, Y. Yuan, H. Jiang, S.-Y. Ren, L.-X. Ding, L. Ma, T. Wu, J. Lu, and H. Wang. "Electrochemical reduction of nitrate to ammonia via direct eight-electron transfer using a copper–molecular solid catalyst". *Nat Energy*, vol. 5, no. 8. Jul. 2020. doi: 10.1038/s41560-020-0654-1 (cit. on p. 134).

[Chen2022a] L.-F. Chen, A.-Y. Xie, Y.-Y. Lou, N. Tian, Z.-Y. Zhou, and S.-G. Sun. "Electrochemical synthesis of Tetrahexahedral Cu nanocrystals with high-index facets for efficient nitrate electroreduction". *J. Electroanal. Chem.*, vol. 907. Feb. 2022. doi: 10.1016/j.jelechem.2022.116022 (cit. on p. 80).

[Chen2022b] F.-Y. Chen, Z.-Y. Wu, S. Gupta, D. J. Rivera, S. V. Lambeets, S. Pecaut, J. Y. T. Kim, P. Zhu, Y. Z. Finfrock, D. M. Meira, G. King, G. Gao, W. Xu, D. A. Cullen, H. Zhou, Y. Han, D. E. Perea, C. L. Muhich, and H. Wang. "Efficient conversion of low-concentration nitrate sources into ammonia on a Ru-dispersed Cu nanowire electrocatalyst". *Nat. Nanotechnol.*, vol. 17, no. 7. Jul. 2022. doi: 10.1038/s41565-022-01121-4 (cit. on pp. 58, 80, 134).

[Chen2024a] F.-Y. Chen, A. Elgazzar, S. Pecaut, C. Qiu, Y. Feng, S. Ashokkumar, Z. Yu, C. Sellers, S. Hao, P. Zhu, and H. Wang. "Electrochemical nitrate reduction to ammonia with cation shuttling in a solid electrolyte reactor". *Nat. Catal.*. Aug. 2024. doi: 10.1038/s41929-024-01200-w (cit. on pp. 79, 105).

[Chen2024b] H. Chen, Z. Zhang, Y. Li, L. Yu, F. Chen, and L. Li. "Conductive polymer protection strategy to promote electrochemical nitrate reduction to ammonia in highly acidic condition over Cu-based catalyst". *Chem. Eng. J.*, vol. 481. Feb. 2024. doi: 10.1016/j.cej.2024.148596 (cit. on p. 90).

[Choi2020] J. Choi, B. H. R. Suryanto, D. Wang, H.-L. Du, R. Y. Hodgetts, F. M. Ferrero Vallana, D. R. MacFarlane, and A. N. Simonov. "Identification and elimination of false positives in electrochemical nitrogen reduction studies". *Nat. Commun.*, vol. 11, no. 1. Nov. 2020. doi: 10.1038/s41467-020-19130-z (cit. on pp. 4, 35, 52, 80).

[Cost2025] G. F. Costa, M. E. G. Winkler, M. R. Pinto, F. H. B. Lima, and R. Nagao. "Effect of pH on the Electrochemical Reduction of Nitrate on Metallic Copper". *Chem. Cat. Chem.*, vol. n/a, no. n/a. Sep. 2025. doi: 10.1002/cctc.202501022 (cit. on p. 89).

[Czer2025] S. Czerny-Holownia, H. R. Boyer, A. J. King, V. Y. Yang, J. Guo, M. J. Liu, J. C. Bui, W. A. Tarpeh, and E. W. Lees. "How the electric double layer impacts nitrate reduction to ammonia". *EES Catal.*. Jul. 2025. doi: 10.1039/D5EY00217F (cit. on pp. 4, 124).

[Daiy2021] R. Daiyan, T. Tran-Phu, P. Kumar, K. Iputera, Z. Tong, J. Leverett, M. H. A. Khan, A. A. Esmailpour, A. Jalili, M. Lim, A. Tricoli, R.-S. Liu, X. Lu, E. Lovell, and R. Amal. "Nitrate reduction to ammonium: From CuO defect engineering to waste NOx-to-NH3 eco-

nomic feasibility". *Energy Environ. Sci.*, vol. 14, no. 6. Jun. 2021. doi: 10.1039/D1EE00594D (cit. on pp. 58, 80, 134, 136).

[Dort2013] M. Dortsiou, Ioannis Katsounaros, Christos Polatides, and G. and Kyriacou. "Influence of the electrode and the pH on the rate and the product distribution of the electrochemical removal of nitrate". *Environ. Technol.*, vol. 34, no. 3. Feb. 2013. doi: 10.1080/09593330.2012.696722 (cit. on p. 89).

[Drio2016] E. Drioli and L. Giorno, Eds. *Encyclopedia of Membranes*. Berlin, Heidelberg: Springer Berlin Heidelberg, 2016. isbn: 978-3-662-44323-1.doi: 10.1007/978-3-662-44324-8 (cit. on p. 12).

[Du2022] H.-L. Du, M. Chatti, R. Y. Hodgetts, P. V. Cherepanov, C. K. Nguyen, K. Matuszek, D. R. MacFarlane, and A. N. Simonov. "Electroreduction of nitrogen with almost 100% current-to-ammonia efficiency". *Nature*, vol. 609, no. 7928. Sep. 2022. doi: 10.1038/s41586-022-05108-y (cit. on p. 4).

[Duan2025] W. Duan, Y. Chen, Y. Zhu, L. Tian, W. Zheng, H. Fu, J.-L. Chen, Y.-J. Lin, J. C.-H. Lam, Y. Lei, and C. Feng. "Synergistic effects of Co single atoms and Co nanoparticles for electrocatalytic nitrate-to-ammonium conversion in strongly acidic wastewater". *App. Cat. B Environ. Eng.*, vol. 363. Apr. 2025. doi: 10.1016/j.apcatb.2024.124812 (cit. on p. 136).

[dVooy2000] A. C. A. de Vooys, R. A. van Santen, and J. A. R. van Veen. "Electrocatalytic reduction of NO3- on palladium/copper electrodes". *J. Mol. Cat. A Chem.*, vol. 154, no. 1. Mar. 2000. doi: 10.1016/S1381-1169(99)00375-1 (cit. on pp. 90, 94).

[El-S2023] M. El-Shafie. "Hydrogen production by water electrolysis technologies: A review". *Results in Engineering*, vol. 20. Dec. 2023. doi: 10.1016/j.rineng.2023.101426 (cit. on p. 26).

[Eris2008] J. W. Erisman, M. A. Sutton, J. Galloway, Z. Klimont, and W. Winiwarter. "How a century of ammonia synthesis changed the world". *Nature Geosci*, vol. 1, no. 10. Oct. 2008. doi: 10.1038/ngeo325 (cit. on pp. 1, 24, 135).

[Fan2022a] K. Fan, W. Xie, J. Li, Y. Sun, P. Xu, Y. Tang, Z. Li, and M. Shao. “Active hydrogen boosts electrochemical nitrate reduction to ammonia”. *Nat. Commun.*, vol. 13, no. 1. Dec. 2022. doi: 10.1038/s41467-022-35664-w (cit. on pp. 58, 80).

[Fan2022b] L. Fan, Q. Yu, J. Chen, U. Khan, X. Wang, and J. Gao. “Achievements and Perspectives in Metal–Organic Framework-Based Materials for Photocatalytic Nitrogen Reduction”. *Catalysts*, vol. 12, no. 9. Sep. 2022. doi: 10.3390/catal12091005 (cit. on p. 34).

[Fang2023] J.-Y. Fang, J.-L. Fan, S.-B. Liu, S.-P. Sun, and Y.-Y. Lou. “Copper-Based Electrocatalysts for Nitrate Reduction to Ammonia”. *Mater.*, vol. 16, no. 11. Jan. 2023. doi: 10.3390/ma16114000 (cit. on pp. 58, 80, 134).

[Ferr2000] A. C. Ferrari and J. Robertson. “Interpretation of Raman spectra of disordered and amorphous carbon”. *Phys. Rev. B*, vol. 61, no. 20. May 2000. doi: 10.1103/PhysRevB.61.14095 (cit. on pp. 49, 50).

[Gao2024] J. Gao, Q. Ma, Z. Wang, B. E. Rittmann, and W. Zhang. “Direct electrosynthesis and separation of ammonia and chlorine from waste streams via a stacked membrane-free electrolyzer”. *Nat. Commun.*, vol. 15, no. 1. Sep. 2024. doi: 10.1038/s41467-024-52830-4 (cit. on pp. 4, 80, 81, 134–136).

[Garc2018] S. Garcia-Segura, M. Lanzarini-Lopes, K. Hristovski, and P. Westerhoff. “Electrocatalytic reduction of nitrate: Fundamentals to full-scale water treatment applications”. *Applied Catalysis B: Environmental*, vol. 236. Nov. 2018. doi: 10.1016/j.apcatb.2018.05.041 (cit. on pp. 71, 134, 136).

[Gome2018] Y. A. Gomez, A. Oyarce, G. Lindbergh, and C. Lagergren. “Ammonia Contamination of a Proton Exchange Membrane Fuel Cell”. *J. Electrochem. Soc.*, vol. 165, no. 3. Mar. 2018. doi: 10.1149/2.0761803jes (cit. on p. 134).

[Guan2024] Y. Guan, J. Kümper, S. D. Mürtz, S. Kumari, P. J. C. Hausoul, R. Palkovits, and P. Sautet. “Origin of copper dissolution under electrocatalytic reduction conditions involving amines”. *Chem. Sci.*, vol. 15, no. 35. 2024. doi: 10.1039/D4SC01944J (cit. on p. 90).

[Guid2022] S. Guida, L. Van Peteghem, B. Luqmani, M. Sakarika, A. McLeod, E. J. McAdam, B. Jefferson, K. Rabaey, and A. Soares. “Ammonia recovery from brines originating from a municipal wastewater ion exchange process and valorization of recovered nitrogen into microbial protein”. *Chem. Eng. J.*, vol. 427. Jan. 2022. doi: 10.1016/j.cej.2021.130896 (cit. on pp. 2, 79, 134–136).

[Guo2023] J. Guo, P. Brimley, M. J. Liu, E. R. Corson, C. Muñoz, W. A. Smith, and W. A. Tarpeh. “Mass Transport Modifies the Interfacial Electrolyte to Influence Electrochemical Nitrate Reduction”. *J. Am. Chem. Soc. Sustain. Chem. Eng.*, vol. 11, no. 20. May 2023. doi: 10.1021/acssuschemeng.3c01057 (cit. on p. 89).

[Guo2024] J. Guo, M. J. Liu, C. Laguna, D. M. Miller, K. S. Williams, B. D. Clark, C. Muñoz, S. J. Blair, A. C. Nielander, T. F. Jaramillo, and W. A. Tarpeh. “Electrodialysis and nitrate reduction (EDNR) to enable distributed ammonia manufacturing from wastewaters”. *Energy Environ. Sci.*, vol. 17, no. 22. Nov. 2024. doi: 10.1039/D4EE03002H (cit. on pp. 3, 30, 79, 134–136).

[Guti2018] M. Gutiérrez, R. N. Biagioni, M. T. Alarcón-Herrera, and B. A. Rivas-Lucero. “An overview of nitrate sources and operating processes in arid and semiarid aquifer systems”. *Sci. Total Environ.*, vol. 624. May 2018. doi: 10.1016/j.scitotenv.2017.12.252 (cit. on pp. 2, 79, 134).

[Hals2004] R. Halseid, P. J. S. Vie, and R. Tunold. “Influence of Ammonium on Conductivity and Water Content of Nafion 117 Membranes”. *J. Electrochem. Soc.*, vol. 151, no. 3. Feb. 2004. doi: 10.1149/1.1641035 (cit. on pp. 93, 132, 134).

[Hals2006] R. Halseid, P. J. S. Vie, and R. Tunold. “Effect of ammonia on the performance of polymer electrolyte membrane fuel cells”. *J. Power Source*, Selected Papers from the Ninth Ulm Electrochemical Days, vol. 154, no. 2. Mar. 2006. doi: 10.1016/j.jpowsour.2005.10.011 (cit. on pp. 93, 132, 134).

[Hao2019] Y.-C. Hao, Y. Guo, L.-W. Chen, M. Shu, X.-Y. Wang, T.-A. Bu, W.-Y. Gao, N. Zhang, X. Su, X. Feng, J.-W. Zhou, B. Wang, C.-W. Hu, A.-X. Yin, R. Si, Y.-W. Zhang, and C.-H. Yan. “Promoting nitrogen electroreduction to ammonia with bismuth nanocrystals and

potassium cations in water". *Nat Catal*, vol. 2, no. 5. May 2019. doi: 10.1038/s41929-019-0241-7 (cit. on p. 4).

[Hayn2017] W. M. Haynes, D. R. Lide, and T. J. Bruno, Eds. *CRC Handbook of Chemistry and Physics: A Ready-Reference Book of Chemical and Physical Data*. 97th edition. Boca Raton: CRC Press, 2017. isbn: 978-1-4987-5429-3. (Cit. on p. 24).

[He2022] H. He, H.-M. Wen, H.-K. Li, and H.-W. Zhang. "Recent advances in metal–organic frameworks and their derivatives for electrocatalytic nitrogen reduction to ammonia". *Coordination Chemistry Reviews*, vol. 471. Nov. 2022. doi: 10.1016/j.ccr.2022.214761 (cit. on pp. 3, 33, 34).

[Hoan2024] N. Hoang Truong, J.-S. Kim, J. Lim, and H. Shin. "Electrochemical reduction of nitrate to Ammonia: Recent progress and future directions". *Chem. Eng. J.*, vol. 495. Sep. 2024. doi: 10.1016/j.cej.2024.153108 (cit. on pp. 134–136).

[Horc2007] P. Horcajada, S. Surblé, C. Serre, D.-Y. Hong, Y.-K. Seo, J.-S. Chang, J.-M. Grenèche, I. Margiolaki, and G. Férey. "Synthesis and catalytic properties of MIL-100(Fe), an iron(III) carboxylate with large pores". *Chem. Commun.*, no. 27. Jul. 2007. doi: 10.1039/B704325B (cit. on pp. 41, 42, 44).

[Hu2015] C. Hu, S. Sedghi, A. Silvestre-Albero, G. G. Andersson, A. Sharma, P. Pendleton, F. Rodríguez-Reinoso, K. Kaneko, and M. J. Biggs. "Raman spectroscopy study of the transformation of the carbonaceous skeleton of a polymer-based nanoporous carbon along the thermal annealing pathway". *Carbon*, vol. 85. Apr. 2015. doi: 10.1016/j.carbon.2014.12.098 (cit. on pp. 49, 71).

[Huan2016] T. N. Huan, P. Simon, G. Rousse, I. Génois, V. Artero, and M. Fontecave. "Porous dendritic copper: An electrocatalyst for highly selective CO2 reduction to formate in water/ionic liquid electrolyte". *Chem. Sci.*, vol. 8, no. 1. Dec. 2016. doi: 10.1039/C6SC03194C (cit. on pp. 83, 133).

[Huan2017] T. N. Huan, G. Rousse, S. Zanna, I. T. Lucas, X. Xu, N. Menguy, V. Mougel, and M. Fontecave. "A Dendritic Nanostructured Copper Oxide Electrocatalyst for the Oxygen Evolution Reaction". *Ange-*

wandte Chemie International Edition, vol. 56, no. 17. 2017. doi: 10.1002/anie.201700388 (cit. on pp. 83, 133).

[Huan2024a] H. Huang, K. Peramaiah, and K.-W. Huang. "Rethinking nitrate reduction: Redirecting electrochemical efforts from ammonia to nitrogen for realistic environmental impacts". *Energy Environ. Sci.*, vol. 17, no. 8. Apr. 2024. doi: 10.1039/D4EE00222A (cit. on pp. 2, 30, 133).

[Huan2024b] P.-W. Huang, H. Song, J. Yoo, D. A. Chipoco Haro, H. M. Lee, A. J. Medford, and M. C. Hatzell. "Impact of Local Microenvironments on the Selectivity of Electrocatalytic Nitrate Reduction in a BPM-MEA System". *Adv. Energy Mater.*. Feb. 2024. doi: 10.1002/aenm.202304202 (cit. on pp. 4, 79, 105).

[Huan2025] Y. Huang, Z. Zeng, T. Wang, and Z. Che. "Poisoning mechanism of ammonia on proton transport and ionomer structure in cathode catalyst layer of PEM fuel cells". *Chem. Eng. J.*, vol. 504. Jan. 2025. doi: 10.1016/j.cej.2024.158543 (cit. on pp. 93, 134, 135).

[Huo2020] X. Huo, J. Vanneste, T. Y. Cath, and T. J. Strathmann. "A hybrid catalytic hydrogenation/membrane distillation process for nitrogen resource recovery from nitrate-contaminated waste ion exchange brine". *Water Research*, vol. 175. May 2020. doi: 10.1016/j.watres.2020.115688 (cit. on pp. 134, 135).

[Ibl1961] N. Ibl. "Probleme des konvektiven Stofftransports bei der Elektrolyse". *Chemie Ingenieur Technik*, vol. 33, no. 2. 1961. doi: 10.1002/cite.330330202 (cit. on p. 4).

[IEA2021] IEA, "Ammonia Technology Roadmap: Towards more sustainable nitrogen fertiliser production", OECD Publishing, Paris, Tech. Rep., Oct. 2021. doi: 10.1787/f6daa4a0-en Accessed: Dec. 2, 2025 (cit. on pp. 1, 2, 24, 136).

[IEA2025] IEA, "Global Hydrogen Review 2025", Paris, Tech. Rep., Sep. 2025 (cit. on p. 32).

[Inag2010] M. Inagaki, H. Konno, and O. Tanaike. "Carbon materials for electrochemical capacitors". *Journal of Power Sources*, vol. 195, no. 24. Dec. 2010. doi: 10.1016/j.jpowsour.2010.06.036 (cit. on p. 46).

[IPCC2023] IPCC, “Climate Change 2023: Synthesis Report. Contribution of Working Groups I, II and III to the Sixth Assessment Report of the Intergovernmental Panel on Climate Change”, Genva, Switzerland, Tech. Rep., 2023, p. 184. Accessed: Dec. 15, 2025 (cit. on p. 1).

[IREN2022] IRENA and AEA, “Innovation Outlook Renewable Ammonia”, nternational Renewable Energy Agency, Abu Dhabi, Ammonia Energy Association, Brooklyn, Tech. Rep. Innovation Outlook: Renewable Ammonia, May 2022. Accessed: Nov. 7, 2025 (cit. on pp. 2, 24, 32, 135, 136).

[Jans1978] L. J. J. Janssen. “Mass transfer at gas evolving electrodes”. *Electrochimica Acta*, vol. 23, no. 2. Feb. 1978. doi: 10.1016/0013-4686(78)80101-7 (cit. on pp. 94, 133).

[Joos2025] M. Joos, X. Kang, R. Merkle, and J. Maier. “Water uptake of solids and its impact on ion transport”. *Nat. Mater.*, vol. 24, no. 6. Jun. 2025. doi: 10.1038/s41563-025-02143-8 (cit. on p. 134).

[Kara2023] M. Karamad, T. J. Goncalves, S. Jimenez-Villegas, I. D. Gates, and S. Siahrostami. “Why copper catalyzes electrochemical reduction of nitrate to ammonia”. *Faraday Discuss.*, vol. 243, no. 0. Jul. 2023. doi: 10.1039/D2FD00145D (cit. on p. 71).

[Kim2023] K. Kim, A. Zagalskaya, J. L. Ng, J. Hong, V. Alexandrov, T. A. Pham, and X. Su. “Coupling nitrate capture with ammonia production through bifunctional redox-electrodes”. *Nat Commun*, vol. 14, no. 1. Feb. 2023. doi: 10.1038/s41467-023-36318-1 (cit. on pp. 134, 136).

[Kord2000] V. Kordali, G. Kyriacou, and C. Lambrou. “Electrochemical synthesis of ammonia at atmospheric pressure and low temperature in a solid polymer electrolyte cell”. *Chemical Communications*, vol. 0, no. 17. 2000. doi: 10.1039/B004885M (cit. on p. 4).

[Krol1998] J. J. Krol, M. Jansink, M. Wessling, and H. Strathmann. “Behaviour of bipolar membranes at high current density: Water diffusion limitation”. *Separation and Purification Technology*, vol. 14, no. 1. Aug. 1998. doi: 10.1016/S1383-5866(98)00058-6 (cit. on p. 13).

[Lang1989a] S. Langlois and F. Coeuret. “Flow-through and flow-by porous electrodes of nickel foam. I. Material characterization”. *J Appl Electrochem*, vol. 19, no. 1. Jan. 1989. doi: 10.1007/BF01039388 (cit. on pp. 4, 22, 97, 134).

[Lang1989b] S. Langlois and F. Coeuret. “Flow-through and flow-by porous electrodes of nickel foam. II. Diffusion-convective mass transfer between the electrolyte and the foam”. *J Appl Electrochem*, vol. 19, no. 1. Jan. 1989. doi: 10.1007/BF01039389 (cit. on pp. 22, 97, 134).

[Lang1990a] S. Langlois and F. Coeuret. “Flow-through and flow-by porous electrodes of nickel foam Part III: Theoretical electrode potential distribution in the flow-by configuration”. *J Appl Electrochem*, vol. 20, no. 5. Sep. 1990. doi: 10.1007/BF01094300 (cit. on pp. 22, 97, 134).

[Lang1990b] S. Langlois and F. Coeuret. “Flow-through and flow-by porous electrodes of nickel foam Part IV: Experimental electrode potential distributions in the flow-through and in the flow-by configurations”. *J Appl Electrochem*, vol. 20, no. 5. Sep. 1990. doi: 10.1007/BF01094301 (cit. on pp. 22, 97, 134).

[Li2023] S. Li, D. Han, G. Jiang, Z. Han, H. Lu, J. Gao, X. Wang, Y. Wang, C. Geng, Z. Weng, and Q.-H. Yang. “Proton Exchange Membrane Electrode Assembly for Ammonia Electrosynthesis from Nitrate”. *ACS Appl. Energy Mater.*, vol. 6, no. 9. May 2023. doi: 10.1021/acsaem.3c00709 (cit. on p. 104).

[Lim2021] J. Lim, C. A. Fernández, S. W. Lee, and M. C. Hatzell. “Ammonia and Nitric Acid Demands for Fertilizer Use in 2050”. *ACS Energy Lett.*, vol. 6, no. 10. Oct. 2021. doi: 10.1021/acsenergylett.1c01614 (cit. on p. 135).

[Liu2015] C.-L. Liu, Z. Sun, G.-M. Lu, X.-F. Song, and J.-G. Yu. “Experimental and numerical investigation of two-phase flow patterns in magnesium electrolysis cell with non-uniform current density distribution”. *Can. J. Chem. Eng.*, vol. 93, no. 3. 2015. doi: 10.1002/cjce.22135 (cit. on p. 96).

[Liu2022] H. Liu, X. Lang, C. Zhu, J. Timoshenko, M. Rüscher, L. Bai, N. Guijarro, H. Yin, Y. Peng, J. Li, Z. Liu, W. Wang, B. R. Cuenya, and J. Luo. "Efficient Electrochemical Nitrate Reduction to Ammonia with Copper-Supported Rhodium Cluster and Single-Atom Catalysts". *Angew. Chem. Int. Ed.*, vol. 61, no. 23. 2022. doi: 10.1002/anie.202202556 (cit. on pp. 79, 80).

[Lore2025] F. Lorenzutti, R. R. Seemakurthi, E. F. Johnson, S. Morandi, P. Nikačević, N. López, and S. Haussener. "Microenvironment effects in electrochemical CO2 reduction from first-principles multiscale modelling". *Nat Catal*, vol. 8, no. 9. Sep. 2025. doi: 10.1038/s41929-025-01399-2 (cit. on pp. 4, 113).

[MacF2020] D. R. MacFarlane, P. V. Cherepanov, J. Choi, B. H. R. Suryanto, R. Y. Hodgetts, J. M. Bakker, F. M. Ferrero Vallana, and A. N. Simonov. "A Roadmap to the Ammonia Economy". *Joule*, vol. 4, no. 6. Jun. 2020. doi: 10.1016/j.joule.2020.04.004 (cit. on pp. 2, 3, 32, 79, 135).

[Mací2019] A. Macías-García, D. Torrejón-Martín, M. Á. Díaz-Díez, and J. P. Carrasco-Amador. "Study of the influence of particle size of activate carbon for the manufacture of electrodes for supercapacitors". *Journal of Energy Storage*, vol. 25. Oct. 2019. doi: 10.1016/j.est.2019.100829 (cit. on p. 47).

[Mari2024] Y. Maribel Allcca Castillo, Y. Adjez, V. Raul Jauja Ccana, G. A. Cerrón-Calle, S. Garcia-Segura, A. La Rosa-Toro Gómez, and C. M. Sánchez-Sánchez. "Benchmarking three-dimensional metal foam electrodes for the electrochemical reduction of nitrate". *J. Electroanal. Chem.*, vol. 968. Sep. 2024. doi: 10.1016/j.jelechem.2024.118499 (cit. on p. 136).

[Marn1998] G. Marnellos and M. Stoukides. "Ammonia Synthesis at Atmospheric Pressure". *Science*, vol. 282, no. 5386. Oct. 1998. doi: 10.1126/science.282.5386.98 (cit. on p. 4).

[Mart2017] J. Martínez, A. Ortiz, and I. Ortiz. "State-of-the-art and perspectives of the catalytic and electrocatalytic reduction of aqueous nitrates". *App. Cat. B Environ.*, vol. 207. Jun. 2017. doi: 10.1016/j.apcatb.2017.02.016 (cit. on pp. 134, 136).

[McEn2017] J. M. McEnaney, A. R. Singh, J. A. Schwalbe, J. Kibsgaard, J. C. Lin, M. Cargnello, T. F. Jaramillo, and J. K. Nørskov. “Ammonia synthesis from N2 and H2O using a lithium cycling electrification strategy at atmospheric pressure”. *Energy Environ. Sci.*, vol. 10, no. 7. Jul. 2017. doi: 10.1039/C7EE01126A (cit. on p. 4).

[McEn2020] J. M. McEnaney, S. J. Blair, A. C. Nielander, J. A. Schwalbe, D. M. Koshy, M. Cargnello, and T. F. Jaramillo. “Electrolyte Engineering for Efficient Electrochemical Nitrate Reduction to Ammonia on a Titanium Electrode”. *ACS Sustainable Chem. Eng.*, vol. 8, no. 7. Feb. 2020. doi: 10.1021/acssuschemeng.9b05983 (cit. on pp. 79, 134, 136).

[Mill2024] D. M. Miller, M. J. Liu, K. Abels, A. Kogler, K. S. Williams, and W. A. Tarpeh. “Engineering a molecular electrocatalytic system for energy-efficient ammonia production from wastewater nitrate”. *Energy Environ. Sci.*, vol. 17, no. 15. Jul. 2024. doi: 10.1039/D4EE01727G (cit. on p. 4).

[Mitt2007] V. O. Mittal, H. R. Kunz, and J. M. Fenton. “Membrane Degradation Mechanisms in PEMFCs”. *J. Electrochem. Soc.*, vol. 154, no. 7. May 2007. doi: 10.1149/1.2734869 (cit. on pp. 93, 134).

[Oar-2017] L. Oar-Arteta, T. Wezendonk, X. Sun, F. Kapteijn, and J. Gascon. “Metal organic frameworks as precursors for the manufacture of advanced catalytic materials”. *Mater. Chem. Front.*, vol. 1, no. 9. Aug. 2017. doi: 10.1039/C7QM00007C (cit. on pp. 33, 34).

[Paid2002] M. Paidar, K. Bouzek, and H. Bergmann. “Influence of cell construction on the electrochemical reduction of nitrate”. *Chem. Eng. J.*, vol. 85, no. 2-3. Jan. 2002. doi: 10.1016/S1385-8947(01)00158-9 (cit. on p. 78).

[Pärn2021] R. Pärnamäe, S. Mareev, V. Nikonenko, S. Melnikov, N. Sheldeshov, V. Zabolotskii, H. V. M. Hamelers, and M. Tedesco. “Bipolar membranes: A review on principles, latest developments, and applications”. *Journal of Membrane Science*, vol. 617. Jan. 2021. doi: 10.1016/j.memsci.2020.118538 (cit. on pp. 13, 68).

[Pärn2023] R. Pärnamäe, M. Tedesco, M.-C. Wu, C.-H. Hou, H. V. Hamelers, S. K. Patel, M. Elimelech, P. Biesheuvel, and S. Porada. “Origin of Limiting and Overlimiting Currents in Bipolar Membranes”. *Environ. Sci. Technol.*, vol. 57, no. 26. Jul. 2023. doi: 10.1021/acs.est.2c09410 (cit. on p. 13).

[Pati2021] S. B. Patil, T.-R. Liu, H.-L. Chou, Y.-B. Huang, C.-C. Chang, Y.-C. Chen, Y.-S. Lin, H. Li, Y.-C. Lee, Y. J. Chang, Y.-H. Lai, C.-Y. Wen, and D.-Y. Wang. “Electrocatalytic Reduction of NO3– to Ultrapure Ammonia on {200} Facet Dominant Cu Nanodendrites with High Conversion Faradaic Efficiency”. *J. Phys. Chem. Lett.*, vol. 12, no. 33. Aug. 2021. doi: 10.1021/acs.jpclett.1c02236 (cit. on pp. 58, 80).

[Pére2017] E. Pérez-Gallent, M. C. Figueiredo, I. Katsounaros, and M. T. M. Koper. “Electrocatalytic reduction of Nitrate on Copper single crystals in acidic and alkaline solutions.” *Electrochim. Acta*, vol. 227. Feb. 2017. doi: 10.1016/j.electacta.2016.12.147 (cit. on pp. 74, 89).

[Phu2024] T. K. C. Phu, P. L. Nguyen, T. V. B. Phung, and P.-A. Le. “A Perspective on Copper-Based Catalysts for Nitrate-to-Ammonia Electrochemical Reduction”. *Green Energy Environ. Tech.*, vol. 3, no. 1. Aug. 2024. (Cit. on p. 90).

[Pick1985] C. J. Pickett and J. Talarmin. “Electrosynthesis of ammonia”. *Nature*, vol. 317, no. 6038. Oct. 1985. doi: 10.1038/317652a0 (cit. on p. 4).

[Pirr2024] N. Pirrone, S. Garcia-Ballesteros, S. Hernández, and F. Bella. “Membrane/electrolyte interplay on ammonia motion inside a flow-cell for electrochemical nitrogen and nitrate reduction”. *Electrochimica Acta*, vol. 493. Jul. 2024. doi: 10.1016/j.electacta.2024.144415 (cit. on p. 67).

[Plet1979] D. Pletcher and Z. Poorabedi. “The reduction of nitrate at a copper cathode in aqueous acid”. *Electrochim. Acta*, vol. 24, no. 12. Dec. 1979. doi: 10.1016/0013-4686(79)87081-4 (cit. on pp. 4, 79, 89).

[Plet2009] D. Pletcher. *A First Course in Electrode Processes*. The Royal Society of Chemistry, Aug. 2009. isbn: 978-1-84755-893-0.doi: 10.1039/9781839169083 (cit. on pp. 9, 17).

[Pour1974] M. Pourbaix. *Atlas of Electrochemical Equilibria in Aqueous Solutions*. Houston, Texas: National Assoc. of Corrosion Engineers, 1974. isbn: 978-0-915567-98-0. (Cit. on p. 137).

[Raja2003] N. Rajalakshmi, T. Jayanth, and K. Dhathathreyan. "Effect of Carbon Dioxide and Ammonia on Polymer Electrolyte Membrane Fuel Cell Stack Performance". *Fuel Cells*, vol. 3, no. 4. 2003. doi: 10.1002/fuce.200330107 (cit. on p. 93).

[Ren2021] T. Ren, K. Ren, M. Wang, M. Liu, Z. Wang, H. Wang, X. Li, L. Wang, and Y. Xu. "Concave-convex surface oxide layers over copper nanowires boost electrochemical nitrate-to-ammonia conversion". *Chem. Eng. J.*, vol. 426. Dec. 2021. doi: 10.1016/j.cej.2021.130759 (cit. on p. 80).

[Rox2023] H. Rox, A. Bashkatov, X. Yang, S. Loos, G. Mutschke, G. Gerbeth, and K. Eckert. "Bubble size distribution and electrode coverage at porous nickel electrodes in a novel 3-electrode flow-through cell". *Int. J. Hydrog.*, vol. 48, no. 8. Jan. 2023. doi: 10.1016/j.ijhydene.2022.10.165 (cit. on pp. 96, 133, 134).

[Salv2021] D. A. Salvatore, C. M. Gabardo, A. Reyes, C. P. O'Brien, S. Holdcroft, P. Pintauro, B. Bahar, M. Hickner, C. Bae, D. Sinton, E. H. Sargent, and C. P. Berlinguette. "Designing anion exchange membranes for CO2 electrolysers". *Nat Energy*, vol. 6, no. 4. Apr. 2021. doi: 10.1038/s41560-020-00761-x (cit. on pp. 13, 134, 135).

[Sant2015] V. P. Santos, T. A. Wezendonk, J. J. D. Jaén, A. I. Dugulan, M. A. Nasalevich, H.-U. Islam, A. Chojecki, S. Sartipi, X. Sun, A. A. Hakeem, A. C. J. Koeken, M. Ruitenbeek, T. Davidian, G. R. Meima, G. Sankar, F. Kapteijn, M. Makkee, and J. Gascon. "Metal organic framework-mediated synthesis of highly active and stable Fischer-Tropsch catalysts". *Nat Commun*, vol. 6, no. 1. Mar. 2015. doi: 10.1038/ncomms7451 (cit. on p. 46).

[Schm2003] V. M. Schmidt. *Elektrochemische Verfahrenstechnik*. Weinheim: Wiley VCH, 2003. isbn: 3-527-29958-0. (Cit. on pp. 9, 12, 13, 18, 21–23, 96).

[Shen2025] S. Shen, S. Wang, B. Zhang, X. Zhao, C. Sun, S. Zhou, Z. Li, Y. Hou, L. Lei, and B. Yang. “Optimizing Nitrate Electroreduction toward Nearly 100% Ammonia Selectivity through Synergistic RuCu Catalysts and Integrated Coupled Anodic Reaction for High-Value Products”. *Chem. Bio. Eng.*, vol. 2, no. 1. Jan. 2025. doi: 10.1021/cbe.4c00124 (cit. on p. 136).

[Sign2024] V. Signorini, A. Askin, C. Oldani, M. Minelli, and M. Giacinti Baschetti. “Study on ammonia transport and separation in Aquivion® perfluoro sulfonated acid membranes”. *Journal of Membrane Science*, vol. 697. Mar. 2024. doi: 10.1016/j.memsci.2024.122564 (cit. on pp. 67, 134).

[Simo2025] A. N. Simonov, M. T. M. Koper, and D. R. MacFarlane. “Practical prospects of electroreduction of dilute NOx streams to ammonia”. *Nat Chem Eng*. Jul. 2025. doi: 10.1038/s44286-025-00240-8 (cit. on pp. 29, 134, 136).

[Skol2022] E. Skolotneva, K. Tsygurina, S. Mareev, E. Melnikova, N. Pismenskaya, and V. Nikonenko. “High Diffusion Permeability of Anion-Exchange Membranes for Ammonium Chloride: Experiment and Modeling”. *International Journal of Molecular Sciences*, vol. 23, no. 10. Jan. 2022. doi: 10.3390/ijms23105782 (cit. on p. 134).

[Skúl2011] E. Skúlason, T. Bligaard, S. Gudmundsdóttir, F. Studt, J. Rossmeisl, F. Abild-Pedersen, T. Vegge, H. Jónsson, and J. K. Nørskov. “A theoretical evaluation of possible transition metal electro-catalysts for N2 reduction”. *Phys. Chem. Chem. Phys.*, vol. 14, no. 3. Dec. 2011. doi: 10.1039/C1CP22271F (cit. on pp. 2, 32).

[Smit2020] C. Smith, A. K. Hill, and L. Torrente-Murciano. “Current and future role of Haber–Bosch ammonia in a carbon-free energy landscape”. *Energy Environ. Sci.*, vol. 13, no. 2. Feb. 2020. doi: 10.1039/C9EE02873K (cit. on pp. 1, 24–28, 135, 136).

[Stat] Statista, *Ammonia production worldwide 2024*, https://www.statista.com/statistics/1266378/global-ammonia-production. Accessed: Dec. 2, 2025 (cit. on pp. 1, 24).

[Sury2021] B. H. R. Suryanto, K. Matuszek, J. Choi, R. Y. Hodgetts, H.-L. Du, J. M. Bakker, C. S. M. Kang, P. V. Cherepanov, A. N. Simonov, and D. R. MacFarlane. “Nitrogen reduction to ammonia at high efficiency and rates based on a phosphonium proton shuttle”. *Science*, vol. 372, no. 6547. Jun. 2021. doi: 10.1126/science.abg2371 (cit. on p. 4).

[Syam2025] N. A.-P. Syamaladevi, A. Dutta, A. Rieder, X. Yu, H. Nedumkulam, J. Drnec, Z. Szakály, S. Vesztergom, R. K. Pittkowski, and P. Broekmann. “Transport Matters: The Critical Role of the Hydrogen Evolution Reaction (HER) in Accelerating Electrochemical Nitrate to Ammonia Conversion”. *Adv. Sci.*, vol. n/a, no. n/a. Sep. 2025. doi: 10.1002/advs.202506733 (cit. on pp. 92, 94).

[Tsun1994] A. Tsuneto, A. Kudo, and T. Sakata. “Lithium-mediated electrochemical reduction of high pressure N2 to NH3”. *Journal of Electroanalytical Chemistry*, vol. 367, no. 1. Mar. 1994. doi: 10.1016/0022-0728(93)03025-K (cit. on p. 4).

[Urib2002] F. A. Uribe, S. Gottesfeld, and T. A. Zawodzinski. “Effect of Ammonia as Potential Fuel Impurity on Proton Exchange Membrane Fuel Cell Performance”. *J. Electrochem. Soc.*, vol. 149, no. 3. Jan. 2002. doi: 10.1149/1.1447221 (cit. on pp. 93, 132, 134).

[Velá2011] A. Velázquez-Palenzuela, L. Zhang, L. Wang, P. L. Cabot, E. Brillas, K. Tsay, and J. Zhang. “Carbon-Supported Fe–N_x Catalysts Synthesized by Pyrolysis of the Fe(II)–2,3,5,6-Tetra(2-pyridyl)pyrazine Complex: Structure, Electrochemical Properties, and Oxygen Reduction Reaction Activity”. *J. Phys. Chem. C*, vol. 115, no. 26. Jul. 2011. doi: 10.1021/jp2020897 (cit. on p. 34).

[Venn2019] J.-B. Vennekötter, T. Scheuermann, R. Sengpiel, and M. Wessling. “The electrolyte matters: Stable systems for high rate electrochemical CO2 reduction”. *Journal of CO2 Utilization*, vol. 32. Jul. 2019. doi: 10.1016/j.jcou.2019.04.007 (cit. on pp. 13, 133, 135).

[vLang2021] P. H. van Langevelde, I. Katsounaros, and M. T. M. Koper. “Electrocatalytic Nitrate Reduction for Sustainable Ammonia Production”. *Joule*, vol. 5, no. 2. Feb. 2021. doi: 10.1016/j.joule.2020.12.025 (cit. on pp. 28, 29, 58, 80, 135).

[Wang2020] Y. Wang, W. Zhou, R. Jia, Y. Yu, and B. Zhang. “Unveiling the Activity Origin of a Copper-based Electrocatalyst for Selective Nitrate Reduction to Ammonia”. *Angew. Chem. Int. Ed.*, vol. 59, no. 13. 2020. doi: 10.1002/anie.201915992 (cit. on pp. 58, 80).

[Wang2021] M. Wang, M. A. Khan, I. Mohsin, J. Wicks, A. H. Ip, K. Z. Sumon, C.-T. Dinh, E. H. Sargent, I. D. Gates, and M. G. Kibria. “Can sustainable ammonia synthesis pathways compete with fossil-fuel based Haber–Bosch processes?”, *Energy Environ. Sci.*, vol. 14, no. 5. May 2021. doi: 10.1039/D0EE03808C (cit. on pp. 26, 27, 134).

[Wang2023a] Y. Wang, A. Dutta, A. Iarchuk, C. Sun, S. Vesztergom, and P. Broekmann. “Boosting Nitrate to Ammonia Electroconversion through Hydrogen Gas Evolution over Cu-foam@mesh Catalysts”. *Am. Chem. Soc. Catal.*, vol. 13, no. 12. Jun. 2023. doi: 10.1021/acscatal.3c00716 (cit. on pp. 92, 94, 133).

[Wang2023b] Z. Wang, S. Liu, X. Zhao, M. Wang, L. Zhang, T. Qian, J. Xiong, C. Yang, and C. Yan. “Interfacial Defect Engineering Triggered by Single Atom Doping for Highly Efficient Electrocatalytic Nitrate Reduction to Ammonia”. *Am. Chem. Soc. Mater. Lett.*, vol. 5, no. 4. Apr. 2023. doi: 10.1021/acsmaterialslett.3c00007 (cit. on pp. 58, 80).

[Wang2024] A. Wang, J. Ye, Y. Yang, G. He, and H. Chen. “Recent advances in nickel-based catalysts for electrochemical nitrate reduction to ammonia”. *Journal of Industrial and Engineering Chemistry*, vol. 132. Apr. 2024. doi: 10.1016/j.jiec.2023.11.039 (cit. on p. 70).

[Wei2021] X. Wei, M. Pu, Y. Jin, and M. Wessling. “Efficient Electrocatalytic N2 Reduction on Three-Phase Interface Coupled in a Three-Compartment Flow Reactor for the Ambient NH3 Synthesis”. *ACS Appl. Mater. Interfaces*, vol. 13, no. 18. May 2021. doi: 10.1021/acsami.1c03698 (cit. on p. 33).

[Weze2016] T. A. Wezendonk, V. P. Santos, M. A. Nasalevich, Q. S. Warringa, A. I. Dugulan, A. Chojecki, A. C. J. Koeken, M. Ruitenbeek, G. Meima, H.-U. Islam, G. Sankar, M. Makkee, F. Kapteijn, and J. Gascon. “Elucidating the Nature of Fe Species during Pyrolysis of the Fe-BTC MOF into Highly Active and Stable Fischer–Tropsch

Catalysts". *ACS Catal.*, vol. 6, no. 5. May 2016. doi: 10.1021/acscatal.6b00426 (cit. on pp. 34, 46).

[Wild2024] L. M. Wilder, K. Wyatt, C. A. Skangos, W. E. Klein, M. R. Parimuha, J. L. Katsirubas, J. L. Young, and E. M. Miller. "Membranes Matter: Preventing Ammonia Crossover during Electrochemical Ammonia Synthesis". *ACS Appl. Energy Mater.*, vol. 7, no. 2. Jan. 2024. doi: 10.1021/acsaem.3c02461 (cit. on pp. 67, 134).

[Wu2020] W. Wu, Z. Zhang, Z. Lei, X. Wang, Y. Tan, N. Cheng, and X. Sun. "Encapsulating Pt Nanoparticles inside a Derived Two-Dimensional Metal–Organic Frameworks for the Enhancement of Catalytic Activity". *ACS Appl. Mater. Interfaces*, vol. 12, no. 9. Mar. 2020. doi: 10.1021/acsami.9b20781 (cit. on p. 48).

[Xion2024] Y. Xiong, Y. Wang, J. Zhou, F. Liu, F. Hao, and Z. Fan. "Electrochemical Nitrate Reduction: Ammonia Synthesis and the Beyond". *Adv. Mater.*, vol. 36, no. 17. 2024. doi: 10.1002/adma.202304021 (cit. on pp. 58, 80).

[Xu2023] Z. Xu, L. Wan, Y. Liao, M. Pang, Q. Xu, P. Wang, and B. Wang. "Continuous ammonia electrosynthesis using physically interlocked bipolar membrane at 1000 mA cm-2". *Nat. Commun.*, vol. 14, no. 1. Mar. 2023. doi: 10.1038/s41467-023-37273-7 (cit. on pp. 4, 13, 58, 79, 80, 90).

[Yang2016] Z. K. Yang, Z.-W. Zhao, K. Liang, X. Zhou, C.-C. Shen, Y.-N. Liu, X. Wang, and A.-W. Xu. "Synthesis of nanoporous structured iron carbide/Fe–N–carbon composites for efficient oxygen reduction reaction in Zn–air batteries". *J. Mater. Chem. A*, vol. 4, no. 48. Dec. 2016. doi: 10.1039/C6TA08050B (cit. on pp. 49, 50).

[Yang2023] M. Yang, B. Li, S. Li, Q. Dong, Z. Huang, S. Zheng, Y. Fang, G. Zhou, X. Chen, X. Zhu, T. Li, M. Chi, G. Wang, L. Hu, and Z. J. Ren. "Highly Selective Electrochemical Nitrate to Ammonia Conversion by Dispersed Ru in a Multielement Alloy Catalyst". *Nano Lett.*, vol. 23, no. 16. Aug. 2023. doi: 10.1021/acs.nanolett.3c01978 (cit. on p. 90).

[Yang2024] K. Yang, S.-H. Han, C. Cheng, C. Guo, T. Li, and Y. Yu. “Unveiling the Reaction Mechanism of Nitrate Reduction to Ammonia Over Cobalt-Based Electrocatalysts”. *J. Am. Chem. Soc.*, vol. 146, no. 19. May 2024. doi: 10.1021/jacs.3c13517 (cit. on p. 71).

[Yi2020] X. Yi, X. He, F. Yin, T. Yang, B. Chen, and G. Li. “NH2–MIL-88B–Fe for electrocatalytic N2 fixation to NH3 with high Faradaic efficiency under ambient conditions in neutral electrolyte”. *J Mater Sci*, vol. 55, no. 26. Sep. 2020. doi: 10.1007/s10853-020-04777-2 (cit. on p. 33).

[Yuan2024] T. Yuan, T. Burdyny, M. Li, S. Subramanian, J. Kok, M. Li, A. Urakawa, and O. Voznyy. “Sequential electrocatalytic reactions along a membrane electrode assembly drive efficient nitrate-to-ammonia conversion”. *Cell Rep. Phys. Sci.*. May 2024. doi: 10.1016/j.xcrp.2024.101977 (cit. on pp. 4, 58, 79–81, 90, 104).

[Zhan2023] R. Zhang, C. Li, H. Cui, Y. Wang, S. Zhang, P. Li, Y. Hou, Y. Guo, G. Liang, Z. Huang, C. Peng, and C. Zhi. “Electrochemical nitrate reduction in acid enables high-efficiency ammonia synthesis and high-voltage pollutes-based fuel cells”. *Nat. Commun.*, vol. 14, no. 1. Dec. 2023. doi: 10.1038/s41467-023-43897-6 (cit. on pp. 81, 89).

[Zhan2024a] W. Zhang, Y. Yao, Z. Chen, S. Zhao, F. Guo, and L. Zhang. “Fluorine Modification Promoted Water Dissociation into Atomic Hydrogen on a Copper Electrode for Efficient Neutral Nitrate Reduction and Ammonia Recovery”. *Environ. Sci. Technol.*, vol. 58, no. 16. Apr. 2024. doi: 10.1021/acs.est.4c00151 (cit. on p. 79).

[Zhan2024b] X.-L. Zhang, P.-C. Yu, S.-P. Sun, L. Shi, P.-P. Yang, Z.-Z. Wu, L.-P. Chi, Y.-R. Zheng, and M.-R. Gao. “In situ ammonium formation mediates efficient hydrogen production from natural seawater splitting”. *Nat. Commun.*, vol. 15, no. 1. Nov. 2024. doi: 10.1038/s41467-024-53724-1 (cit. on p. 92).

List of Abbreviations

AEM anion exchange membrane

BET Brunauer-Emmett-Teller

BPM bipolar membrane

CC constant current

CCM catalyst-coated membrane

CEM cation exchange membrane

DFT density functional theory

ED electrodialysis

EDL electric double layer

eNO_3RR electrochemical nitrate reduction reaction

eNRR electrochemical nitrogen reduction reaction

FE faradaic efficiency

GC gas chromatography

GDE gas diffusion electrode

GDL gas diffusion layer

GEIS galvanostatic electrochemical impedance spectroscopy

HB Haber-Bosch

HER hydrogen evolution reaction

IC ion chromatography

LSV linear sweep voltammetry

MEA membrane electrode assembly

MOF Metal-Organic-Framework

PE pulsed electrolysis

RDE rotating disk electrode

RHE reversible hydrogen electrode

RO reverse osmosis

SEM scanning electron microscopy

SMR steam methane reforming

TEM transmission electron microscopy

XRD X-ray diffraction